

**THE EFFECTS OF LIGHT-WEIGHT INTERFACE
MATERIAL ON THE STRESS WAVE
PROPAGATION IN THE MULTILAYERED
COMPOSITE ARMOR SYSTEM**

**A Thesis Submitted to
the Graduate School of Engineering and Sciences of
İzmir Institute of Technology
in Partial Fulfillment of the Requirements for the Degree of**

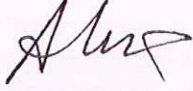
MASTER OF SCIENCE

in Mechanical Engineering

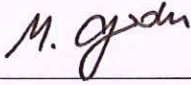
**by
Gözde TUNUSOĞLU**

**July 2011
İZMİR**

We approve the thesis of **Gözde TUNUSOĞLU**



Assoc. Prof. Dr. Alper TAŞDEMİRCİ
Supervisor



Prof. Dr. Mustafa GÜDEN
Committee Member



Prof. Dr. Ramazan KARAKUZU
Committee Member

4 July 2011

Prof. Dr. Metin TANOĞLU
Head of the Department of
Mechanical Engineering

Prof. Dr. Durmuş Ali DEMİR
Dean of the Graduate School of
Engineering and Sciences

ACKNOWLEDGEMENTS

I would like to express my sincere gratitude to my supervisor Assoc. Prof. Dr. Alper TAŞDEMİRÇİ for his valuable advises, great patience and guidance through the thesis.

I would like to thank Prof. Dr. Mustafa GÜDEN for both his endless support and material support.

Thanks to all of my lab-mates, and room-mates, Ali KARA, Kutlay ODACI and A. Kıvanç TURAN who especially played great role in my experimental, numerical analysis and writing studies for their precious efforts.

Thanks to TÜBİTAK for financial support grant #106M353 project.

Thanks to Mechanical and Chemical Industry Corporation, Ankara for technical support.

Thanks to Center of Composite Materials, Newark, D.E., U.S.A for material support.

I am also grateful to my friends for their great patience, support and kindness.

I would like to thank my family, my mother Nurdan TUNUSOĞLU, my father Ali TUNUSOĞLU and my sister Özge TUNUSOĞLU who have always encouraged and supported me, as they did so during my graduate studies.

Lastly, I would like to thank Mert TUNÇER and Hanife TUNÇER for their great patience, encouragement and support for all this thesis period.

ABSTRACT

THE EFFECTS OF LIGHT-WEIGHT INTERFACE MATERIAL ON THE STRESS WAVE PROPAGATION IN THE MULTILAYERED COMPOSITE ARMOR SYSTEM

The main purpose of the current study is to investigate the effect of interlayer material on the ballistic performance of composite armor and stress wave propagation both experimentally and numerically. Three different interlayer materials, EPDM rubber, Teflon and Aluminum metallic foam, were tried. Relatively large pieces of the ceramic around the impact axis in the rubber interlayer configuration were observed while the ceramic layer was efficiently fragmented in Aluminum foam and Teflon interlayer configurations. Accordingly, more significant amount of delamination in composite layer of without interlayer, larger and deeper delamination in EPDM rubber configurations was observed while fewer amounts were observed on Teflon and Aluminum foam configurations. Also, all interlayers caused reduction in the magnitude of the stress transmitted to the composite backing plate, particularly Aluminum foam. However, EPDM rubber did not cause delay in the initial stress build-up in the composite layer, whereas Teflon ($\sim 15 \mu\text{s}$) and Aluminum foam ($\sim 25 \mu\text{s}$) caused a significant delay. Also, as ceramic was efficiently fragmented in Teflon and Aluminum metallic foam interlayer configurations, greater amount of projectile kinetic energy was absorbed in this layer, as a consequence, the remaining energy which was transmitted to composite backing plate was decreased. At this point, the effectiveness of Aluminum foam and Teflon were validated with conducting ballistic tests and corresponding numerical simulations and impact chamber tests. After this validation, the ballistic performance of aforementioned materials was compared at equal areal densities. Finally, Aluminum foam was found to be more effective interlayers in reducing the stress values transmitted to the composite backing plate and reduction of the damage imparted to this layer.

ÖZET

HAFİF ARA YÜZEY MALZEMELERİNİN ÇOK KATMANLI KOMPOZİT ZIRH SİSTEMİNDE GERİLME DALGASI YAYINIMINA ETKİLERİ

Bu çalışmanın ana amacı, ara yüzey malzemesinin kompozit zırhın balistik performansına etkisini ve gerilme dalgası ilerleyişini nümerik ve deneysel olarak incelemektir. Üç farklı ara yüzey malzemesi, EPDM lastik, Teflon ve alüminyum metalik köpük denenmiştir. Alüminyum metalik köpük ve Teflon ara yüzey malzemesi içeren konfigürasyonlarda seramik katman istenildiği gibi etkin şekilde kırılmaktayken, diğer konfigürasyonlarda kırılma eksenini etrafında nispeten daha büyük seramik kırıkları gözlenmektedir. Buna bağlı olarak, ara yüzeyli halin kompozit katmanı üzerinde ciddi miktarda delaminasyon gözlenirken, EPDM lastik içeren konfigürasyonun kompozit katmanında Teflon'dakine göre daha geniş ve derin, Teflon ve alüminyum köpük ara yüzeyli konfigürasyonlarda ise daha az miktarda hasar gözlenmektedir. Ayrıca, tüm ara yüzey malzemeleri, özellikle alüminyum köpük, kompozit katmana iletilen gerilme değeri miktarında önemli oranda azalmaya neden olmaktadır. Ancak, Teflon ve alüminyum köpük ara yüzeyleri kompozit katmanı gerilme dalgası iletimi sırasında önemli oranda gecikmeye neden olurken (sırasıyla ~15 ve ~25 μ s), EPDM lastik ara yüzeyi kompozit plakanın ilk gerilme oluşumunda kayda değer bir gecikmeye neden olmamıştır. Buna ek olarak, Teflon ve alüminyum metalik köpük ara yüzey malzemesi içeren konfigürasyonlarda seramik etkin bir şekilde kırıldığından, mermi kinetik enerjisinin büyük bölümü bu katmanda sökülmenmiş, sonuç olarak, kompozit katmana iletilen enerji azalmıştır. Bu noktada alüminyum metalik köpük ve Teflon ara yüzeylerinin etkinlikleri zırh delici mermi kullanılarak yapılan balistik testler ve bunların nümerik simülasyonları ve çelik bilye kullanılarak yapılan çarpma haznesi testleriyle doğrulanmıştır. Söz konusu malzemeler, balistik performanslarının kanıtlanmasının ardından, eş alansal yoğunluklarda incelenmişlerdir. Sonuç olarak alüminyum metalik köpüğün kompozit katmana iletilen gerilme değerinin azaltılması, iletim zamanının gecikmesi ve bu katmandaki hasar miktarının azaltılmasında en etkin ara yüzey malzemesi olduğu saptanmıştır.

TABLE OF CONTENTS

LIST OF FIGURES.....	viii
LIST OF TABLES.....	xiii
CHAPTER 1. INTRODUCTION.....	1
CHAPTER 2. TYPES OF ARMORS.....	7
2.1. Monolithic Armors.....	7
2.2. Ceramic-Metal and Ceramic-Composite Armors.....	9
2.3. Basic Concepts of Multilayered Armors.....	12
2.3.1. Impact Characteristics of Alumina	12
2.3.2. Acoustic Impedance Mismatch.....	14
2.4. Literature Survey.....	17
2.5. Motivation.....	19
CHAPTER 3. EXPERIMENTAL SETUP.....	20
3.1. Test Methods.....	20
3.2. Tests for Mechanical Characterization.....	20
3.2.1. Quasi-Static Tests.....	21
3.2.2. High Strain Rate Testing and Split Hopkinson Pressure Bar.....	22
3.3. Penetration and Perforation Tests	28
3.3.1. Ballistic Tests.....	28
3.3.2. Compressed Air Gun Tests.....	30
CHAPTER 4. EXPERIMENTAL AND NUMERICAL STUDIES OF STRESS WAVE PROPAGATION IN ARMOR SYSTEM CONSTITUENTS	35
4.1. Armor Constituents	36
4.1.1. Ceramic Front Layer	37
4.1.2. Interlayer Materials	40

4.1.2.1. EPDM Rubber.....	41
4.1.2.2. Teflon.....	43
4.1.2.3. Aluminum Metallic Foam.....	44
4.1.3. Composite Backing Plate	46
4.1.3.1. Fabrication of E-Glass/polyester Composite.....	47
4.1.3.2. Mechanical Characterization of E-Glass/polyester Composite.....	48
4.1.3.3. Verification of Material Model Parameters of E-Glass/polyester Composite	57
4.1.4. Polyester Cover Layer	62
4.1.5. Projectile	64
CHAPTER 5. INVESTIGATION ON THE BALLISTIC PERFORMANCE OF ARMOR CONFIGURATIONS	66
5.1. Specimen Preparation and Experimental Study	67
5.2. Finite Element Model Description	67
5.3. Experimental and Numerical Results	71
5.4. The Effect of Interlayer Thickness on Ballistic Performance	93
CHAPTER 6. COMPRESSED AIR GUN (IMPACT CHAMBER) EXPERIMENTS	100
6.1. Sample Preparation and Compressed Air Gun Tests	100
6.2. Damage Analysis	104
CHAPTER 7. CONCLUSION.....	110
REFERENCES.....	112

LIST OF FIGURES

<u>Figure</u>	<u>...Page</u>
Figure 1.1. Shield and weapon of Sumerians.	2
Figure 1.2. Primitive tank.	3
Figure 1.3. Kevlar body armor.....	5
Figure 1.4. Kevlar with shear thickening fluid.	6
Figure 2.1. Impact response of armor ceramic under different velocities.	13
Figure 2.2. Four stages of projectile penetration into ceramic armor.	14
Figure 2.3. Wave reflection.	14
Figure 3.1. Quasi-static testing apparatus.	21
Figure 3.2. Schematic of SHPB.	23
Figure 3.3. Schematic of specimen and waves.	23
Figure 3.4. Typical SHPB signal.	24
Figure 3.5. Typical stress history.	24
Figure 3.6. SHPB set-up.	25
Figure 3.7. Chronograph and high speed camera.	26
Figure 3.8. High speed camera images of 0/90 E-Glass/polyester composite tested in the through-thickness direction.	26
Figure 3.9. High speed camera images of 0/90 E-Glass/polyester composite tested in the in-plane direction.	27
Figure 3.10. Ballistic test set-up.	28
Figure 3.11. Schematic view of 7.62 x 51 mm NATO A.P. (M61) projectile.	30
Figure 3.12. Rifle constituents of compressed air gun set-up (a) Sabot (with steel ball projectile) (b) Scraper.	32
Figure 3.13. Compressed air gun set-up.	32
Figure 3.14. Armor holder.	33
Figure 3.15. Sequence of captured images during compressed air gun experiment.	33
Figure 3.16. Chronograph used in compressed air gun test set-up.	34
Figure 4.1. Armor constituents: (a) Alumina ceramic, (b) EPDM rubber and Teflon, (c) Aluminum foam and (d) E-Glass and S2-Glass Composite.	36
Figure 4.2 Description of JH-2 model in aspects of pressure distribution.	39
Figure 4.3. Data fit for Ogden material model, N=3.	43

Figure 4.4. Typical yield stress vs. volumetric strain data for crushable foam.	44
Figure 4.5. The processing stages of the foaming from powder compact process used.	45
Figure 4.6. Honeycomb material model description.....	46
Figure 4.7. VARTM station.....	47
Figure 4.8. Core-drill.....	48
Figure 4.9. E-Glass composite specimen.....	48
Figure 4.10. Stress-strain curves of 0/90 E-Glass/polyester composites at 0.001 s ⁻¹ : (a) in-plane and (b) through-thickness directions.....	49
Figure 4.11. Stress-strain curves of 0/90 E-Glass/polyester composites at an average strain rate of 850 s ⁻¹ : (a) in-plane and (b) through-thickness directions.....	50
Figure 4.12. Stress-strain curves of 0/90 E-Glass/polyester composites at various strain rates: (a) in-plane and (b) through-thickness directions.....	50
Figure 4.13. Photographs of samples tested in the in-plane direction: (a) quasi-static and (b) high strain rate.	51
Figure 4.14. Photographs of samples tested in the through-thickness direction: (a) quasi-static and (b) high strain rate.	51
Figure 4.15. SEM image of specimen tested in the through-thickness direction.	52
Figure 4.16. Elastic modulus vs. strain rate.	55
Figure 4.17. Stress vs. strain rate in: (a) in-plane and (b) through-thickness directions.....	55
Figure 4.18. Stress vs. strain curves of 0/90 E-Glass composite at 850 s ⁻¹ strain rate in the in-plane direction: (a) experimental, and (b) numerical (single element model).....	56
Figure 4.19. Stress vs. strain curves of 0/90 E-Glass composite at 850 s ⁻¹ strain rate in the through-thickness direction: (a) experimental, and (b) numerical (single element model).....	56
Figure 4.20. SHPB numerical model.	60
Figure 4.21. Bar responses of SHPB experiments in the in-plane direction: (a) experimental, and (b) numerical	61
Figure 4.22. Bar response of SHPB experiments in the through-thickness direction (a) experimental and (b) numerical.....	62
Figure 4.23. Delamination damage: (a) in-plane and (b) through-thickness.	62

Figure 4.24. Elastic-plastic behavior with isotropic and kinematic hardening.....	64
Figure 5.1. Mounted ceramic/composite armor target: (a) top and (b) side view.	67
Figure 5.2. Ballistic test numerical model (a) top (b) cross-sectional views.....	68
Figure 5.3. Different size meshes of ceramic layer: (a) coarse, (b) medium and (c) fine.	69
Figure 5.4. Force vs. time data of ceramic layers for different mesh sizes.	70
Figure 5.5. Ballistic test specimens: (a) without, (b) with EPDM rubber, (c) Teflon and (d) Aluminum foam interlayers.....	71
Figure 5.6. Damage occurred in ceramic layer.	72
Figure 5.7. Fracture conoid: (a) experimental and (b) numerical.	74
Figure 5.8. Damage occurred in ceramic layers of different configurations: (a) without interlayer, (b) EPDM rubber, (c) Teflon and (d) Aluminum foam.	75
Figure 5.9. Delamination damage in the composite layers of different configurations: (a) without interlayer, (b) EPDM rubber, (c) Teflon and (d) Aluminum foam.	76
Figure 5.10. Material directions.....	77
Figure 5.11. Fiber damage in the composite layers of different configurations in the in-plane and through-thickness directions consecutively: ((a)-(b)) without interlayer ((c)-(d)) EPDM rubber, ((e)-(f)) Teflon and ((g)-(h)) Aluminum foam.	78
Figure 5.12. Projectile (a) residual velocity and (b) mass vs. time.....	79
Figure 5.13. The eroded energy history of projectile.	79
Figure 5.14. Internal and kinetic energies of eroded and non-eroded elements.	81
Figure 5.15. Energy balance in aspects of (a) conservation of energy and (b) hourglass energy ratio.	81
Figure 5.16. Energy dissipation in armor constituents.	82
Figure 5.17. The energy histories of the ceramic layer: (a) internal, (b) kinetic and (c) eroded internal.	83
Figure 5.18. The energy histories of the composite plate: (a) kinetic and (b) total internal.....	84
Figure 5.19. The Z-force history at the interlayer-composite interface.....	85
Figure 5.20. Element notation of stress/time/distance maps.	86

Figure 5.21. Stress/time/distance maps along line B on composite layer of different interlayer configurations: (a) without, (b) with EPDM rubber, (c) Teflon and (d) Aluminum foam.	87
Figure 5.22. Stress/time/distance maps along line C on composite layer of different interlayer configurations: (a) without, (b) with EPDM rubber, (c) Teflon and (d) Aluminum foam.	89
Figure 5.23. Stress vs. time data of different elements for all configurations: (a) B12, (b) C12, (c) B24, (d) C24.....	91
Figure 5.24. Stress rise time delay in Teflon and Aluminum foam.....	92
Figure 5.25. Complete erosion of Teflon.....	92
Figure 5.26. Numerical models: ((a)-(b)) 2.3 and 4.6 mm Teflon, ((c)-(d)) 4 and 8 mm Aluminum foam.....	93
Figure 5.27. Energy histories of the ceramic layers: (a) internal, (b) total internal and (c) kinetic.	94
Figure 5.28. Projectile (a) residual velocity and (b) mass vs. time data of different thickness configurations.	95
Figure 5.29. Variations of : (a) internal, (b) total internal and (c) kinetic energies of composite layer.....	96
Figure 5.30. Top views of (a) 2.3 and (b) 4.6 mm Teflon (c) 4 and (d) 8 mm Aluminum foam 250 μ s after impact.....	97
Figure 5.31. Damage contours in the ceramic layers of different interlayer configurations: ((a)-(b)) 2.3 and 4.6 mm Teflon and ((c)-(d)) 4 and 8 mm Aluminum foam.	98
Figure 5.32. Delamination damage in composite layers of different interlayer configurations : ((a)-(b)) 2.3 and 4.6 mm Teflon and ((c)-(d)) 4 and 8 mm Aluminum foam.	99
Figure 6.1. Targets of different configurations tested at compressed air gun test set-up: (a) without interlayer, (b) with EPDM rubber, (c) Teflon and (d) Aluminum foam interlayers.	101
Figure 6.2. Real time images of compressed air gun tests (a)WR, (b)WT and (c) WF.	102
Figure 6.3. Damage contours in the ceramic layer after compressed air gun tests: (a)WO, (b)WR, (c)WT and (d) WF.....	105

Figure 6.4. Delamination damage contours in the composite layer after compressed air gun tests: (a) WO (b) WR (c) WT and (d) WF configurations.	106
Figure 6.5. SEM images of composite layers: (a) WO (b) WR (c) WT and (d) WF configurations.	107
Figure 6.6. Different damage modes observed in Teflon configuration.	108
Figure 6.7. Fiber crush and fiber/matrix cracks observed in rubber configuration.	109
Figure 7.1. Preliminary study of a compressed air gun numerical model.	111

LIST OF TABLES

<u>Table</u>	Page
Table 2.1. Selected mechanical properties of monolithic armors.....	8
Table 2.2. Mechanical properties of composite armors.....	9
Table 2.3. History of modern armor.	11
Table 2.4. Acoustic impedance values of armor constituents used in current study.	16
Table 3.1. Dynamic aspects of mechanical testing.	22
Table 3.2. Mechanical properties of bar material.	25
Table 3.3. Technical properties of a 7.62 mm NATO A.P. projectile.....	30
Table 3.4. Armor types and protection levels.....	31
Table 4.1. Mechanical properties of alumina ceramic.....	37
Table 4.2. JH-2 material model parameters of alumina ceramic.....	41
Table 4.3. Mechanical properties of EPDM rubber and Teflon.	44
Table 4.4. Mechanical properties of Aluminum foam.....	46
Table 4.5. Material model constants of 0/90 E-Glass/polyester composite.....	58
Table 4.6. Material model constants of 0/90 S2-Glass/epoxy composite.....	59
Table 4.7. Mechanical properties of polyester.....	63
Table 4.8. Material model parameters of projectile.....	65
Table 5.1. Details of the mesh used through the study.	70
Table 6.1. Number of radial and circular cracks.....	104

CHAPTER 1

INTRODUCTION

Mankind has always tendency to war. Since the birth of civilization human race has been in war and people have fought for different reasons i.e. land, food, honor. As people fight, there is a certain necessity to protect them, so armors have been needed for this purpose. Over the years technology driven wars and operations necessitate the innovations for protection.

Armor systems advance with the progress that has been made in weapon area since ancient times. When weapons were primitive (raw sticks and rocks), shields made up of animal furs or barks were strong enough to protect. As more advanced weapons like sharpened metal tip sticks were invented, more complex armors were created by weaving bones or rocks into clothing. First known armor in history dates back to 4000-5000 years ago. In explorations, people with sharpening sticks and shields were seen from the drawings discovered in Ancient Egypt (Figure 1.1).

Sumerians were almost the first to make use of body armor on all of their infantry. Illustrations indicate that Sumerian soldiers wore goat wool tunic and possibly leather and bronze helmet. Furthermore, they brought a new approach to armor design by using a metal stud interwoven leather cloaks and electrum helmets. Electrum is a weak gold and silver alloy so this helmet was used for ceremonial purposes.

The Assyrians' archers wore a conical helmet made of bronze in the early years and later made from iron. The archers also wore a short sleeved, ankle length body armor, known as lamellar armor. Lamellar armor is a kind of scale armor. The scales in lamellar armor are attached to all of the adjacent scales making it stronger.

The Mycenaean brought new developments to the armor history such as a leather helmet made of 30-40 alternating boar tusks. A complete suit of bronze plate armor was also discovered. This armor of Mycenae is the first known bronze cuirass, body armor. One of the shields that Mycenaean used consists of seven layers of wood, bronze and leather.

The Greeks developed armor to some extent. Most Greeks wore breastplates made of bronze. The basic Greek soldier wore a bronze helmet that covered most of his head, nose and cheeks.



Figure 1.1. Shield and weapon of Sumerians.
(Source: history of armor, 2011).

Typical to most cultural patterns, the first armors to appear in China were mostly for the noble classes. The earliest armors were made out of turtle shells lashed together to make a coat of shells. Later on, they used leather and bronze body armors, and bronze helmets. Until the invention of lacquered leather armors, they used buffalo skin (history of armor, 2011).

After the Roman Empire crumbled, Europe was divided into small kingdoms and the importance given on military was enormously increased. Small kingdoms tried to develop better weapons and more protective armors for possible attacks. Medieval knight armor started out with chain-mail, created by interlocking tens of thousands of small metal rings. These rings were individually riveted together in order to increase the strength of armor. Knight armor evolved between the 13th and 15th centuries and full-grown version consisted of a complex series of plates and other garments held together by leather straps and buckles. In the 15th century the knights were fully covered with metal plate armors to protect from more dangerous metal weapons: swords. In the 16th century, the weight of a full plate armor reach to ~25 kg. This heavy and strong body

armors with shields had stayed as a dominant design for a long time, up to the invention of guns, and armor fighting vehicles, tanks (history of armor, 2011; wikipedia.org, 2011).

In the early 19th century, the technology race was accelerated by the industrial revolution. Tank were started to be invented and machine guns were developed, accordingly, idea of controlling the global system arises (Figure 1.2). This desire of developed countries brings the wars. Hence, progress in military technology was unavoidably increased. As more destructive weapons were developed so were protective armors (wikipedia, 2011).

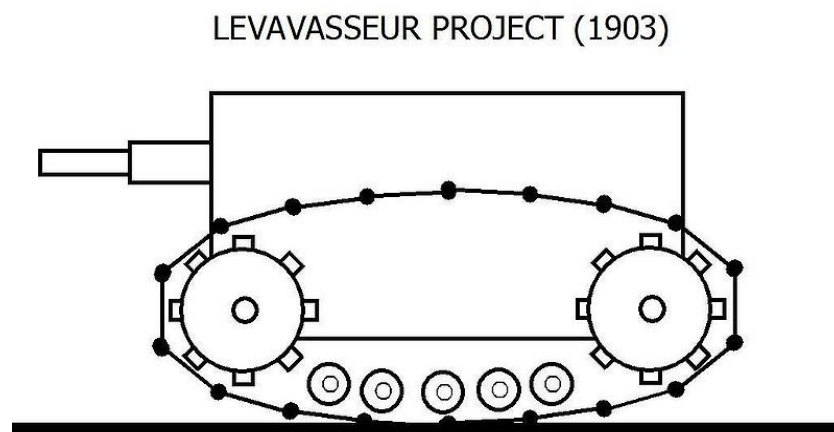


Figure 1.2. Primitive tank.
(Source: wikipedi, 2011).

Research area of armors so expanded that the investigations went forward in several branches: body, ground and air vehicles, for the same aims: lighter weight, more protection and appropriate production cost.

After World War I, plenty of metallic armor design was tried for both body armor configuration and tanks. Aluminum and steel have been widely used in metallic armor systems. Wars generally cause innovations in design and war tactics as in World War II, producing important concepts of armored tanks which even persist to this day. Steel was the earliest type of armor. The Germans pioneered the implementation of surface hardened steel during World War II, cotton, pressed steel plates silk were

produced in England and the Soviets also accomplished improved ballistic protection with sloped armor. On the other hand, aluminum is usually preferred against low caliber projectiles and shrapnel (Elaldı, 1997; global security, 2011; vikipedi, 2011).

Up to 1950s and 1960s mechanical properties of metallic armor materials were improved. Penetration mechanics and ballistic performances of metallic and metal-based materials such as metallic honeycomb containing armors were explored. It has been confirmed that there is no single material that meets the essentials of armor design such as high ballistic performance, strength and weight-cost effectiveness.

Integration of non-metallic materials into armors led to creative ideas. In the Korean War, siliceous-cored armor which contained a plate of fused silica glass between rolled steel plates was developed for tanks. Then, lightweight materials for ballistic protection were deeply investigated in 1960s and 1970s. While research was conducted on metal backed ceramic composite armors, in 1967, Soviet T-64 tanks pioneered a new armor material design. This armor design, Combination K, is composed of a glass-reinforced plastic sandwiched between inner and outer steel layers. Ceramic was realized to be an ideal face material in armor design due to its superior mechanical properties and ballistic resistance which will be explained in details further. Later on, T-64 tanks were modified where boron carbide-filled resin combined design appeared. In 1970s, Kevlar being used recently was applied into body armor. Kevlar is a lightweight and strong para-aramid (poli para fenilen terepitemid) woven synthetic fiber invented in 1965 by Kevlar. Kevlar bullet proof vests have been the premium choice of body armors for years (Figure 1.3). Furthermore Kevlar is used in some other specific areas such as land and air vehicles.(Viechnicki et al., 1991; Elaldı, 1997; wikipedia, 2011).

In 1980s, in order to increase the ductility and fracture toughness of ceramics, some materials were added to alumina, purity of monolithic ceramics such as Al_2O_3 changed, ceramic metal composites (CMC) were developed. Nevertheless, this method could only provide limited increment in ballistic performance of armor where these aforementioned ceramics used. Also, CMC was not as cost effective as improved monolithic ceramics. Thus, improved ceramics supported by various backing plates were tried in order to increase ballistic performance of armors (Viechnicki et al., 1991).

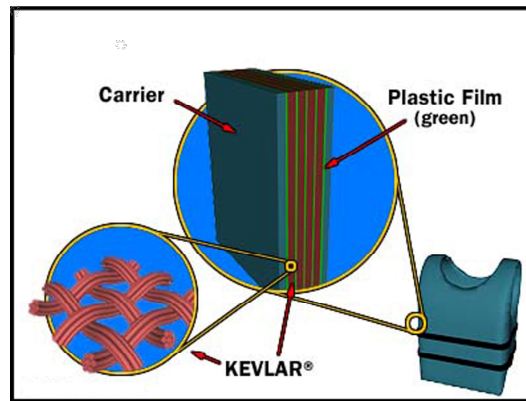


Figure 1.3. Kevlar body armor.
(Source: how stuff works).

Since 1990s major components of armors have been well defined: a ceramic layer backed by a composite plate. Within the new millennium, two brilliant ideas appeared. One of them was to insert light-weight materials between ceramic and composite plates. The other was to impregnate Kevlar with shear thickening fluid in order to increase mechanical properties of backing plate (Figure 1.4). As expected, when used with Kevlar, shear thickening fluid results in a stronger and lighter structure. Its working principle likes custard, the molecules of the fluid inside the liquid are locked after strike (how stuff works, 2011; gizmag, 2011). These brilliant ideas, which have been in progress recently, have increased the ballistic-weight performance of armor. Kevlar with shear thickening fluid provides better ballistic protection against some projectiles, but except armor piercing threats. Hence, to increase ballistic protection against armor piercing projectiles without sacrificing light weight, light-weight materials have been inserted ceramic and backing plate. The main purpose behind it is that, ceramic is fragmented more efficiently and magnitude of stress wave transmitted to backing plate is reduced.

Combination of materials in composite armor systems is a challenging subject and requires deep knowledge about the properties of candidate materials. Ceramic is relatively expensive and testing these materials for different configurations are time and money consuming. Thus, cost effective numerical methods have been used to get detailed information about the ballistic performance of the armor system since 1960s. Wilkins (Viechnickie et al., 1991) simulated the ceramic armor penetration almost for the first time. In his simulation, armor consisted of two layers; a hot pressed boron

carbide or liquid-phase sintered alumina in the front and doron (a glass reinforced plastic) in the back.

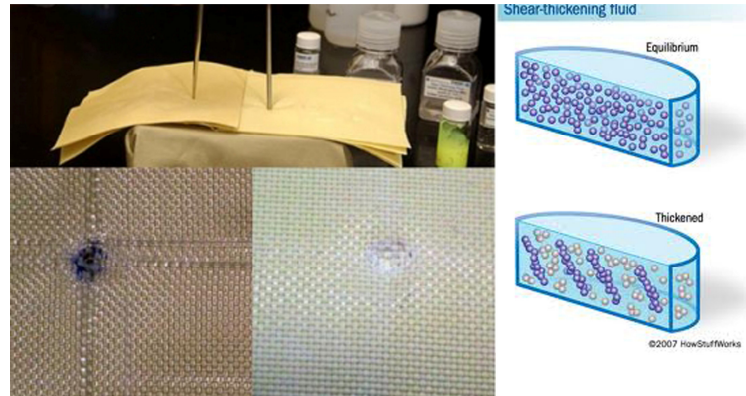


Figure 1.4. Kevlar with shear thickening fluid.
(Source: gizmag, 2011; how stuff woks, 2011).

In this study, to increase the ballistic performance of multilayered armors, three different materials: EPDM rubber, Teflon and Aluminum metallic foam were placed between ceramic front layers and composite backing plates. To validate the effectiveness of those materials, ballistic tests and corresponding numerical simulations, and impact chamber tests were conducted. This methodology provided detailed stress wave propagation analyses in multilayered armor systems and allows investigating the effect of some parameters which cannot be observed experimentally. Considering the results of the methodology explained above, promising interlayer materials were determined in terms of their ballistic performances and these materials were compared in themselves at equal areal densities.

CHAPTER 2

TYPES OF ARMORS

Armors can be categorized into two basic groups: monolithic and composite armors. Monolithic armors, which are conventional, consist of single material, generally metal. They are not sufficient since there is no material that meets the design necessities. They were widely used until multilayered armors were developed. A multilayered armor, consisting of different constituents, was formed by adaptation of non-metallic materials into armor configurations.

2.1. Monolithic Armors

Aluminum and steel are widely used in monolithic armor systems. Aluminum is usually preferred against low caliber projectiles and shrapnel whereas steel, the earliest type of armor, have been used for protection from more destructive ones. The Germans pioneered the implementation of surface hardened steel during World War II and the Soviets also accomplished improved ballistic protection with sloped (angled, neither vertical nor horizontal) armor. World War II advancements also increased the usage of homogeneous steel, high hardness levels approaching to 320-380 BHN, armor with the development of shaped-charge warheads.

Although The Food Machinery Corporation (FMC) used 5083 aluminum (aluminum-manganese-magnesium) alloy in production of M113 armored personnel carrier due to its effectiveness on shrapnel fragments, its ballistic protection to high velocity projectiles was inadequate. In 1960s 7039 aluminum (heat treated aluminum-zinc-magnesium) armors having 150 BHN were developed. Despite effectiveness to shrapnel and low caliber projectiles, this material was prone to stress corrosion cracking. Hence, 2519 aluminum (aluminum-copper-magnesium) armors were developed as an alternative.

Another type of material used in armor systems is hardened double alloyed steel, developed during World War I. However, between 1930 and 1960, it had almost never been used. Its hardness approaches to 600 BHN and has maximum mass effectiveness

(the relative difference in the mass of the target) where aluminum alloys cannot reach when 7.62 A.P. projectiles used, see Table 2.1 (Wikipedia, 2011; Elaldi, 1997).

Table 2.1. Selected mechanical properties of monolithic armors.
(Source: Elaldi, 1997).

Armor	Density	Areal Density	Mass Effectiveness
Steel Armors			
• RHA (380 BHN)	7830	114	1.00
• High hardened steel (550 BHN)	7850	98	1.16
• Double hardened steel (600-440 BHN)	7850	64	1.78
Aluminum Armors			
• 5083	2660	128	0.89
• 7039	2780	106	1.08
• 2519	2807	100	1.14

Beginning from 1960s, after the manufacturing of “Cadloy” type of high hardness steel protective against 7.62 A.P., high hardness steels have been widely used for armored personnel carrier. Hardening is a brilliant idea for metallic armor applications. Since, as the hardness of steel increases, the required thickness of the plate for the same ballistic protection level decreases and accordingly, mass effectiveness increases up to an optimum value.

Similar to high hardness steel, double hardened steel armors were developed in 1930s. Though, due to high production costs they have not been widely used. They are still in use but not in the igle vehicles because weight reduces maneuverability. Instead, they are used for load bearing applications, recently (Elaldi, 1997; wikipedia 2011).

2.2. Ceramic-Metal and Ceramic-Composite Armors

Penetration mechanics and ballistic performance of metallic and metal-based materials were explored and well known. However, available armors could not supply weight-cost effectiveness and ballistic performance together. Weight reduction without sacrificing performance led searchers to try nonmetallic materials.

Although brittleness of single ceramic layer results in spalling after impact, multilayered armor consisting of ceramic backed by a plate gives superior ballistic performance as it is seen in the Table 2.2. Since, the mechanical response of alumina at intermediate velocity regimes increases erosion as explained in detail further. Accordingly, researchers have been focused on these multilayered armors since 1950s. The milestones in the use of ceramic in armor applications are given chronologically in Table 2.3.

Table 2.2. Mechanical properties of composite armors.
(Source: Elaldi, 1997).

Armor	Density	Areal Density	Mass Effectiveness
Alumina (AD90)	3560	-	-
Alumina+5083 Aluminum	3125	50	2.28
Alumina+7020 Aluminum	3200	42	2.75
Alumina+E-Glass/polyester	2556	46	2.48
Alumina+Kevlar	2000	38	3.0
Boron carbide+Aluminum	2564	35	3.26
Titanium diboride	4450	-	-

In the Korean War, siliceous-cored armor containing a plate of fused silica glass between rolled steel plates was developed for tanks. The stopping power of glass exceeds that of armor steel on a thickness basis and in many cases glass is more than twice as good as steel on a thickness basis. Then, lightweight materials for ballistic protection were deeply investigated in 1960s and 1970s during the Vietnam War. While

research was conducted on ceramic- metal armors, in 1967 Soviet T-64 tanks pioneered new armor material design. This armor design, called as Combination K, is composed of glass-reinforced plastic sandwiched between inner and outer steel layers. However, ceramic was confirmed to be an ideal face material in armor design due to its ballistic resistance and lightweight and T-64 tanks were modified, boron carbide-filled resin combined design appeared. (wikipedia, 2011 ; Elaldi, 1997; and Viechnicki et al., 1991)

Since 1970s alumina ceramics have been improved and combined with various materials. Ceramics backed by metal plates were widely used until development of ceramic-composite armor of which backing plate consisting of fibers bonded by resin. Due to light weight, low cost, ductility, high and tailored strength in different directions, ceramic-composite armors have become widespread. Fibers of the backing plate were generally made of E-Glass, S2-Glass and Aramid (Kevlar etc.) (Elaldi, 1997). They were bonded with epoxy or polyester resins.

Since 1990s major components of armors have been well defined: a ceramic layer backed by a composite plate. After this step, to obtain lighter armors with higher performance, innovative design was needed. Materials having low acoustic impedance began to be inserted between ceramic and backing plate. Since this interlayer cause acoustic impedance mismatch and accordingly, portion of reflected compression waves from ceramic-interlayer interface is increased. Acoustic impedance mismatch phenomena and the studies about interface materials are given in detail further. The armor technology has been in progress to reach the most effective design.

The main drawback while developing the multilayered armors is a complex task. To overcome this problem, Wilkins, for the first time, simulated the ceramic armor penetration in 1968. In his simulation, layered armor consisted two layers; a hot pressed boron carbide or liquid-phase sintered alumina in the front and doron (a glass reinforced plastic) in the back. From now on, these numerical and analytical studies have been in parallel to experimental work.

Table 2.3. History of modern armor.
 (Source: Viechnickie et al., 1991).

Year	1940	1950	1960	1970
Technical Milestone	Armor with Glass/doron tested	Siliceous core armor	Alumina/doron	Various ceramics tested
Application	Aircrafts	Tanks	Personnel aircraft	
Threat	Small arms Shell fragments	Cannonballs	Small arms	Small arms and A.P.
Year	1980	1990	2000	
Technical Milestone	Improved ceramics Various DA (Dept. of Army), DN (Dept of Navy), DAF (Dept. of Air Force), R&D programs DARPA,/A/AA (armor, antiarmor) program armor design			
Application	Ground vehicles aircraft			
Threat	Long rod penetrators, Chemical energy munitions		electromagnetic gun	

2.3. Basic Concepts of Multilayered Armors

To explain the working principle of multilayered armors, impact characteristics of ceramic must be well understood. Since, the majority of projectile kinetic energy is absorbed by the ceramic debris and greater portion of stress wave is reflected back from the ceramic interface during ballistic hit. Moreover, to understand the effect of interlayer on ballistic performance, which is the motivation of the current study, wave reflection and transmission characteristics of layers have to be investigated through.

2.3.1. Impact Characteristics of Alumina

Ballistic impact is a dynamic phenomenon and greatly occurs within a few hundred microseconds. During such a short time, main functions expected from the face material are; to absorb the projectile's kinetic energy and lower the magnitude of transmitted stress to the backing plate. Besides having relatively low density, ceramic fulfills the mentioned requirements of armor face material. Since it has high strength under compression and still retains its high strength even after fracture under compressive loading.

The ballistic response of a ceramic layer when backed by a plate can be classified into three main groups in terms of the penetrator velocity. At low velocities ($V < 700$ m/s), dynamic mechanical properties effect penetration. Thus, ceramic layer is fractured after impact and accordingly, it cannot be efficiently utilized in the process (Figure 2.1). More ductile materials such as metal face plates are more efficient, preferable at low impact speeds.

At hypervelocities (3000 m/s $> V$) ceramic is insufficient on energy absorption since hydrodynamic properties of materials play role within this regime. Projectile and ceramic flow as if they are fluid. Ceramic again cannot be efficiently utilized.

At intermediate velocities, (700 m/s $< V < 3000$ m/s) dynamic material properties play important role while hydrodynamic flow occurs (Figure 2.1). In this velocity regime, where projectile impact velocity is evolved, four different steps occur (Figure 2.2 (a)): First, projectile impacts and penetrates into alumina thereby hydrodynamic flow occurs in both alumina and penetrator (Viechnickie et al., 1991).

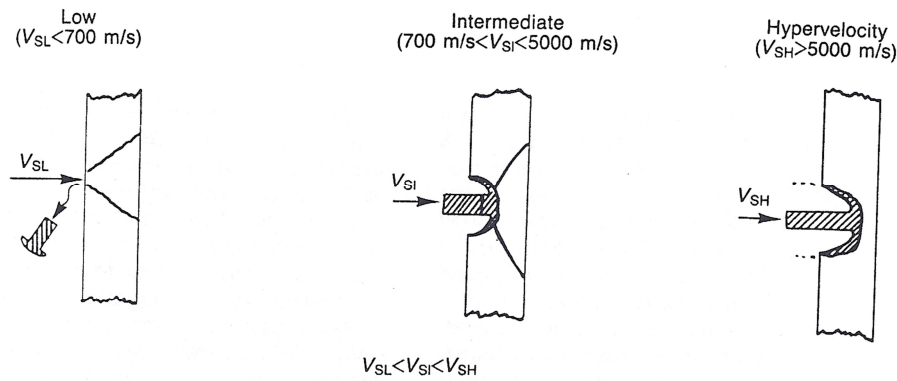


Figure 2.1 Impact response of armor ceramic under different velocities.
 (Source: Viechnickie et al., 1991).

Hence, a conical fracture pattern occurs in alumina in the vicinity of impacted zone and propagates toward ceramic-composite/interlayer interface while ceramic debris, which deforms the tip of penetrator, appears (Figure 2.2 (b)). Besides, compression waves are generated. Then some portion of these waves is transmitted to the backing plate, while the remaining reflects back from ceramic-composite/interlayer interface as tension. These reflected waves result in radial cracks while conical, high compressive stress region of fully fragmented materials developed at the impacted zone, named Hertzian cone (Figure 2.2 (c)). Since, ceramic is pulverized (dissipated into debris) and flow of penetrator continues during this time. As fracture of ceramic increases and this conoid zone widens and the interaction between penetrator and ceramic debris increases, accordingly, penetrator is eroded (Figure 2.2 (d)).

Fracture of ceramic absorbs insignificant amount of energy whereas development of the conical zone consisting of ceramic debris plays vitally important role in defeating projectile and energy absorption. This debris has to be supported so that it does not spread out. The main functions of backing plate is to support debris absorb the remaining kinetic energy and accordingly stop the penetrator. When the backing plate deforms, the remaining energy is absorbed. Metal: aluminum, steel, or titanium, and composites have been used as backing plate.

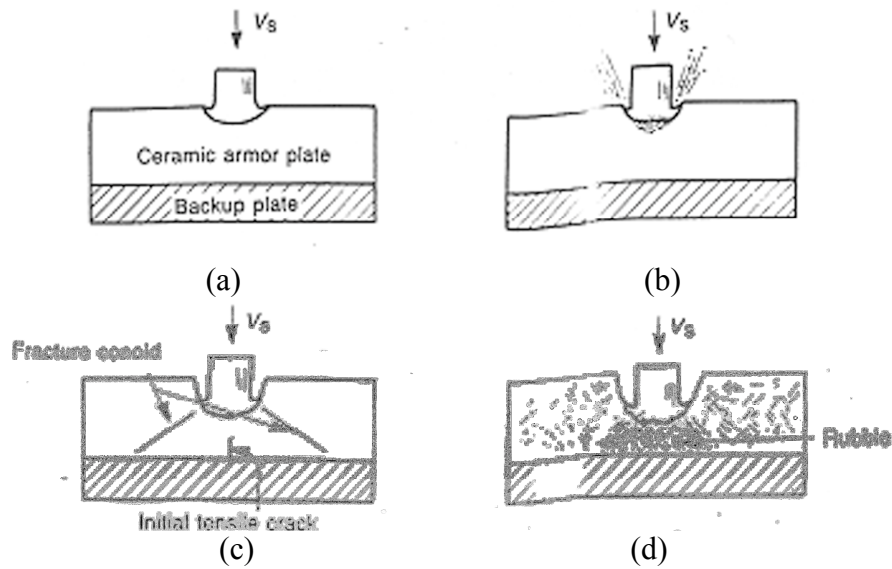


Figure 2.2. Four stages of projectile penetration into ceramic armor. (Source: Viechnickie et al., 1991).

2.3.2. Acoustic Impedance Mismatch

As explained before, wave propagation is a significant concept in the ballistic impacts. It is effective in the fracture mechanism of ceramic and energy absorption of armor. Hence, wave reflection of stress waves at boundaries plays important role in ballistic impacts.

There is a relation between wave reflection and acoustic impedance as seen in Figure 2.3. Hence, an interlayer between front and backing layers is inserted to alter the wave propagation characteristics and consequently the ballistic performance of the armor system by increasing acoustic impedance mismatch:

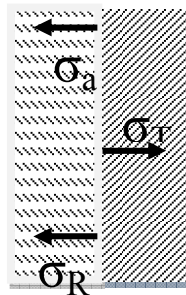


Figure 2.3. Wave reflection.

For the one dimensional elastic wave case force and velocity equilibriums are given in the equations below where “a”, “R and “T” refer to compressive wave striking an interface, reflected and transmitted waves (Smith and Hetherington, 2003):

$$\sigma_T = \left(\frac{2\sqrt{E_2\rho_2}}{\sqrt{E_1\rho_1} + n\sqrt{E_2\rho_2}} \right) \times \sigma_a \quad (2.1)$$

$$\sigma_R = \left(\frac{n\sqrt{E_2\rho_2} - \sqrt{E_1\rho_1}}{n\sqrt{E_2\rho_2} + \sqrt{E_1\rho_1}} \right) \times \sigma_a \quad (2.2)$$

$$n = \frac{A_2}{A_1} \quad (2.3)$$

Where ρ (kg/m³) is density and C (m/s) is the sound speed which is a function of mechanical properties of the material and is independent of the amplitude of the sound wave. Accordingly, wave reflection is equal to:

$$R = \frac{\sigma_R}{\sigma_a} = \frac{n\sqrt{E_2\rho_2} - \sqrt{E_1\rho_1}}{n\sqrt{E_2\rho_2} + \sqrt{E_1\rho_1}} \quad (2.4)$$

Acoustic impedance (Z) can be found by the following formulas based on Hooke's Law and Newton's Second Law:

$$Z = \sqrt{E\rho} \quad (2.5)$$

Wave reflection is referred to acoustic impedance mismatch and it depends on the acoustic impedance differences of materials, as seen in the Equation 2.7 where Z_1 and Z_2 illustrate acoustic impedances of the boundaries in contact

$$R = \frac{nZ_2 - Z_1}{nZ_2 + Z_1} \quad (2.6)$$

Table 2.4, density, elastic modulus and acoustic impedance of the armor constituents are given, as can be seen, acoustic impedance of ceramic is high. Materials with relatively low acoustic impedances were placed between ceramic and composite backing plate in the current study.

EPDM rubber is a highly non linear material and acoustic impedance of it is not constant. When the armor structure is concerned the acoustic impedance and mismatch between ceramic and EPDM rubber is initially high. However, this mismatch ceases out during compression as the elastic modulus of EPDM rubber rapidly and stiffness increases.

Table 2.4. Acoustic impedance values of armor constituents used in current study.

Material	Density (kg/m³)	Elastic Modulus (GPa)	Acoustic Impedance (10⁵ kg/m²s)
EPDM rubber	1200	*~0.007 (initial)	~0.9
Teflon	760	*~0.025 (initial)	~1.38
Aluminum foam	438	*~0.177 (initial)	~2.78
Alumina ceramic	3890	370	379.38
E-Glass Composite	1850	11.8	46.72

* Elastic moduli of the materials are not constant.

2.4. Literature Survey

Conventionally, armor systems have been monolithic, typically composing of a high strength hard steel plate (Sorensen et al., 1991; Gupta and Madhu, 1992; Littlefield et al., 1997; Borvik et al., 1999; Abrate, 2009). However, there is an increasing demand for the armor materials providing maximum ballistic protection at a minimum weight. Over the years, ceramics and polymer matrix composites have been increasingly incorporated into armor protection systems (Anderson and Morris, 1992; Anderson et al., 1996; Collombet et al., 1998; Davies and Zhang, 1995; Deka et al., 2008; DeLuca et al., 1998; Kumar and Bhat, 1998; Shokrieh and Javadpour, 2008; Yadav and Ravichandran, 2003). The composite armor, which is also known as integrated multilayered armor system, is composed of a hard facing front layer of ceramic tiles and a fiber reinforced composite backing plate. The main function of the hard front ceramic layer is to reduce the local pressure imposed to the backing composite plate, by deforming and eroding the projectile. The composite backing plate absorbs part of the kinetic energy of the projectile. Metallic plates were also investigated for the backing plate in multilayered armor systems (Gooch et al., 1999; Liu et al., 2003; Lopez-Puente et al., 2005; Roeder and Sun, 2001; Sadanandan and Hetherington, 1997; Zhang et al., 2010). Several studies concern efforts to investigate the penetration analysis of multilayered targets. (Sherman, 2000; Sherman and Ben-Shushan, 1997; Abrate, 2009).

When a projectile hits the ceramic layer at a relatively high velocity, a compressive stress wave is generated and it propagates from the projectile hit/impact zone in the impact direction. Once this compressive wave reaches the back face of the ceramic layer, it is partially reflected back as tensile wave, causing the damage in the ceramic layer. Several studies have investigated the stress wave propagation in the composite armor both analytically and numerically (Abrate, 2003; Bruck, 2000; Gama, 1998; Mines, 2004). The acoustic impedance mismatch between the ceramic and composite layer plays a key role in the ballistic performance of the armor system. The insertion of an interlayer in between these two layers significantly alters the wave propagation characteristics and consequently the ballistic performance of the armor system. Gama et al. (Gama et al., 2000; 2001) studied through-thickness wave propagation and the effect of rubber interlayer in an integrated composite armor system. It was reported that the rubber interlayer ensured a good resilient bond between the

ceramic and composite and also enhanced the multi-hit capability. It was shown that the composite armor with an Aluminum foam interlayer produced more extensive ceramic fragmentation and less volumetric delamination of the composite plate (Gama et al., 2001). The effect of adhesive interlayer thickness on the ballistic efficiency of alumina/aluminum armor system was investigated numerically and experimentally (Lopez-Puente et al., 2005; Zaera and Sanchez-Galvez, 1997; Zaera et al., 2000). It was shown that the thicker layer of adhesive resulted in a wider plastic deformation area of the metallic backing plate and earlier shattering of the ceramic layer. The effects of wave speed, layer geometry and the mechanical properties of the layers on the load distribution between the layers were further investigated numerically (Gupta and Ding, 2002; Robbins et al., 2004). It was shown that a single, thick, high strength and high wave speed layer for a fixed layer thickness provided the best lateral load spreading through intense and rapid wave transmission.

As the multilayered armor systems are becoming increasingly complex, the analysis of the wave propagation between the layers requires both modeling and experimental investigations. Previous studies have provided the first precise theoretical and experimental insights into the details of the stress wave propagation in these materials (Tasdemirci and Hall, 2005; 2007a; 2007b). The Split Hopkinson Pressure Bar (SHPB) was used as a probe for generating entry and exit of the stress waves of known characteristics. These known, measured, entry and exit waves were then reproduced in a finite element model of the multilayer material. It was confirmed that when the model data matched the output data from the bars, the model was accurately describing the stress-state within the multilayer material including single, double and triple layered materials. These studies were mainly focused on the mimicking the initial few microseconds; however, during the course of ballistic impact, several different deformation and failure mechanisms involved, making the full penetration analysis of multilayer armor inevitable. Previous studies published on the penetration analysis of the armor systems are also noted to be limited to plates without an interlayer. The primary aim of the present work was to develop 3D finite elements models of armor systems with different interlayer materials in order to demonstrate the effect of interlayer material on the stress wave propagation in multilayer composite armor systems.

2.5. Motivation

Up to now, most of the studies that have published on the penetration analysis of armor systems are limited to the cases without an interlayer. The primary thrust of the present work was, therefore, to develop 3D finite elements models of armor systems with different interlayer materials to demonstrate the effect on stress wave propagation of interlayer material in the multilayer composite armors.

The main purpose of the current study is to investigate the effect of interlayer material on the ballistic performance of composite armor and stress wave propagation both experimentally and numerically. In this study generally experiments and numerical simulations were conducted simultaneously thereby, the advantages of both techniques were used together. To increase the ballistic performance of multilayered armors, three different materials with low acoustic impedances: EPDM rubber, Teflon and Aluminum metallic foam were placed between ceramic front layers and composite backing plates. To validate the effectiveness of those materials at relatively high velocities, ballistic tests and corresponding numerical simulations whereas to validate at low velocities compressed air gun tests were conducted. Considering the results of the methodology explained above, promising interlayer materials were determined in terms of their ballistic performances and these materials were compared in themselves at equal areal densities. Hence, the most effective layer could then be selected and effect of interlayer thickness could be demonstrated.

CHAPTER 3

EXPERIMENTAL SETUP

3.1. Test Methods

The mechanical characterization tests conducted in this study can be categorized into two main groups: quasi-static and SHPB tests. Strain rate sensitivities of the components were defined and stress-strain curves were obtained. This data was further used during numerical modeling which will also be described in detail somewhere in this thesis. A second group of tests was also conducted to observe the ballistic impact response of armor systems; ballistic impact and compressed air gun tests. Improved armor designs were shot at different velocities. Compressed air gun (impact chamber) tests were carried out to understand the behavior of armor system at relatively low speeds, 150-200 m/s, while ballistic tests were done at significantly higher impact speeds, 800 ± 50 m/s, using armor piercing projectiles.

3.2. Tests for Mechanical Characterization

The mechanisms governing the deformation behavior of materials can be classified in terms of strain rate, as shown in Table 3.1. At strain rates between 10^{-6} and 10^{-5} s^{-1} , creep is the dominant deformation behavior whereas between 10^{-4} and 10^{-3} quasi-static mechanical properties are dominant. In the order of 10^{-1} to 10^2 , strain rate is accepted as intermediate levels. Within this regime, strain rate effects also exist to some extent but generally are at negligible order. From 10^2 to 10^5 , rates are accepted as high. At high strain rates, inertia forces and wave propagation effects are prevailing. Above 10^5 s^{-1} and higher, shock wave propagation through the material occurs and most commonly observed in plate impact tests.

Test techniques and machines for material characterization differ regarding the required strain rate levels, as given in Table 3.1. For instance, creep is the behavior of material when exposed to constant or steady loading for long times. Hydraulic or screw

machines are used specifically for inducing constant strain rates during the test. Drop-weight testers use pneumatic mechanisms for offering controllable fall distances to observe material responses at intermediate strain rate levels. Above certain rate (10^2 - 10^4 s^{-1}) levels, stress wave propagation plays a significant role during deformation as explained before. Split Hopkinson Pressure Bar (SHPB) is used to generate elastic wave signals called incident and transmitted waves during impact. Above 10^4 s^{-1} strain rate, shock waves may occur. This type of loading can be applied during plate impact tests. In this study, quasi-static and SHPB tests were conducted to observe the material behavior at different rates.

3.2.1. Quasi-Static Tests

Quasi-static test apparatus apply uniaxial tension or compression type of loading and measures force-displacement. Formulas given below transform force-displacement data into stress-strain data, a valid description of material behavior at constant strain rate. Since quasi-static test is displacement controlled, strain rate remains constant during the deformation. A 30 kN Shimadzu AG-I testing machine was used for quasi-static tests at 10^{-3} s^{-1} strain rate (Figure 3.1).

$$\sigma = \frac{P}{A} \quad (3.1)$$

$$\varepsilon = \frac{\Delta l}{l_0} \quad (3.2)$$



Figure 3.1. Quasi-static testing apparatus.

Table 3.1. Dynamic aspects of mechanical testing.
(Source: Zukas et al., 1992).

						Strain Rate (s^{-1})
10^{-4}	10^{-2}	10^0	10^2	10^4	10^6	
Quasi-static	Inter- mediate		Bar impact	High- velocity plate impact		
Hydraulic (servohydra- ulic) or screw machine	Pneumatic or mechanical machines (Cam plastometer and drop test)		Mechanical or explosive impact (SHPB)	Light- compressed air gun or explosive driven plate impact (Taylor impact test)	Usual method of loading	
Constant strain-rate test	Mechanical resonance in specimen and machine		Elastic-plastic wave propagation	Shock-wave propagation	Dynamic consideration in testing	

3.2.2. High Strain Rate Testing and Split Hopkinson Pressure Bar

Split Hopkinson Pressure Bar is commonly used testing methodology for mechanical characterization of materials under dynamic loads due to its high accuracy and repeatability. A typical SHPB setup, invented by John Hopkinson, consists of four major mechanical components: two strong elastic bars called incident and transmitter, a gas chamber and a striker bar as shown in Figure 3.2. The specimen is sandwiched between incident and transmitter bars.

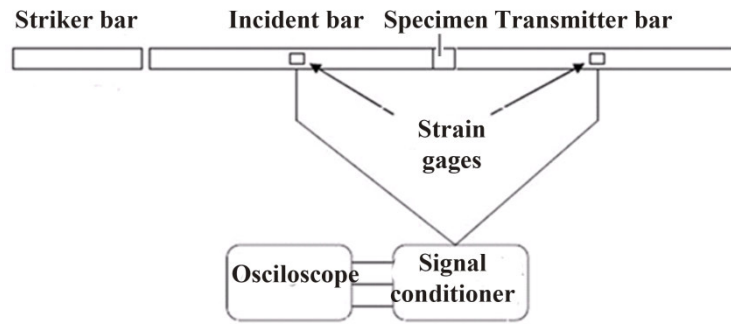


Figure 3.2. Schematic of SHPB.

Striker bar fired by gas gun hits the incident bar face and generates a rectangular well-formed compression stress pulse. This compression wave travels along incident bar towards the specimen interface. After this wave arrives to specimen, some part of it is reflected back as tension, while rest is transmitted to transmitter bar (Figure 3.3). Wave traveling back and forth through the incident bar is called incident (ϵ_I) and reflected (ϵ_R) wave, respectively. Adding that, wave arriving to transmitter bar is called transmitted wave (ϵ_T). These waves are recorded with the help of strain gages installed on bar surfaces. These gages are mounted on the bar surfaces at certain locations: same distance away from the specimen interfaces along both directions. For acquisition of the data, a signal conditioner and a digital storage oscilloscope are used. In Figures 3.4 and 3.5, typical Hopkinson Pressure bar signal and stress history of bars are shown.

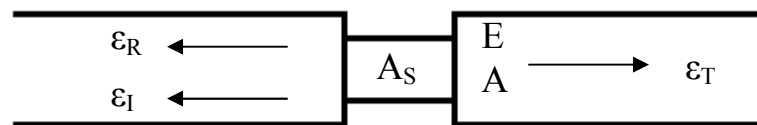


Figure 3.3. Schematic of specimen and waves.

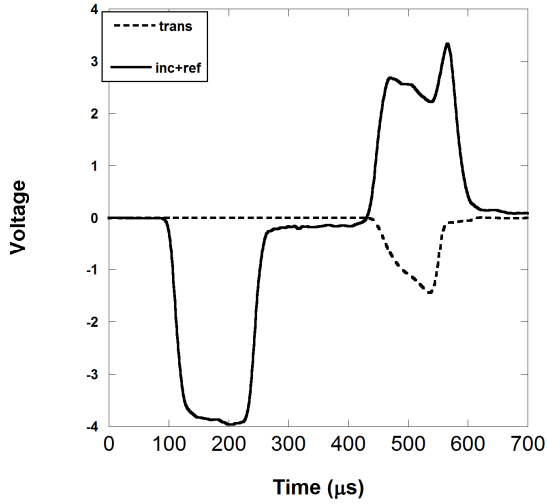


Figure 3.4. Typical SHPB signal.

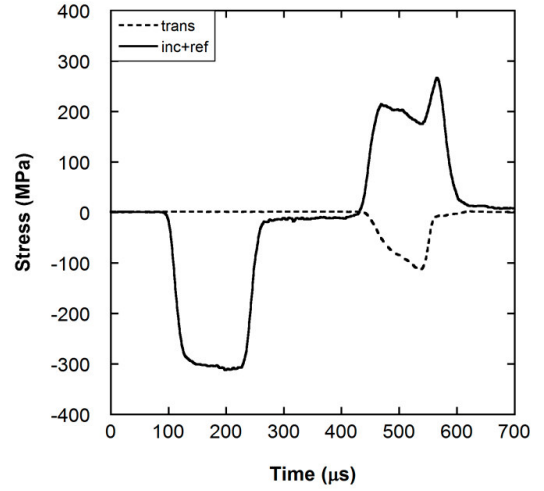


Figure 3.5. Typical stress history.

Stress, strain and strain rate of the specimen can be calculated by the following equations (Kolsky). The symbols A and A_0 refer cross sectional areas of specimen and output bars (incident and transmitter bars) whereas E_0 and C_0 refer to elastic modulus and wave velocity of bars whereas L denotes the length of specimen.

$$\sigma(t) = E_0 \frac{A_0}{A} \varepsilon_T(t) \quad (3.3)$$

$$\varepsilon(t) = -\frac{C_0}{L} \int_0^t \varepsilon_R d(t) \quad (3.4)$$

$$\dot{\varepsilon}(t) = -\frac{2C_0}{L} \varepsilon_R(t) \quad (3.5)$$

SHPB apparatus used through this study consists of CPM Rex76™ bars: a 350 mm long striker bar, a 3600 mm incident bar and 1800 mm transmitter bar, all with the same diameter of 20.35 mm (Figure 3.6). Mechanical properties of bars are given in Table 3.2. The multiple reloading of the samples in SHPB was avoided by using a transmitter bar shorter than the incident bar.

Table 3.2. Mechanical properties of bar material.
(Source: Ergöner, 2008).

Material	Density, ρ (kg/m ³)	Young's Modulus, E (GPa)	Poisson's Ratio, ν	Yield Strength σ_Y (MPa)
CPM Rex76	8255	214	0.3	700



Figure 3.6. SHPB setup.

A chronograph was also incorporated into the SHPB set-up to measure the striker bar velocity (Figure 3.7 (a)). It consists of two gates mounted on the striker path and a controller box. Once the striker bar arrives to the first gate, a TTL (transistor transistor logic which provides constant 5V signal) pulse, and when it arrives the second gate location second TTL pulse are created consecutively. The distance between the gates is preset and software automatically measures the time between these TTL pulses. Accordingly, software calculates impact velocity by dividing distance to the passage time.

Also, a high speed camera Photron FASTCAM SA.1.1 which can capture more than a thousand frames sequentially in 500,000 frames per second (fps) at most, was used during the tests to monitor the damage initiation in the specimen (Figure 3.7 (b)). This important information was further used while comparing the results of the numerical simulations with those of the experiments. To capture such an instantaneous

event, the camera was triggered with the TTL pulse generated from the chronograph. SHPB test generally takes about $700 \mu\text{s}$ and can be recorded by high speed camera with approximately $\sim 47 \mu\text{s}$ interframe time as seen in Figures 3.8 and 3.9.

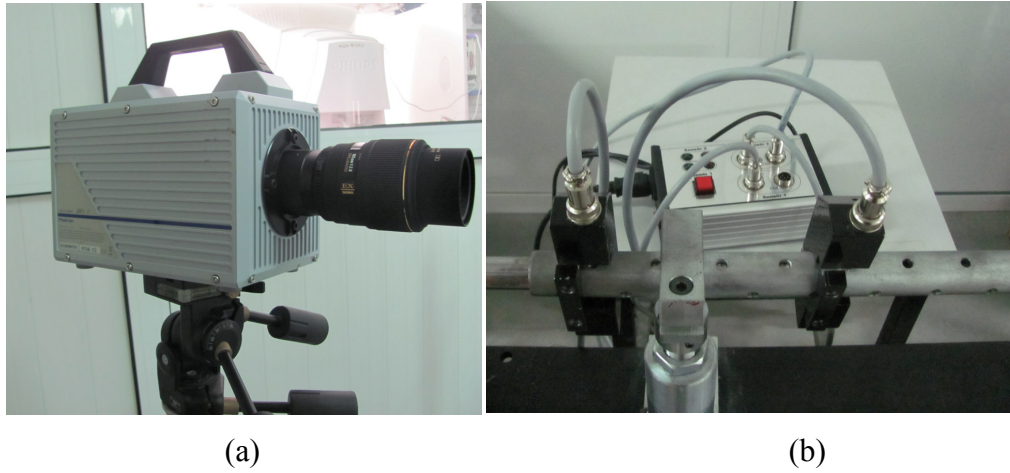


Figure 3.7. Chronograph and high speed camera.

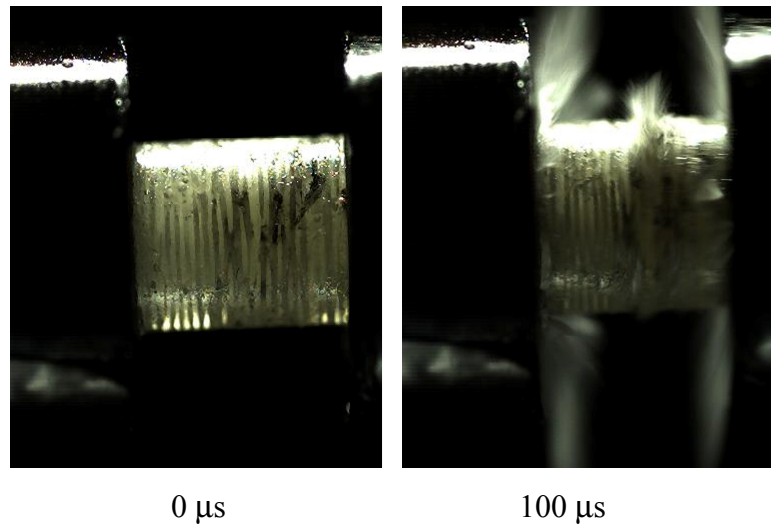


Figure 3.8. High speed camera images of 0/90 E-Glass/polyester composite tested in the through-thickness direction.

(Cont.on next page)

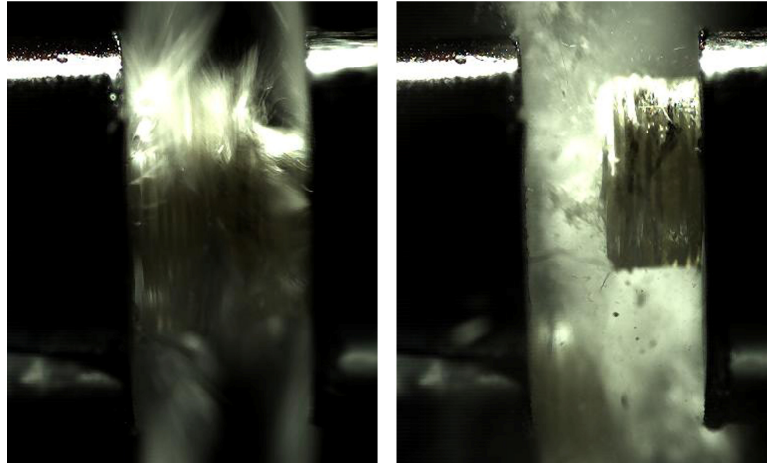
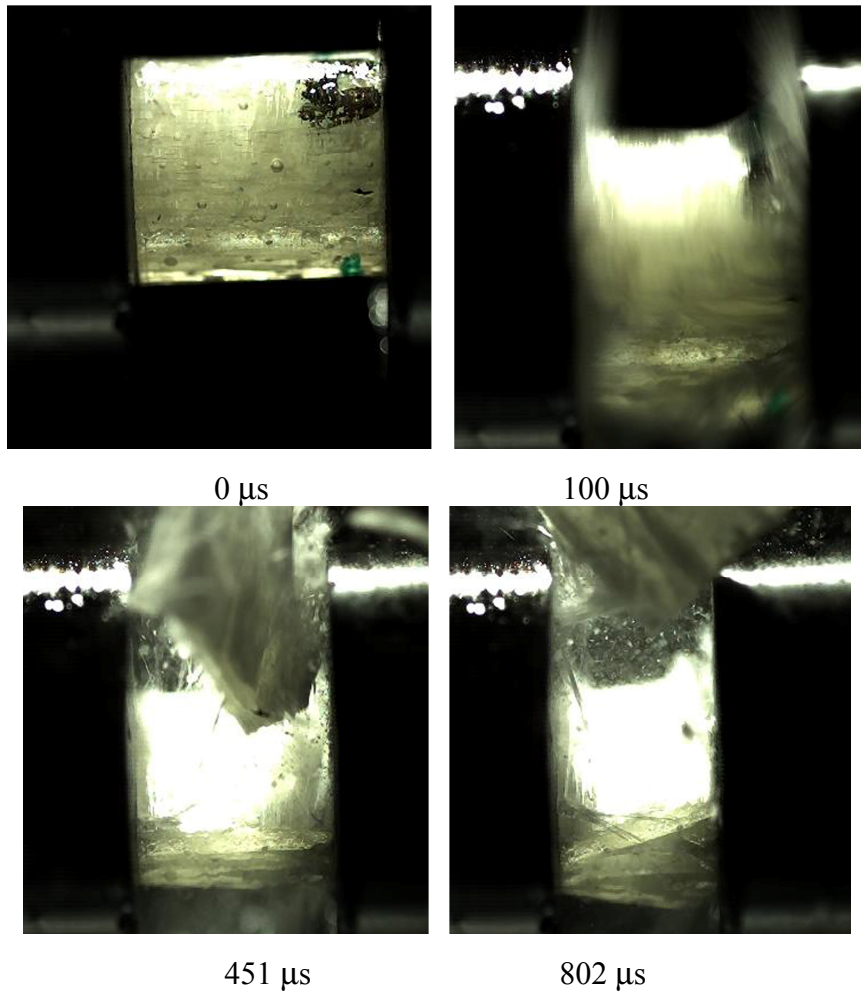


Figure 3.8. (Cont.) 200 μ s

570 μ s



0 μ s

100 μ s

451 μ s

802 μ s

Figure 3.9. High speed camera images of 0/90 E-Glass/polyester composite tested in the in-plane direction.

3.3. Penetration and Perforation Tests

While the mechanical response of a material can be well defined by conducting some testing methods, penetration behavior of a material still is not an easily obtainable characteristic. To understand this behavior, material has to be hit by a projectile. For this purpose projectile test setups are needed. Generally, high velocity penetration behavior (above 600 m/s) is investigated using A.P. projectiles, whereas low velocity (50-500 m/s) response is studied by conducting experiments using compressed air guns.

3.3.1. Ballistic Tests

Ballistic test set ups are relatively simple; a projectile is fired from a fixed rifle (Figure 3.10). Target is held by an armor holder, whereas rifle is fixed on table and projectile is automatically fired by pressing a trigger button. Target can be hit once or multiple times.

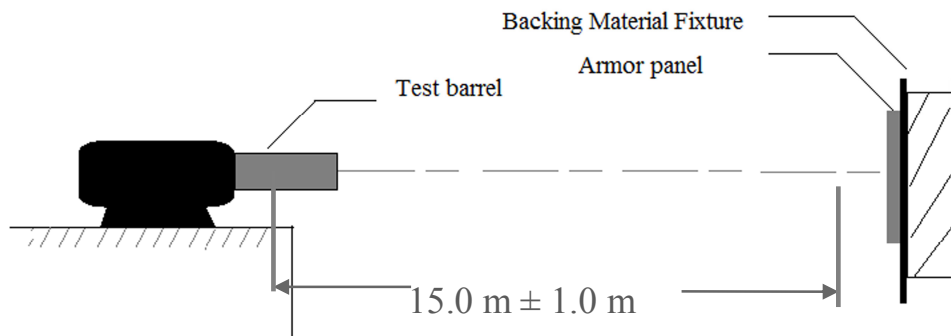


Figure 3.10. Ballistic test set-up.
(Source: National Institute of Justice, 2008).

In general, projectiles are used for different application purposes. Any item capable of being launched can be accepted as projectile and military projectiles form a subgroup of them. Small arm ammunition types of military projectiles which are used in ballistic experiments are called cartridges. They are used in machine guns, hand guns,

and rifles. Cartridge is a copper package containing projectile, casing, propellant, rim, and primer inside. The cartridges vary in terms of the diameter of rim, caliber i.e. 5.56, 7.62 and 14.5 mm. Furthermore, they can be classified into groups due to their nose shape. Standard or modified ball shapes and armor piercing types are generally in use. Armor types are considered to determine convenient projectile in ballistic tests.

Armors are categorized into four main types by level of ballistic performance as demonstrated in Table 3.4. Type I armors protect against .22 long rifle lead round nose (22 LR LRN) and .380 ACP full metal jacketed round nose (FMJ RN) bullets. It provides minimum protection level so increasing threats reduce use of it. Type IIA armor gives protection against 9mm full metal jacketed round nose (FMJ RN) bullets, at a minimum impact velocity of 332 m/s, and .40 S&W caliber full metal jacketed (FMJ) bullets, at a minimum impact velocity of 312 m/s beside type I armor threats. Type II armor protects against 9mm full metal jacketed round nose (FMJ RN) bullets with a minimum velocity of 358 m/s or less, and .357 Magnum jacketed soft point (JSP) bullets with a minimum velocity of 427 m/s (1400 ft/s) or less. It also protects against Type I and Type IIA threats. It is heavier and bulkier than Types I or II-A. Type III-A armor protects against 9mm full metal jacketed round nose (FJM RN) bullets, with a minimum impact velocity of 427 m/s or less, and .44 Magnum jacketed hollow point (JHP) bullets, with a minimum impact velocity of 427 m/s or less. It also protects against most handgun threats, as well as the Type I, II-A, and II threats. For daily routine of secure men, it provides highest level protection. Type III armor protects against 7.62mm full metal jacketed (FMJ) bullets (U.S. military designation M80), shot from rifles at a minimum velocity of 838 m/s. It also protects against Type I through III-A threats. Type IV armor protects against .30 caliber armor piercing (AP) bullets (U.S. military designation M2 AP), impacting at a minimum velocity of 869 m/s or less. It also provides at least single-hit protection against the Type I through III threats. Type IV armor provides the highest level of protection currently available. Since it is capable of resisting “armor piercing” bullets, it often contains ceramic materials inside (globalsecurity, 2011 ; National Institute of Justice, 2008).

In this study, experiments were conducted using the set-up in Mechanical and Chemical Industry Corporation, Ankara and each target was shot once with a 7.62 x 51 mm NATO A.P. M61 projectile to investigate ballistic resistance of multilayered armor

(Figure 3.11). Technical properties of 7.62 mm cartridge are given in Table 3.4. and as it is seen, velocity of 7.62 mm cartridges is generally in the range of 800-1000 m/s.

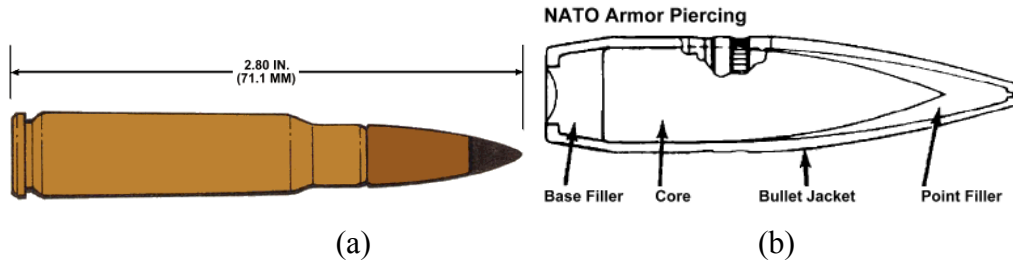


Figure 3.11. Schematic view of 7.62 x 51 mm NATO A.P. (M61) projectile. (Source: inetres, 2011).

Table 3.3. Technical properties of a 7.62 mm NATO A.P. projectile. (Source: inetres, 2011).

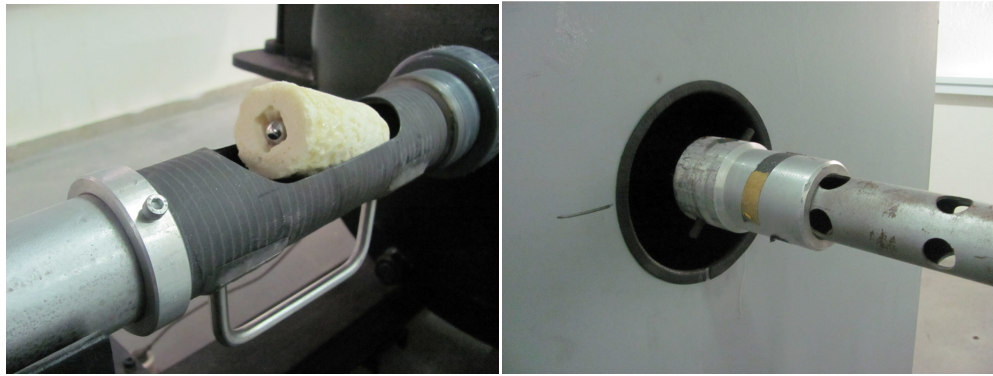
7.62 mm Cartridge				
Model	Cartridge Weight (g)	Cartridge Length (mm)	Projectile Weight (gr)	Velocity (m/s)
M61 AP	25.47	71.1	9.75	~ 838

3.3.2. Compressed Air Gun Tests

Compressed air gun test set-up consists of a rifle connected to a pressurized chamber (Figure 3.12). When the valve of the impact chamber is triggered, pressurized air is released, then a sabot carrying the projectile is set into motion. Projectile is carried by a sabot during its travel in the rifle then a scraper stops the sabot at the outlet end of the rifle and lets the motion of the projectile continues alone (Figure 3.13).

Table 3.4. Armor types and protection levels.
 (Source: National Institute of Justice, 2008).

Test Variables			
Armor Type	Bullet Description	Bullet Mass (gr)	Conditioned Armor Test Velocity (m/s)
IIA	9 mm FMJ RN	8	355
	.40 S&W FMJ	11.7	325
II	9 mm Luger FMJ RN	8	359
	.357 Magnum JSP	10.2	408
	.357 SIG TMJ	8.1	430
	.44 Mag JHP	15.6	408
III A			
III	7.62 mm NATO FMJ-SPIRE PT BT	9.6	847
	30.06 M2 AP FMJ-SPIRE PT AP	10.8	878
IV			
Special	Depends on manufacturer.		



(a)

(b)

Figure 3.12. Rifle constituents of compressed air gun set-up (a) Sabot (with steel ball projectile) (b) Scraper.

During the current study, an impact chamber equipped with a compressed air gun was used. A 25 x 25 cm steel armor holder was used to mount the targets as demonstrated in Figure 3.14. A steel ball projectile (100Cr6) in 12.7 mm diameter was fired during the tests at 180 ± 10 m/s velocity.

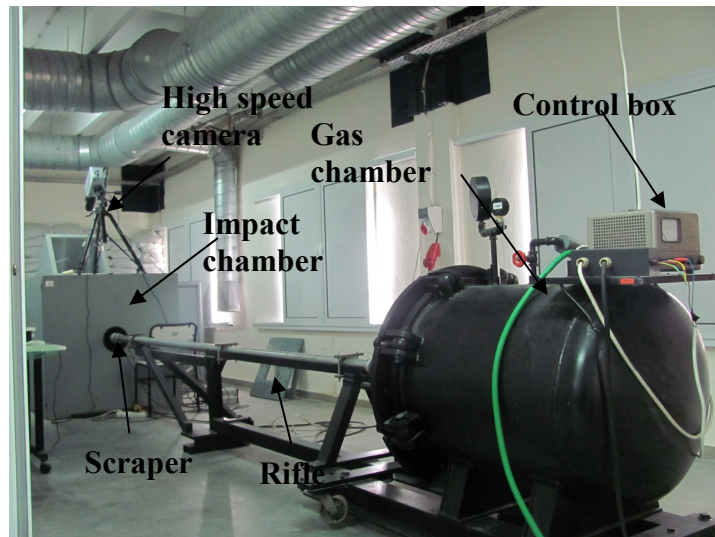


Figure 3.13. Compressed air gun set-up.

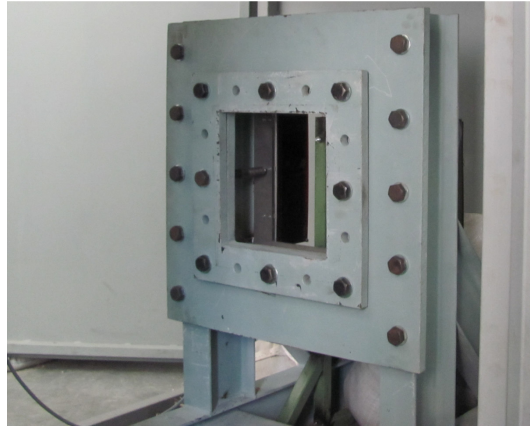


Figure 3.14. Armor holder.

As in SHPB testing, high speed camera was also used during compressed air gun experiments to observe the damage initiation and progression. 20000 fps speed and 512 x 416 pixels resolution provided sufficient images as seen in Figure 3.15 to attain approximately 50 μ s interframe time. The compressed air gun experiment images will be explained later.

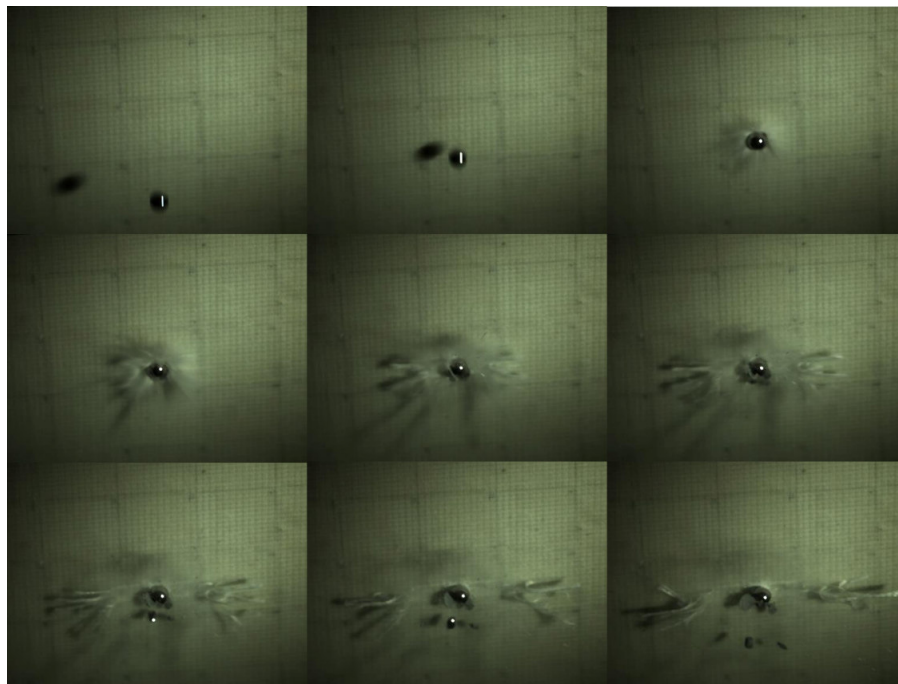


Figure 3.15. Sequence of captured images during compressed air gun experiment.

Camera was triggered with a chronograph integrated into compressed air gun set-up. This chronograph consists of an array of sensors, sweeping an area. The set of sensors enables user to record the terminal velocity, if perforation occurs of course (Figure 3.16).

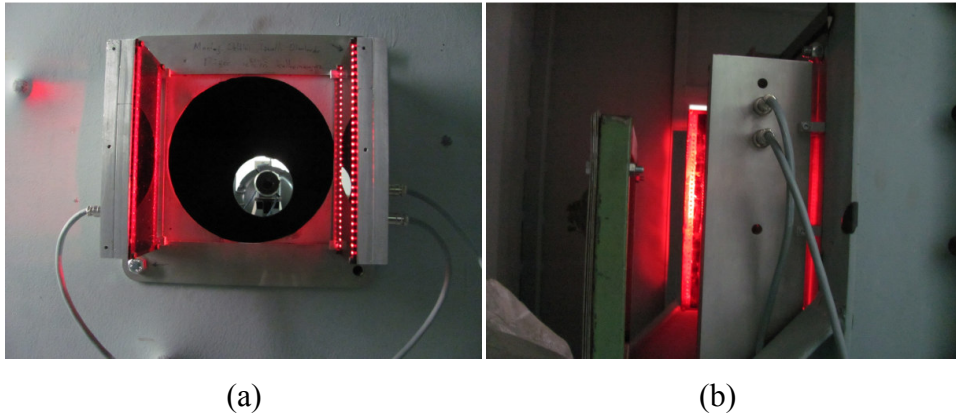


Figure 3.16. Chronograph used in compressed air gun test set-up.

CHAPTER 4

EXPERIMENTAL AND NUMERICAL STUDIES OF STRESS WAVE PROPAGATION IN ARMOR SYSTEM CONSTITUENTS

When exposed to impact loads, stress wave propagates through different layers of multilayered systems. Amplitude and shape of the stress wave propagating depend on layer thickness, dynamic mechanical properties of the layer itself and adjacent layers. In this chapter, dynamic mechanical properties of armor system constituents were determined by using a SHPB set-up.

LS-DYNA 971, within the LS-PrePost was used to numerically analyze armor configurations. In context of this chapter, appropriate material models were selected from LS-DYNA's material model library for each possible layer and the required model parameters were then determined.

Some model parameters were taken from previous the studies (Krashanitsa and Shakarayev, 2005; Ergöncü, 2008; Guden and Yuksel, 2006; Yuksel 2010; Tasdemirci 2005; Tasdemirci and Hall 2009; Xiao et al., 2007; Fawaz et al., 2007). Model parameters of 0/90 E-Glass/polyester layers were not in literature. Thus, SHPB and quasi-static tests of this composite were conducted to characterize of the material and determine the material model parameters. Single element 0/90 E-Glass composite model was conducted to define parameters that could not be determined experimentally. Then numerical and experimental work was conducted in parallel. SHPB model was created to confirm that material model parameters accurately describing the stress-state of experiments.

There was a good agreement between numerical and experimental results by using numerical simulations. Further data, which cannot directly be obtained from experiments (stress, strain, displacement components at any point of specimen or bars, interface force i.e.), were determined.

Material model parameters given in this chapter are further used to investigate the stress wave propagation in multilayered armor systems, which are more complex structures.

4.1. Armor Constituents

In ballistic experiments, the armor plates were composed of a hexagonal 99.5% grade alumina ceramic tile (CoorsTek; AD-995), and a 22 layers of plain weave S2-glass fabric (areal density 0.81 kg/m²), having a [0/90] lay-up orientation (i.e. the fabric warp direction is at 0° and the weft direction is at 90°), backing plate of 10.0 mm thick (Figure 4.1 (a) and (d)). EPDM rubber (Shore A 60), Teflon (Polarchip¹) and Aluminum foam were inserted between ceramic and composite layer. (Figure 4.1 (b) and (c)) The thicknesses of EPDM rubber, Teflon and Aluminum foam were 1.5, 2 and 18 mm in the order given. The commercial explicit finite element code LS-DYNA 971 was used to model these experiments.

In compressed air gun tests, 5x5x1 cm 25 square 99.5% grade alumina ceramic tiles were backed by E-Glass/polyester composite plates of plain weave E-Glass fabric (areal density 0.600 kg/m²), having a [0/90] lay-up orientation (i.e. the fabric warp direction is at 0° and the weft direction is at 90°) as seen in Figure 4.1 (a) and (d). Interlayer materials used in ballistic experiments were inserted.

Mechanical properties, and corresponding material models parameters are described further somewhere in this chapter.

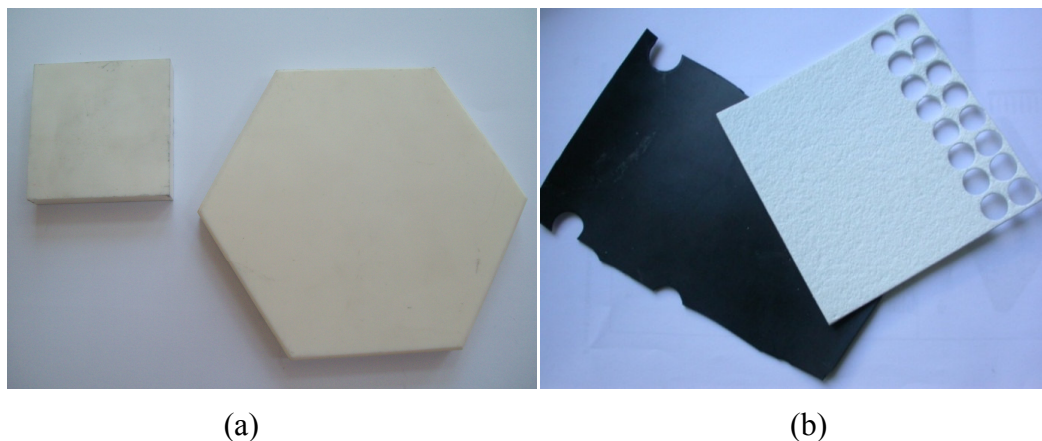


Figure 4.1. Armor constituents: (a) Alumina ceramic, (b) EPDM rubber and Teflon, (c) Aluminum foam and (d) E-Glass and S2-Glass Composite.

¹Polarchip™ is a trademark of W. L. Gore, Inc.

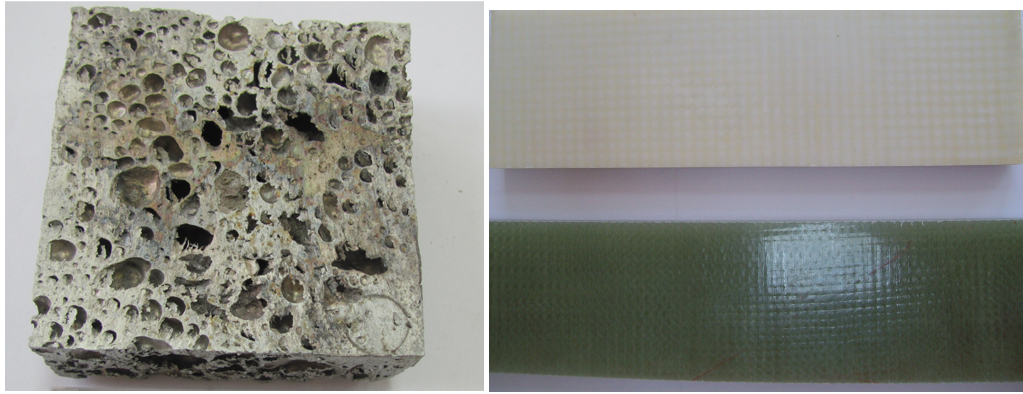


Figure 4.1. (Cont.) (c)

(d)

As seen in Table 4.1, ceramic is a strong material under compressive loading and weak under tension. It is generally heavily fragmented and even sometimes ended up with full damage. The fragmented particles still have plastic material properties and compression strength during ballistic impact. Hence, a material model, JOHNSON_HOLMQUIST (JH-2), including damage evolution and dynamic failure was chosen. JH-2 is specifically developed for brittle materials analogous to JOHNSON_COOK material model for metals. It is developed to simulate the behavior of brittle materials such as ceramic, glass etc. under dynamic loading. It is a pressure and rate sensitive constitutive model which can also successfully simulate the behavior of materials even after damage.

4.1.1. Ceramic Front Layer

Some mechanical properties of AD-995 alumina ceramic are given in Table 4.1

Table 4.1. Mechanical properties of alumina ceramic.
(Source: CoorsTek, 2008).

Material	Modulus of elasticity, E, (GPa)	Compressive and Tensile Strength, S_C, S_T (MPa)	Density, ρ (kg/m^3)	Poisson's Ratio, ν
Ceramic	370	2600, 262	3890	0.22

In the model employed by Johnson and Holmquist, initially conventional elastic regime properties are dominant until yield and plastic strain starts. Within plastic strain, damage initiates. As damage propagates, material weakens and behaves along the weakened curve (Figure 4.2). During the progress of damage, strength drops within the loss of elastic internal energy of deviator and shear stress. This energy is transformed into potential hydrostatic internal energy (Gordon and Tim, 1994; Livermore Software Technology Corporation, 2007).

The equivalent stress (available strength), illustrated by σ^* , is a function of equivalent stresses intact for and damaged regions (σ_i^* and σ_f^*) as seen in the formula below:

$$\sigma^* = \sigma^i - D(\sigma_i^* - \sigma_f^*) \quad (4.1)$$

The equivalent stresses for intact and damaged regions (normalized effective stresses), are given in equations 4.2 and 4.3 respectively. (SFMAX is the maximum fractured strength.)

$$\sigma_i^* = A(P^* + T^*)^N (1 + C \ln \dot{\epsilon}^*) \quad (4.2)$$

$$\sigma_f^* = B(P^*)^M (1 + C \ln \dot{\epsilon}^*) \leq \text{SFMAX} \quad (4.3)$$

Where “P*, T*, and $\dot{\epsilon}^*$ ” refer to normalized pressure, tension strength and strain rate consecutively. They are normalized by the equivalent stress at the Hugoniot Elastic Limit (HEL) as seen in the equations below:

$$T^* = \frac{T}{T_{\text{HEL}}} \quad (4.4)$$

$$P^* = \frac{P}{P_{\text{HEL}}} \quad (4.5)$$

$$\dot{\epsilon}^* = \frac{\dot{\epsilon}}{\dot{\epsilon}_0} \quad (4.6)$$

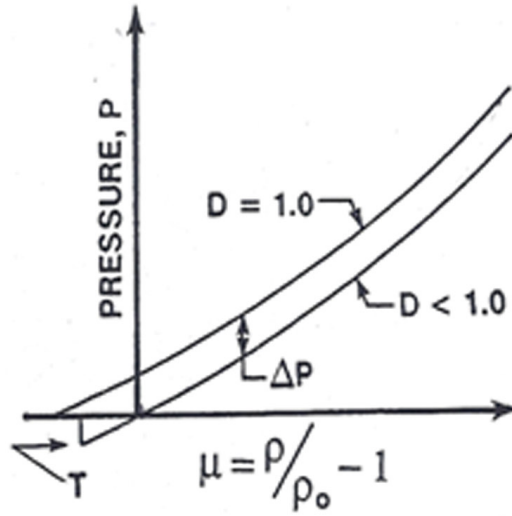


Figure 4.2 Description of JH-2 model in aspects of pressure distribution.
(Source: Johnson and Holmquist, 1998).

HEL is the specific shock pressure level at which material behavior deviates from linear elasticity and D refers to damage parameter varying between 0 and 1. $D=0$ means intact material whereas $D=1$ full damage. Under compression loading, material experiences full damage, only when effective plastic strain reaches the fracture plastic strain. It is expressed by the given equation below:

$$D = \sum \frac{\Delta \epsilon^P}{\epsilon_f^P} \quad (4.7)$$

Where $\Delta \epsilon^P$ is effective plastic strain during cycle of integration and $\Delta \epsilon_f^P$ refers to the fracture plastic strain under a constant pressure that is expressed in equation 4.8. Constants illustrated by D_1 and D_2 are damage constants. Mainly D_1 controls the rate at which damage accumulates. In undamaged material hydrostatic pressure is evaluated as given in equation 4.9 for compression.

$$\epsilon_f^P = D_1 (P^* + T^*)^{D_2} \quad (4.8)$$

$$P = K_1 \mu + K_2 \mu^2 + K_3 \mu^3 \quad (4.9)$$

Material does not experience plastic strain if $P^* = -T^*$. Hence, in tension ($\mu < 0$) it is: Where K_1, K_2, K_3 are constants (K_1 is equal to bulk modulus), and μ is compression variable and equal to:

$$P = K_1\mu \quad (4.10)$$

$$\mu = \frac{\rho}{\rho_0 - 1} \quad (4.11)$$

Where ρ is current density and ρ_0 is initial density. Within the formation of damage, bulking occurs, elastic energy is converted to potential hydrostatic energy and accordingly, pressure increases. This increment is added to hydrostatic pressure equation. Thereby, under compression, hydrostatic pressure equation is converted to equation 4.12. This equation in tension is replaced by:

$$P = K_1\mu + K_2\mu^2 + K_3\mu^3 + \Delta P \quad (4.12)$$

$$P = K_1\mu\Delta P \quad (4.13)$$

JH-2 material model parameters can be determined from the tests conducted at various strain rates. The parameters used in this study were taken from (Krashanitsa and Shkarayev, 2005) and are displayed in Table 4.2.

4.1.2. Interlayer Materials

Previous studies indicate that when a projectile hits the ceramic layer at a relatively high velocity, a compressive stress wave is generated and it propagates from the projectile impact zone in the parallel direction. Once this compressive wave reaches the back face of the ceramic layer, it is partially reflected back as tensile wave, causing the damage in the ceramic layer.

The acoustic impedance mismatch between the ceramic and composite layer plays a key role in the ballistic performance of the armor system. The insertion of an interlayer between these two layers significantly alters the wave propagation characteristics and consequently the ballistic performance of the armor system. Based on this, materials with initially low elastic modulus and acoustic impedance were

selected. In addition to this, two different groups of materials in aspects of Poisson's ratio were chosen to observe effect of surrounding media on interlayer candidates. EPDM rubber has high Poisson's ratio whereas Teflon and Aluminum foam have low Poisson's ratio. Then appropriate material models for interlayers were determined.

Table 4.2. JH-2 material model parameters of alumina ceramic.
(Source: Krashanitsa and Shkarayev, 2005).

Alumina Ceramic Model Parameters		
Symbol	Definition	Value
ρ	Density	3890 kg/m ³
G	Shear modulus	123 GPa
A	Intact normalized strength parameter	0.949
B	Fractured normalized strength parameter	0.1
C	Strength parameter (for strain rate dependence)	0.007
M	Fractured strength parameter (pressure exponent)	0.2
N	Intact strength parameter	0.2
EPSI	Reference strain rate	1.0 s ⁻¹
T	Maximum tensile pressure strength	0.262 GPa
HEL	Hugoniot Elastic limit	8 GPa
D1	Parameter for plastic strain to fracture	0.001
D2	Parameter for plastic strain to fracture (exponent)	1
K1	First Pressure Coefficient (EOS) (bulk modulus)	186.8 GPa

4.1.2.1. EPDM Rubber

EPDM (ethylene propylene diene monomer) rubber is a nonlinear, almost incompressible material with high initial Poisson's ratio (~0.5). While stress wave propagates through the layers of multilayered armor system during ballistic impact, transmission and reflection coefficients do not stay constant at the interfaces of the EPDM and its neighboring layers. Since the magnitude of EPDM rubber's acoustic impedance is very low at the beginning of the deformation, much of stress wave is

reflected back from the ceramic-EPDM rubber interface. This reflected wave encounters the compression wave and reduces the magnitude of stress. As EPDM rubber compresses, acoustic impedance increases, accordingly. The reduction in amplitude of stress wave decreases. Thus, EPDM rubber interlayer loses its effectiveness while it is being compressed.

EPDM rubber was modeled using Ogden Rubber material model. In this material model, EPDM rubber is considered to be fully incompressible since the magnitude of bulk modulus greatly exceeds shear modulus. Rate effects are also taken into account through linear viscoelasticity. In order to model EPDM rubber as an incompressible material, a hydrostatic work term is included in the strain energy function of the relative volume from which stress strain relations can be derived. In Ogden material model, strain energy density function, is expressed in terms of the principal stretches; λ_j as given in the formula below where $j=1, 2, 3$.

$$W(\lambda_1, \lambda_2, \lambda_3) = \sum_{p=1}^N \frac{\mu_p}{\alpha_p} (\lambda_1^{\alpha_p} + \lambda_2^{\alpha_p} + \lambda_3^{\alpha_p} - 3) \quad (4.14)$$

μ and α denote to Ogden material coefficient and exponent respectively. Under the assumption of incompressibility, (only isochoric motions are available and $\lambda_1 \lambda_2 \lambda_3 = 1$), Equation 4.14 can be modified into Equation 4.15 where classical shear modulus is formulated by Equation 4.16:

$$W(\lambda_1, \lambda_2) = \sum_{p=1}^N \frac{\mu_p}{\alpha_p} (\lambda_1^{\alpha_p} + \lambda_2^{\alpha_p} + \lambda_1^{-\alpha_p} + \lambda_2^{-\alpha_p} - 3) \quad (4.15)$$

$$2\mu = \sum_{p=1}^N \mu_p \alpha_p \quad (4.16)$$

Three principal Cauchy stresses (group of stress tensors defining the stress at any point in object) are calculated by the equation below where “p” refers to a Lagrange multiplier introduced by the internal constraint of incompressibility. The modified version of Equation 4.17 is given in Equation 4.18:

$$\sigma_a = p + \lambda_\alpha \frac{\partial W}{\partial \lambda_\alpha} \quad (4.17)$$

$$\sigma_a = \lambda_\alpha P_\alpha \quad (4.18)$$

Where “ P_α ” is hydrostatic pressure and function of Lagrange multiplier (Ogden, 1984; Livermore Software Technology Corporation, 2007). The material model parameters used in the simulations were taken from (Tasdemirci, 2005; Tasdemirci and Hall, 2009) and are given in Table 4.3. The mechanical behavior of EPDM rubber can accurately be reproduced by using Ogden Rubber model with third order (N=3) formulation. Stress-strain data was used as an input and third order fit to the data was used, as seen in Figure 4.3.

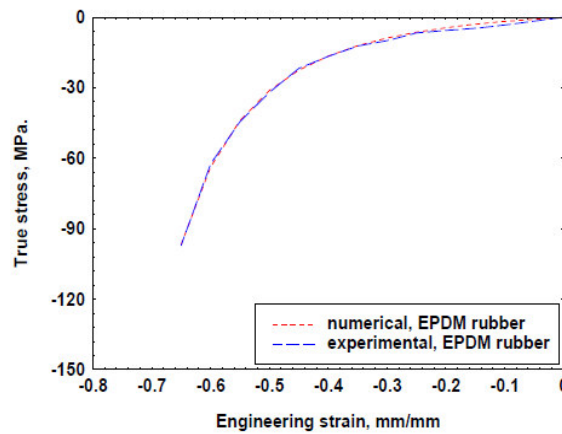


Figure 4.3. Data fit for Ogden material model, N=3.
(Source: Tasdemirci, 2005).

4.1.2.2. Teflon

Teflon (a fluoro polymer composite consisting of expanded polytetrafluoroethylene (ePTFE) matrix filled with boron nitride (BN) particles) is nonlinear, compressible material with low Poisson’s ratio. “CRUSHABLE FOAM” material model developed to model crushable foam with optional damping and tension cutoff was selected for Teflon (Livermore Software Technology Corporation, 2007). Since volumetric strain controls failure, unloading is fully elastic and tension is treated as elastic-perfectly-plastic at the tension cut-off value as demonstrated in Figure 4.4. Mechanical properties and model parameters were determined in (Tasdemirci, 2005; Tasdemirci and Hall, 2009), and they are given in Table 4.3.

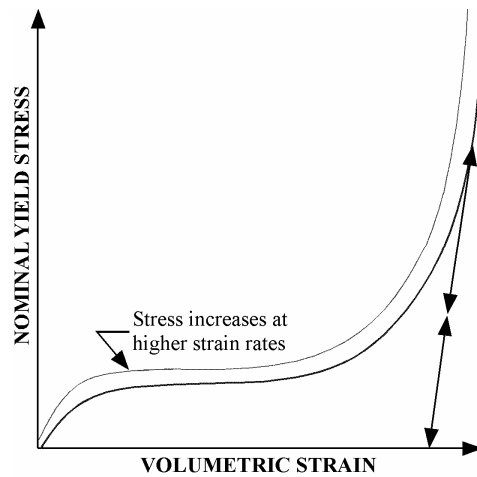


Figure 4.4. Typical yield stress vs. volumetric strain data for crushable foam.
(Source: Livermore Software Technology Corporation, 2007).

Table 4.3. Mechanical properties of EPDM rubber and Teflon.
(Source: Tasdemirci, 2005; Tasdemirci and Hall, 2009).

Material	E (GPa)	ν	Density (kg/m ³)	Other
EPDM Rubber	0.007 (initial)	0.4995	1200	$\mu_1=4.684$ $\mu_2=0.1954$ $\alpha_1= -1.856$ $\alpha_2= -2.992$
Teflon	0.025 (initial)	0.25	760	-

4.1.2.3. Aluminum Metallic Foam

The Aluminum foams were fabricated in DTMLAB in IZTECH by foaming powder compacts (precursors). The major steps of the process are given in Figure 4.5. Aluminum powder (<70 μm) was mixed with TiH_2 powders (<37 μm) and pressed under 200 MPa. Then the pressed powders were hot forged and a precursor was attained. Finally the precursor was foamed in a furnace at 750 $^\circ\text{C}$ and inserted into die.

Aluminum foam have a closed-cell structure and has a plateau stress formation where the stress remains constant through stress value. Plateau stress is the region in stress-strain curve where the stress increases slowly, while the cells deform plastically.

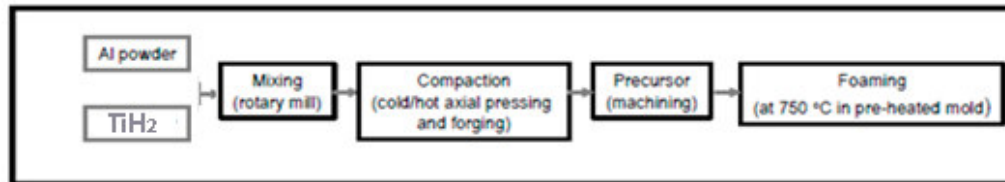


Figure 4.5. The processing stages of the foaming from powder compact process used. (Source: Guden and Yuksel, 2006).

These Aluminum foam plates were modeled with HONEYCOMB material model which is for honeycomb and foam-like materials with anisotropic properties. A nonlinear elastoplastic material behavior can be defined separately for all normal and shear stresses. These are considered to be fully uncoupled (Figure 4.6). Similar to other material models used for EPDM rubber and Teflon, load curves were used as input. Shear and elastic moduli, and stress strain curves for each material direction need to be given. Since the material used in this study can be assumed nearly isotropic, the values of material constants along each direction were identical. Details of mechanical properties and material model parameters can be found in (Ergonenc, 2008; Guden and Yuksel, 2006; Yuksel, 2010) and tabulated in Table 4.4.

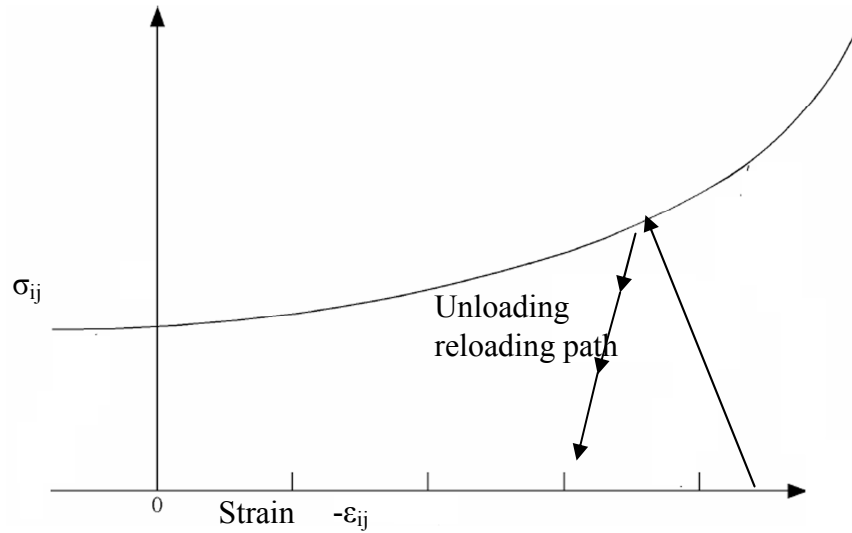


Figure 4.6. Honeycomb material model description.
(Source: Livermore Software Technology Corporation, 2007).

Table 4.4. Mechanical properties of Aluminum Foam.
(Source: Ergönerç, 2008; Yüksel, 2010).

Material	$E_{\text{compacted}}$ (GPa)	v_f	Density (kg/m^3)	Yield Strength σ_Y (MPa)	G_u (MPa)
Aluminum Foam	69	0.285	438	104	69

* $E_{\text{compacted}}$ v_f ; Young Modulus, Relative Volume fraction of compacted Aluminum

* G_u ; Shear Modulus in uncompressed configuration

4.1.3. Composite Backing Plate

MAT162, MAT_COMPOSITE_DAMAGE_MSC, was chosen to model composite layer due to its capability of modeling post-damage softening behavior and also considering strain rate sensitivity of material. This material model is one of the most commonly used material model in progressive failure analysis of composites. It allows the user to monitor the damage initiation and progression such as delamination, matrix and fiber crushing. Also it is possible to define the orientation of each layer of

composite plate as input. This angle varies from 0 to 90 and is represented by a parameter beta (β) in the material model definition. Thus, once the material model parameters have been defined successfully, composite plates of different lay-ups can be accurately modeled. Detailed description of material model and related constants are given in the chapter.

In Ballistic tests, ceramic was supported by S2-Glass/SC-15 composite layers. Mechanical properties were investigated previously and (Tasdemirci, 2005; Tasdemirci and Hall, 2006; Xiao et al., 2007). Material parameters used in this study were taken from (Xiao et al., 2007). However, 0/90 E-Glass/702 CRYSTIC PAX polyester composite used as backing plate in compressed air gun tests were not available in literature. Hence, within the content of current study, characterization of 0/90 E-Glass using SHPB and quasi-static tests and identification of its material model constants were also included. In order to verify the obtained material constants, SHPB simulations were carried out. The results are demonstrated further.

4.1.3.1. Fabrication of E-Glass/polyester Composite

The E-Glass fiber woven fabric (600 gr/m²)/ CRYSTIC 702 PAX composite plates of thickness 14.00 mm, were produced using vacuum assisted resin transfer molding (VARTM) process (Figure 4.7). In this method, the resin is infused to the dry fabric stacked on a single-sided tooling under vacuum.

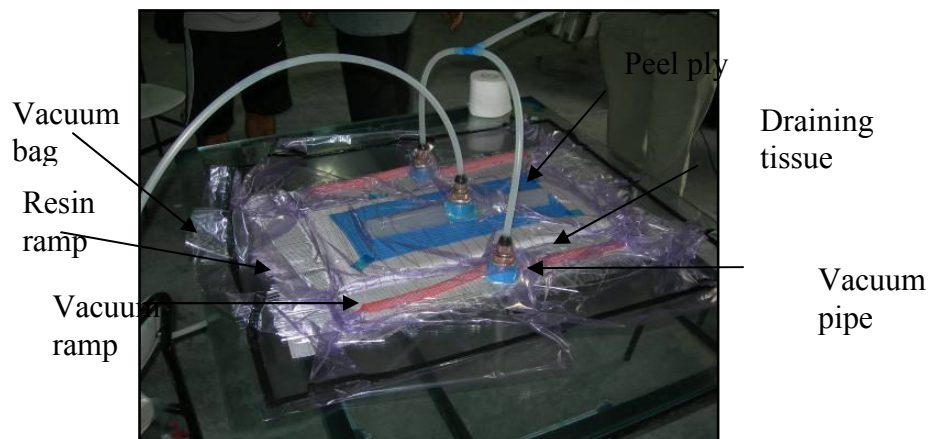


Figure 4.7. VARTM station.

To obtain a fiber volume fraction of 50%, 30 layers of fabric were used. The relation between the volume fraction of the plate and the number of required composite plies is given in the following formula:

$$n = \frac{(t \times \rho_f \times V_f)}{m_f} \quad (4.19)$$

4.1.3.2. Mechanical Characterization of E-Glass/polyester Composite

Compression behavior of composite layer was determined both at high and low strain rates both in the through-thickness and in-plane directions. Specimens were core-drilled (Figure 4.8) in each direction (laterally and longitudinally) providing identical surface quality and dimension. Specimens were 9.5 mm in diameter and 12 mm in length (Figure 4.9).

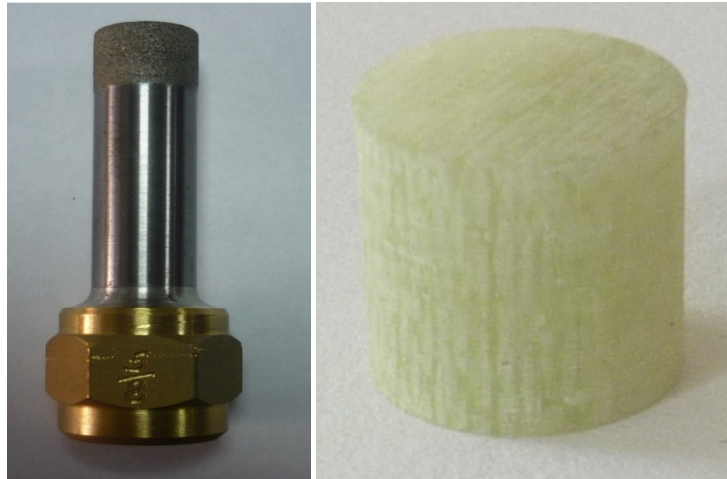


Figure 4.8. Core-drill. Figure 4.9. E-Glass composite specimen.

Samples were quasi-statically and dynamically tested at a strain rate of 0.001 s^{-1} and at an average strain rate of 850 s^{-1} repeatedly. At least three tests were conducted for each strain rate level and testing direction. In Figures 4.10 and 4.11, both quasi-

static and high strain rate test results for in-plane and through thickness directions are given respectively.

The curves are almost linear at the beginning of the deformation then become nonlinear as the strain increases. Elastic modulus calculations were done within the linear region. The peak stresses in the curves are considered failure stresses and the corresponding strains, failure strains.

Strain rate sensitivity of the elastic modulus can be seen in Figure 4.12. Strain rate sensitivity analysis in both directions within the studied strain rate regimes was also done.

The average modulus of the composite increases from 13.0 to 22.0 GPa in the in-plane direction and from 4.8 to 7.1 GPa in the through thickness direction as the strain rate increases from quasi-static ($1.0 \times 10^{-3} \text{ s}^{-1}$) to high strain rates ($> 800 \text{ s}^{-1}$). As can be seen from the Figures 4.10 and 4.11, there is a higher strain rate sensitivity of the elastic modulus in the in-plane direction.

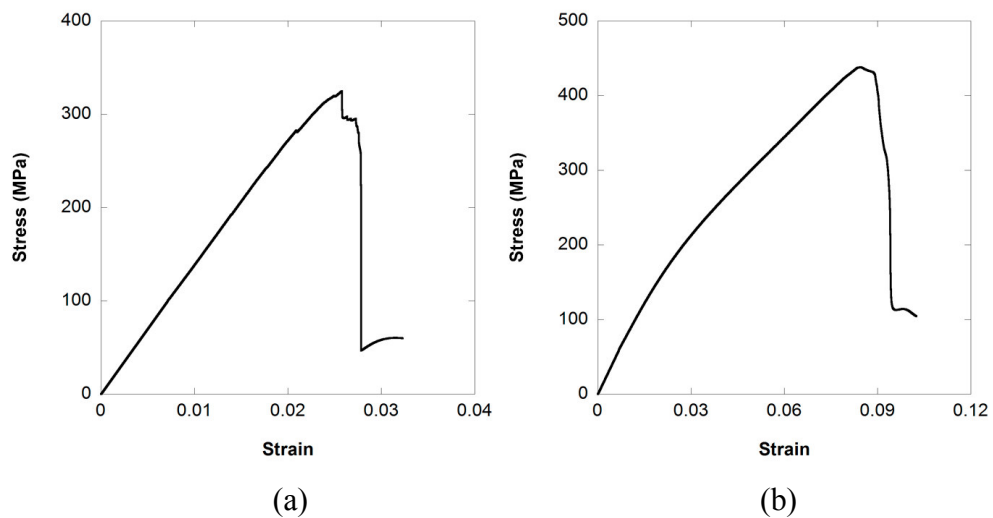


Figure 4.10. Stress-strain curves of 0/90 E-Glass/polyester composites at 0.001 s^{-1} :
(a) in-plane and (b) through-thickness directions.

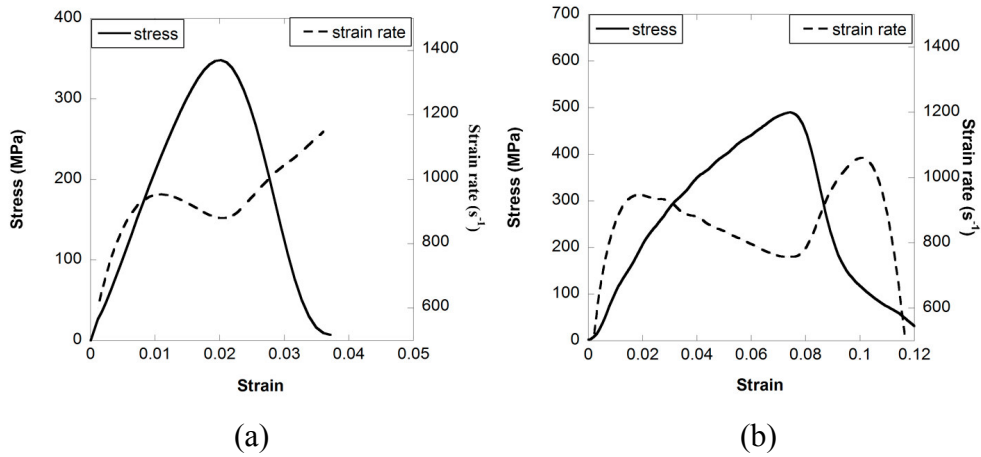


Figure 4.11. Stress-strain curves of 0/90 E-Glass/polyester composites at an average strain rate of 850 s^{-1} : (a) in-plane and (b) through-thickness directions.

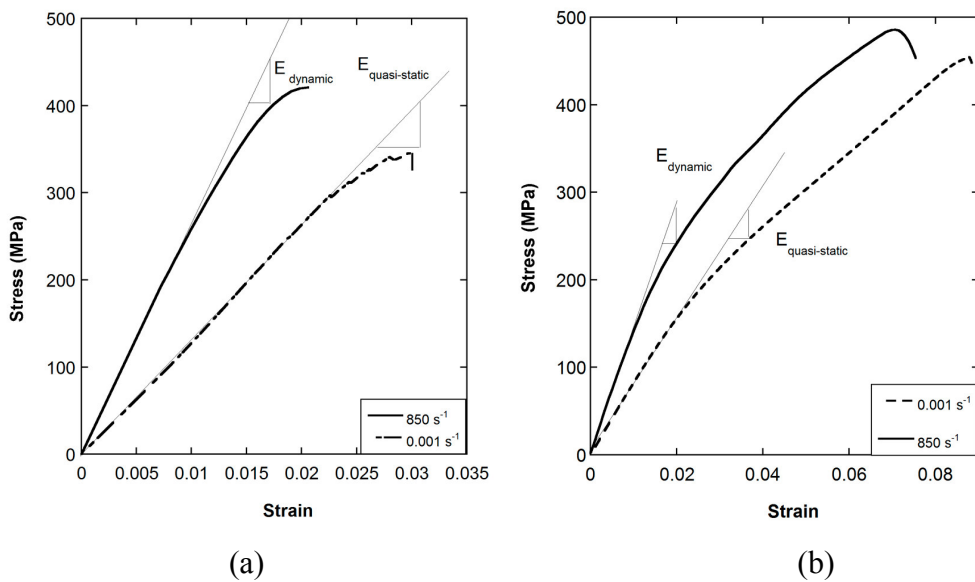


Figure 4.12. Stress-strain curves of 0/90 E-Glass/polyester composites at various strain rates: (a) in-plane and (b) through-thickness directions.

The compressive failure stress of the composite also showed strain rate sensitivity in the strain rate range investigated (Figure 4.12), 330 to 420 MPa in the in-plane and 430 to 490 MPa in the through thickness directions, exhibiting a higher strain rate sensitivity of the failure stress in the in-plane direction.

The average failure strains show strain rate dependence as well: in the in-plane direction, failure strain decreases as strain rate increases from 0.025 at 10^{-3} s^{-1} to 0.020

at 850 s^{-1} . In addition, average failure strain in the through-thickness direction decreases slightly with strain rate from quasi-static to high strain rates: 0.085 at 10^{-3} s^{-1} to 0.073 at 850 s^{-1} . Figures 4.13 and 4.14 show failed samples tested at quasi-static and high strain rates in the in-plane and through-thickness directions.

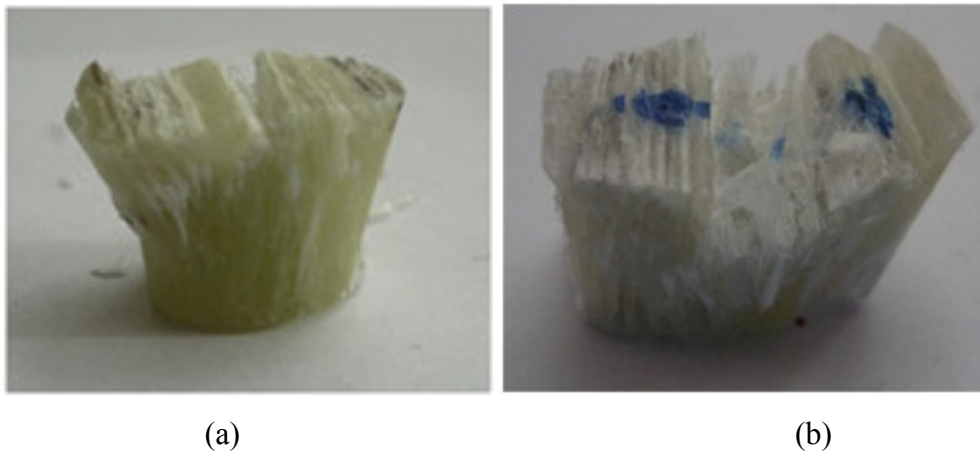


Figure 4.13. Photographs of samples tested in the in-plane direction: (a) quasi-static and (b) high strain rate.



Figure 4.14. Photographs of samples tested in the through-thickness direction: (a) quasi-static and (b) high strain rate.

Stress and strain levels observed in the in-plane direction are lower than those of the through-thickness direction, due to different operative failure modes. For the specimen along the in-plane direction, under both quasi-static and high strain rate loading, predominant failure mode is the delamination between fibers and resin, indicating low interfacial strength between them. At higher strain rates, in particular, specimens split along the loading direction, which is aligned with the fiber direction. In through-thickness direction, at high strain rates, extensive cracking occurs at interlaminar boundaries, resulting in adjoining layers being displaced and extruded in different directions and giving rise to two major fragments and several smaller ones. Cracks are initiated between the fiber layers (Figure 4.15) and also progressive shear cracks are observed in the matrix.

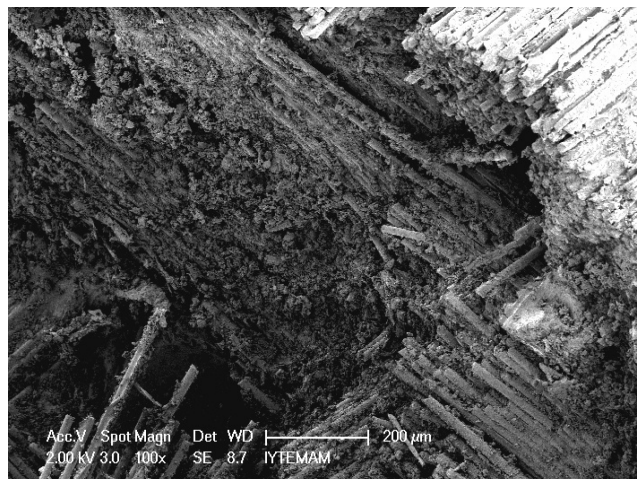


Figure 4.15. SEM image of specimen tested in the through-thickness direction.

After having determined mechanical behavior of composite layer, MAT162 related parameters were obtained from the experimental results. This material model necessitates nine elastic constants (E_A , E_B , E_C , ν_{BA} , ν_{CA} , ν_{CB} , G_{AB} , G_{BC} , G_{CA}) and ten strength-related parameters (S_{AT} , S_{AC} , S_{BT} , S_{BC} , S_{CT} , S_{FS} , S_{FC} , S_{AB} , S_{BC} , S_{CA}) to define the yield after elastic deformation. Several failure criteria can be defined for different damage modes, e.g., tensile and compressive fiber failure, fiber crushing, through thickness matrix failure and delamination. Experimental data played a significant role to

determine most of these parameters. Some were taken from the literature and explicitly mentioned in the related tables.

MAT162 exhibits post-damage softening behavior of composites using continuum damage mechanics principles while degrading the material properties. It is based on the principle of progressive failure of Hashin (Hashin, 1980) and damage mechanics of Matzenmiller et al. (Matzenmiller et al., 1995) that incorporates features for controlling strain softening after failure. Damage propagation is characterized by elastic moduli reduction which is expressed in terms of damage parameters ω_i :

$$E_i = (1 - \omega_i)E_i^0 \quad (4.20)$$

$$\omega_i = 1 - \exp\left(\frac{-r_i^{m_i}}{m_i}\right) \quad 1 \leq r_i, \quad i = 1, 2, \dots, 6 \quad (4.21)$$

where E_i^0 and E_i are the initial and reduced elastic moduli consecutively, r_i are the damage thresholds associated with six different damage functions related with fiber damage, matrix damage and delamination, and m_i are material damage parameters independent of strain-rate.

The softening parameter "AM" is defined for four different damage modes in model, e.g., AM1 for fiber damage in the material direction A, AM2 for fiber damage in material direction B, AM3 for fiber crushing, and AM4 for matrix crack and delamination.

MAT162 also accounts for different strain rate sensitivities in tension, compression and shear which can be used for simulation in high strain rate deformation events, the non-linear stress-strain response of a composite layer is occurred. It is calculated by semi-logarithmic functions for elastic moduli. The effect of strain rate on the ply strength expressed as :

$$\{S_{rt}\} = \{S_0\} \left(1 + C_1 \ln \frac{\dot{\epsilon}}{\epsilon_0}\right) \quad (4.22)$$

where C_1 , is the strain rate constant for strength properties, $\{S_{rt}\}$ are the rate dependent strength values, $\{S_0\}$ are the quasi-static reference strength values, ϵ_0 is the

quasi-static reference strain rate, and $\dot{\epsilon}$ are the associated strain rates (Livermore Software Technology Corporation, 2007). For the rate dependent stiffness properties:

$$\{E_{rt}\} = \{E_0\} \left(1 + C_i \ln \frac{\dot{\epsilon}}{\dot{\epsilon}_0} \right) \quad i = 2, \dots, 6 \quad (4.23)$$

where $\{E_{rt}\}$ are the rate dependent stiffness values, $\{E_0\}$ are the quasi-static stiffness values, C_2 , C_3 and C_4 are the strain rate constants for the longitudinal, shear and transverse modules, $\dot{\epsilon}_0$ is the reference strain rate (0.001 s^{-1}), and $\dot{\epsilon}$ are the associated strain rates (850 s^{-1}).

To determine C_1 , failure stress values at different strain rates in the in-plane and through-thickness directions were calculated and represented in Figure 4.17. Based on the experimental data given below, C_1 is 0.0014. Moreover, C_2 and C_4 , that are the parameters dependent on longitudinal and transverse elastic modules, were calculated 0.038 and 0.03 as shown in Figure 4.16 (Tunusoglu et al., 2010). However, C_3 is dependent on shear moduli and it was taken from (Naik and Kavala, 2008) as 0.003.

The methodology followed in MAT162 material model parameter validation/determination consists of two phases: a) single element (Figure 4.18) and b) SHPB test simulations (Figure 4.19). There is no clearly defined procedure for calibrating damage growth and post-failure softening. Thus, parametric simulations were conducted for different loading and boundary conditions, e.g., in-plane compression and transverse compression. Firstly, a single-element model loaded in compression in the in-plane direction was used to observe the effect of different values of AM1 and AM2. The models were validated with experiments further.

Value of 2 for both AM1 and AM2 gave the best representation of the post-failure behavior. From the through-thickness compression model, damage parameter, AM3, was set to 0.5 to represent the abrupt fiber failure observed in the experiments. However, selection of the value for the shear damage parameter is not that straightforward. It is not possible to define delamination damage criteria AM4 with a “single element” model. Hence, for a 0.35 value of AM4, reported in (Xiao et al., 2007) was used in this study.

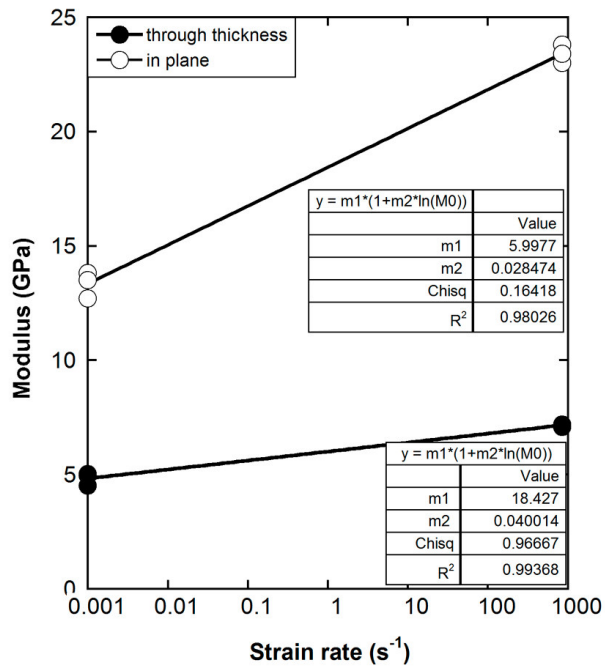


Figure 4.16. Elastic modulus vs. strain rate.

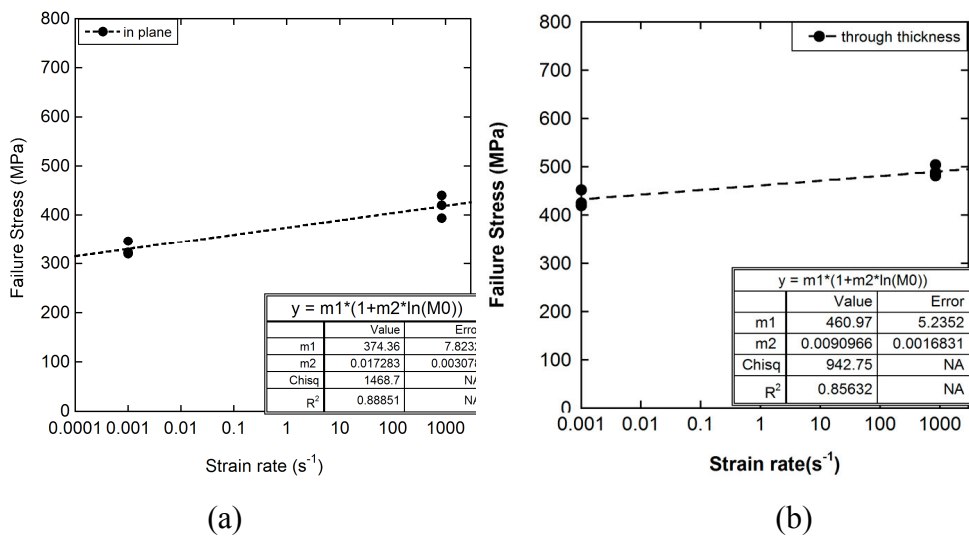


Figure 4.17. Stress vs. strain rate in: (a) in-plane and (b) through-thickness directions.

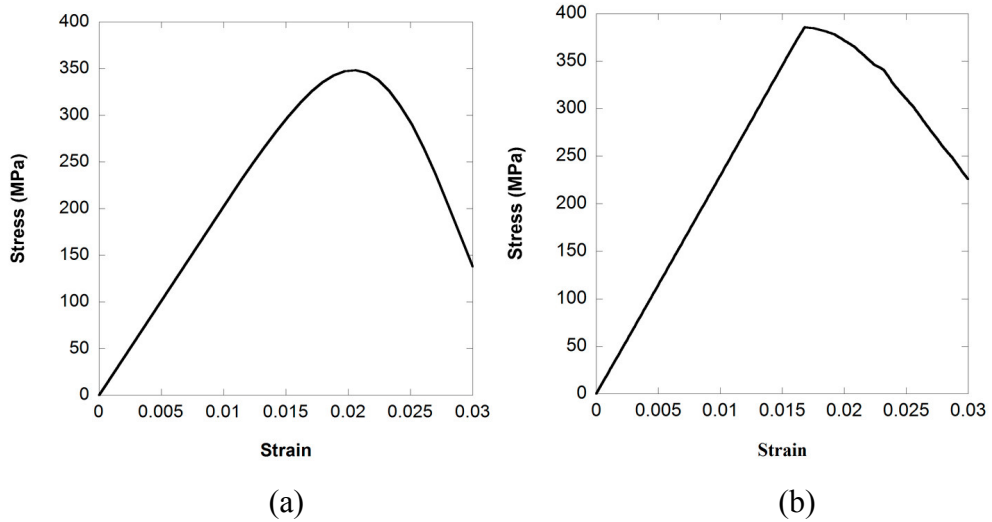


Figure 4.18. Stress vs. strain curves of 0/90 E-Glass composite at 850 s^{-1} strain rate in the in-plane direction: (a) experimental, and (b) numerical (single element model).

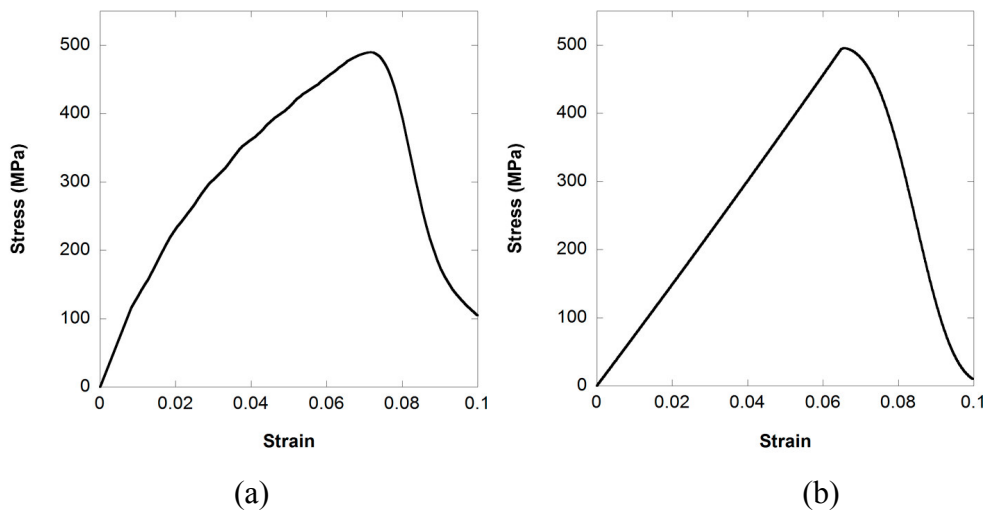


Figure 4.19. Stress vs. strain curves of 0/90 E-Glass composite at 850 s^{-1} strain rate in the through-thickness direction: (a) experimental, and (b) numerical (single element model).

There are some material constants that have to be fine tuned by comparing the results of SHPB simulations with those of experiments, while keeping the known properties constant throughout the calibration. The parameters that need to be calibrated are out-of-plane fiber and matrix shear strengths and the delamination constant. In a

recent experimental study conducted on plain-weave E-glass/epoxy composite by (Naik et al., 2007), interlaminar shear strength was measured to be 29.4 MPa at an average strain rate of 1000 s^{-1} . In the same study, strain-rate sensitivity of interlaminar shear strength was also discussed. In this study, 30 Mpa was used as the baseline value of interlaminar shear strength. Shear moduli and Poisson's ratio values in the in-plane and through-thickness directions were taken from (Deka et al., 2008). The through-thickness tensile strength of the composite was estimated to be 50 Mpa. Experimental results revealed that the through-thickness tensile strength of the different mposite is usually lower than the tensile strength of the polyester matrix material.

The interlaminar shear stress concentration was studied by (Pahr et al., 2002) and the stress concentration was reported 1.21. In this study, a value of 1.2 was used for the delamination constant. Besides, the above mentioned material properties and parameters, three eroding parameters need to be determined. The three eroding parameters, E_LIMIT, E_CRSH, and EEXPN, were obtained from fine tuning the results till matching up them to the bar responses and final deformed shapes of the specimens for both in-plane and through-thickness tests. Material model parameters for 0/90 E-Glass/polyester and S2-Glass/epoxy are exhibited in Table 4.5 and 4.6 respectively.

4.1.3.3. Verification of Material Model Parameters of E-Glass/polyester Composite

For this purpose, SHPB numerical model of 0/90 E-Glass/polyester was created for both in-plane and through-thickness directions. The experimental and numerical bar responses and damage behavior of composite were compared to verify the model constants. Once validated, these material model constants can be further used in compressed air gun test simulations of multilayered armor systems.

Table 4.5. Material model constants of 0/90 E-Glass/polyester composite.

E-Glass Model Parameters	Value
Density, ρ,	1850 (kg/m ³)
Tensile modulus, E_A, E_B, E_C	18.2, 18.2, 6.2 (GPa)
Poisson's ratio, $\nu_{BA}, \nu_{CA}, \nu_{CB}$	0.08, 0.14, 0.15
Shear modulus, G_{AB}, G_{BC}, G_{CA}	1.79, 1.52, 1.52 (GPa)
In-plane tensile strength, S_{AT}, S_{BT}	0.4 (GPa)
Out of plane tensile strength, S_{CT}	0.05 (GPa)
Compressive strength, S_{AC}, S_{BC}	0.33 (GPa)
Fiber crush, S_{FC}	0.5 (GPa)
Fiber shear, S_{FS}	0.2 (GPa)
Matrix mode shear strength, S_{AB}, S_{BC}, S_{CA}	0.03 (GPa)
Residual compressive scale factor, SFFC	0.3 (GPa)
Friction angle, PHIC	10 (GPa)
Damage parameter, AM1, AM2, AM3, AM4	2.0, 2.0, 0.5, 0.35
Strain rate parameter, C_1, C_2, C_3, C_4	0.014, 0.040, 0.03, 0.0284
Delamination, S_{DELM}	1.2

Table 4.6. Material model constants of 0/90 S2-Glass/epoxy composite.
(Source: Xiao et al., 2007).

S-2 Glass Model Parameters	Value
Density, ρ,	1850 (kg/m ³)
Elastic modulus, E_A, E_B, E_C	27.5, 27.5, 11.8 (GPa)
Poisson's ratio, $\nu_{BA}, \nu_{CA}, \nu_{CB}$	0.11, 0.18, 0.18
Shear modulus, G_{AB}, G_{BC}, G_{CA}	2.9, 2.14, 2.14 (GPa)
In-plane tensile strength, S_{AT}, S_{BT}	0.604 (GPa)
Out of plane tensile strength, S_{CT}	0.058 (GPa)
Fiber crush, S_{FC}	0.85 (GPa)
Fiber shear, S_{FS}	0.3 (GPa)
Matrix mode shear strength, S_{AB}, S_{BC}, S_{CA}	0.075, 0.058 0.058 (GPa)
Residual compressive scale factor, SFFC	0.3 (GPa)
Friction angle, PHIC	10 (GPa)
Damage parameter, AM1, AM2, AM3	2.0, 2.0, 0.5
Delamination, S_DELM	1.2
Eroding strain, E_LIMIT	0.2

In the damage analysis of a composite specimen, a full (no symmetry definitions) numerical model was used with appropriate boundary conditions. The model has three components in contact: the incident and transmitter bars each 1524 mm in length, and the specimen. Experimentally measured stress pulse was used as an input to the impact face of the incident bar and all other boundaries are traction-free. The finite element mesh of SHPB is shown in Figure 4.20. In order to reduce computational time, mesh biasing was done. To decrease computation time further, 1524 mm length of the bars instead of full length was simulated. Although this decreases the transit time

between successive waves and shortens the wave duration slightly, it does not affect the basic wave shapes or amplitudes. Trial computations were carried out using full-length bars but, apart from the slightly smaller time window, no significant differences were found and the shorter bars were used in all calculations henceforth. Incident and transmitter bar models are composed of 60000 elements. Through-thickness and in-plane composite specimens were modeled with 83520 and 72000 elements, respectively. Eroding single surface contact was defined between the bar ends and the specimen. Bars, of which mechanical properties were given in Table 3.2, were modeled by PLASTIC_KINEMATIC material model. Since this model is suitable for steel and the details about model will be explained further.

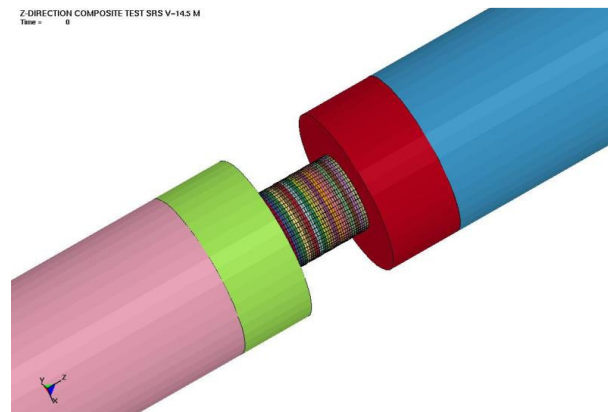


Figure 4.20. SHPB numerical model.

Figure 4.21 (a) and (b) show experimental and numerical results for an SHPB experiment conducted with a striker bar velocity of 14.5 m/s corresponding an average strain rate 850 s^{-1} .

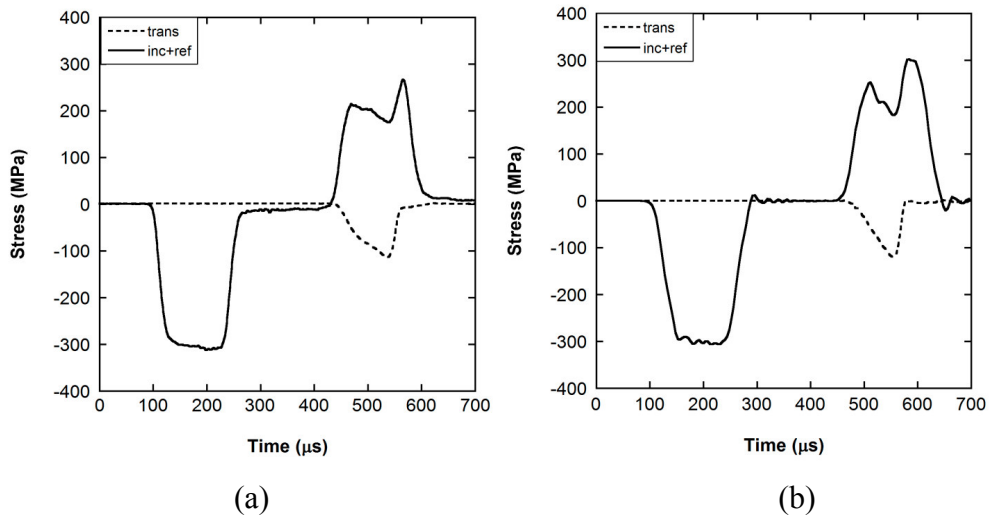


Figure 4.21. Bar responses of SHPB experiments in the in-plane direction: (a) experimental and (b) numerical.

The amplitude of the reflected wave increases as a function of time from zero to a local maximum before decreasing gradually: this is followed by a sharp rise indicating that the specimen has been extensively damaged or has failed. The numerical data of Figure 4.21 (b) are very similar to those of experimental data and, hence, confirm the validity of the model.

Figures 4.22 (a) and (b) show experimental and numerical SHPB waves of the in-plane specimen. The reflected wave increases from zero to a local maximum then decreases slightly, indicating specimen failure during the test.

Figure 4.23 (a) and (b) show numerically deformed specimens in the through thickness and in-plane directions, respectively. For the specimen deformed in the through-thickness direction, simulation shows the form of severe delamination, matching excellently with the experimentally observed damage modes (Figure 4.23 (b)). The longitudinal compressive strain generated lateral strains which promoted the development of interlaminar matrix cracks. Fiber bundles flowed outward from the specimen and eventually the specimen disintegrated catastrophically. The in-plane specimen failed by axial splitting in two or more pieces along the loading direction. The numerical model was accurately reproduced, therefore, the final appearance of fractured sample.

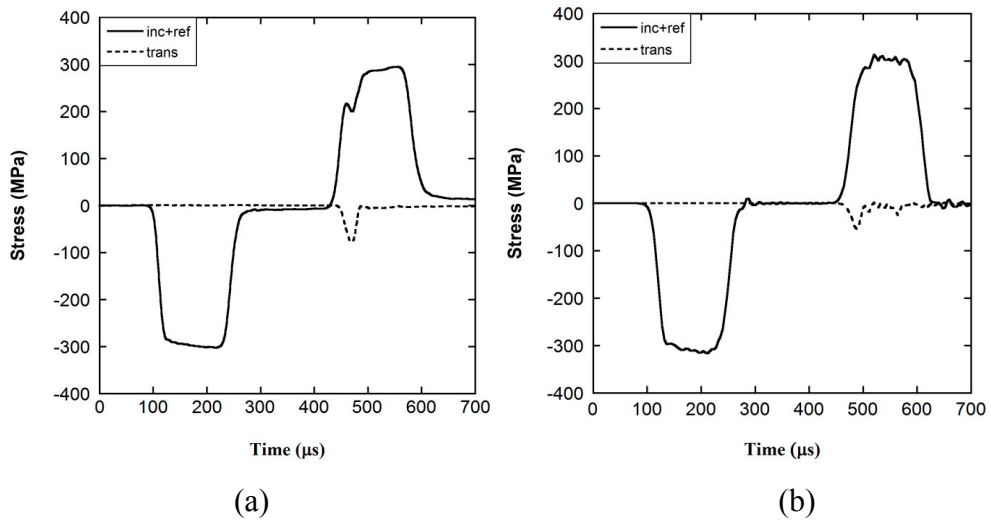


Figure 4.22. Bar response of SHPB experiments in the through-thickness direction (a) experimental and (b) numerical.

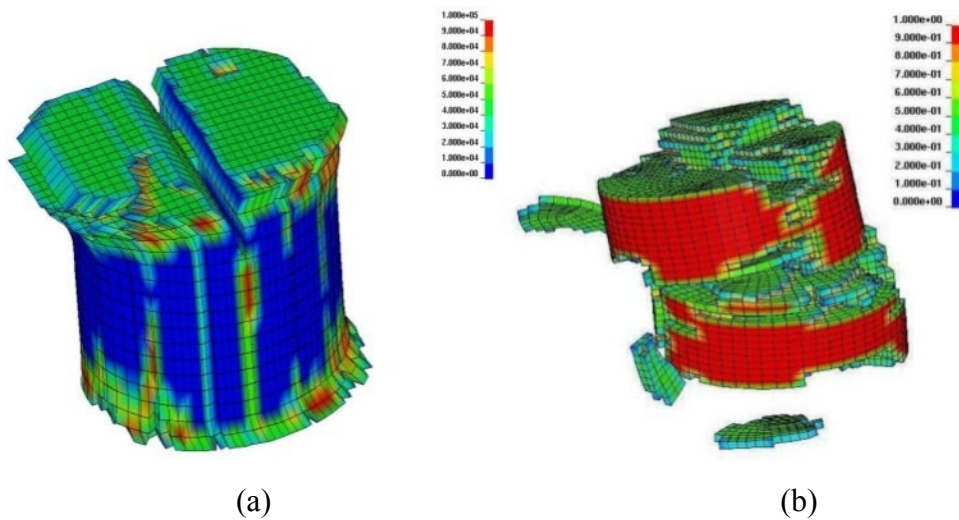


Figure 4.23. Delamination damage: (a) in-plane and (b) through-thickness.

4.1.4. Polyester Cover Layer

The targets of ballistic tests were embedded in a polyester resin and molded in a rectangular glass frame. This outer polyester layer was placed for two reasons; to keep the fractured pieces together and make the post-mortem analysis possible and to support the layer with the armor holder during ballistic impact. The epoxy is modeled with `PIECEWISE_LINEAR_PLASTICITY` material model. With the material model one

can define an elasto-plastic material with an arbitrary stress-strain curve and arbitrary strain dependency (Livermore Software Technology Corporation, 2007).

Hence, stress-strain curve is entered to the model as input, “LCSS”. Optional fully viscoplastic formulation which incorporates the different options above within yield surface was selected throughout the solution. Density, Young’s Modulus, Poisson’s ratio and yield stress are the required material model constants. If yield stress entered is bigger than zero, dynamic yield stress is computed from the sum of the static stress $(\sigma_y^s)(\varepsilon_{eff}^p)$ typically given by the stress curve and initial yield stress referred by SIGY multiplied by the Cowper-Symonds factor as demonstrated in the following equation:

$$\sigma_y(\varepsilon_{eff}^p, \dot{\varepsilon}_{eff}^p) = (\sigma_y^s)(\varepsilon_{eff}^p) + SIGY \cdot \left(\frac{\dot{\varepsilon}_{eff}^p}{C}\right)^{1/p} \quad (4.24)$$

Where “ ε_{eff}^p ” and “ $\dot{\varepsilon}_{eff}^p$ ” are effective plastic strain and strain rate, “C” and “p” refers to strain rate parameters that can be entered directly to model or LS-DYNA can calculate them from stress-strain curve. In this study it was calculated by LS-DYNA from entered curve. Erosion is controlled with failure criteria. When the calculated plastic strain in each element reaches a critical value, defined by user, element is deleted from the calculation. Mechanical properties and related constants of the material model are given in Table 4.6.

Table 4.7. Mechanical properties of polyester.

Polyester Model Parameters	Value
Density, ρ	1133 (kg/m ³)
Elastic modulus, E	3.2 (GPa)
Poisson’s ratio, ν	0.35
Yield Stress, SIGY	113 (MPa)

4.1.5. Projectile

7.62 mm NATO A.P. steel projectile was modeled using PLASTIC_KINEMATIC material model. It is bi-linear plastic-kinematic model including formulations combining isotropic and kinematic hardening (Figure 4.24). Moreover, it is cost effective and incorporates deformation. In the model, isotropic hardening was selected (Livermore Software Technology Corporation, 2007). Material model parameters of projectile were taken from Fawaz et al. (Fawaz et al., 2004) and are demonstrated in Table 4.7.

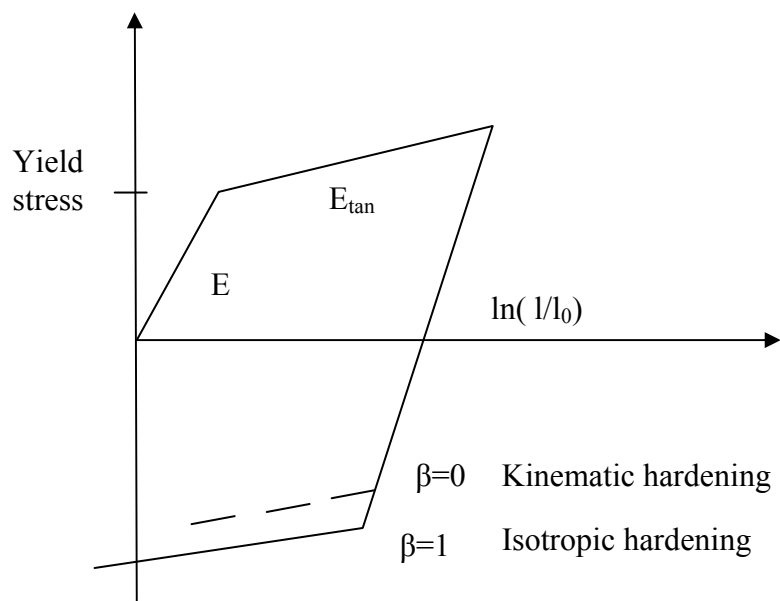


Figure 4.24. Elastic-plastic behavior with isotropic and kinematic hardening.

Table 4.8. Material model parameters of projectile.
(Source: Fawaz et al., 2004).

Projectile Model Parameters	Value
Density, ρ	7890 (kg/m ³)
Elastic modulus, E	202 (GPa)
Poisson's ratio, ν	0.30
Yield Stress, SIGY	1069 (MPa)
E_{tan}	2.0 (GPa)

CHAPTER 5

INVESTIGATION ON THE BALLISTIC PERFORMANCE OF ARMOR CONFIGURATIONS

As explained before, multilayered armor system consist distinctively different materials, having vastly different acoustic impedances and nonlinear behavior, thus the stress wave propagation is a complex task. In these systems stress wave propagates along different directions. To investigate this propagation, ballistic experiments and simulations have to be coupled. For this reason, the effect of the interlayer material on the ballistic performance was investigated both experimentally and numerically.

Ballistic tests were performed on without, with EPDM rubber, Teflon and Aluminum metallic foam configurations. While the targets were impacted using a 7.62 mm NATO armor-piercing projectile, their finite element models were developed. The fracture pattern of the ceramic layer and the damage generated in the composite plate were investigated. Energy distribution in composite layer, stress distribution in ceramic and composite layers, interface forces were discussed.

It was confirmed that the ceramic layer was efficiently fragmented during the ballistic impact of Aluminum foam and Teflon interlayer configuration. In order to determine the most efficient interlayer and optimum thickness value in aspects of weight performance ratio in armor design, Teflon and Aluminum foam interlayer configurations having two different areal densities were simulated. The results indicate that Aluminum foam delivers better performance and also up to a certain limit, increase in thickness raises the performance.

5.1. Specimen Preparation and Experimental Study

Ballistic tests were performed on the targets composed of alumina ceramic tiles bonded to a composite plate (having dimensions of 120x160x12 mm³) with (EPDM rubber, Teflon, al foam) and without an interlayer (Figure 5.1 (a) and (b)). The targets were mounted into a polyester resin in a rectangular glass mold. The polyester cover gathered the constituents of armors and provided to fix whole target.

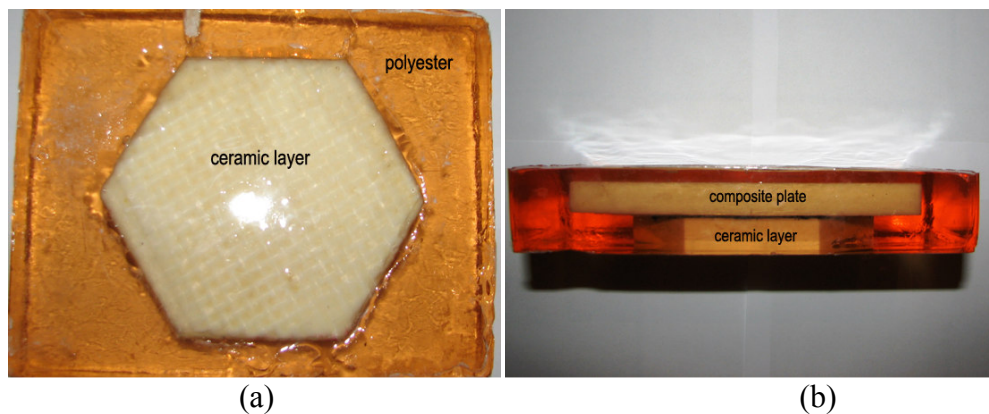


Figure 5.1. Mounted ceramic/composite armor target: (a) top and (b) side view.

The targets were then mounted on the steel plates of 2 cm. The steel plates were then inserted into the ballistic fixture for the testing. The targets were hit using a 7.62 x 51 mm NATO armor-piercing (A.P.) round projectile with a hard steel core at a velocity of 800 ± 50 m/s. Four different configurations were tested; without an interlayer and with an interlayer of EPDM rubber, Teflon (Polarchip²) and Aluminum metallic foam.

5.2. Finite Element Model Description

As the multilayered armor systems are becoming increasingly complex, the analysis of the wave propagation between the layers requires both modeling and experimental investigations.

²Polarchip™ is a trademark of W. L. Gore, Inc.

Finite element models were developed to investigate the effect of interlayer material on the ballistic response of the multilayered armor. In the modeling, the projectile geometry was simplified in a 60° conical-cylindrical shape, 7.62 mm in diameter and 28.1 mm in length of which performance is similar to the 7.62 mm NATO armor-piercing (AP) round projectile (Fawaz et al., 2004). The armor plates were composed of an alumina ceramic front layer of 14.0 mm thick (CoorsTek, 995) hexagonal tile, and a 10.0 mm thick 5x5 plain weave S-2 glass fiber woven fabric (0.814 kg/m²) composite backing plate adhesively bonded with SC 15 (Applied Poleramic Inc.) epoxy. Interlayer EPDM rubber, Teflon and Aluminum foam were inserted between ceramic and composite layer. The thicknesses of EPDM rubber, Teflon and Aluminum foam were sequentially 1.5, 2 and 18 mm. In the damage analyses of the multilayered armor system, a full (no symmetry definitions) numerical model shown in Figure 5.2 (a) was used.

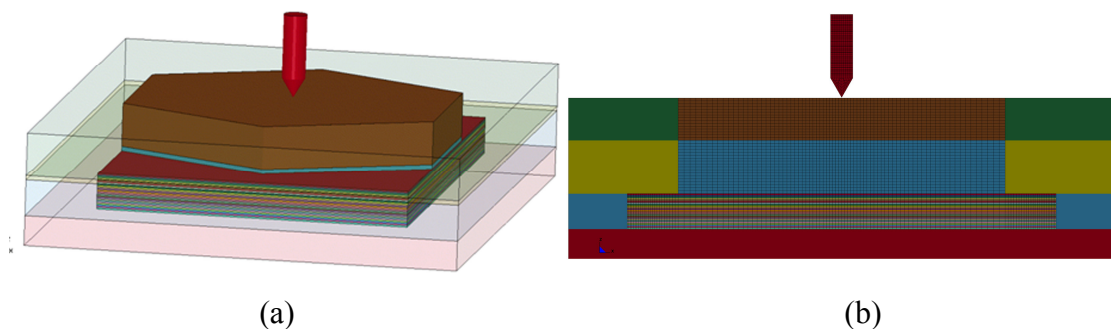


Figure 5.2. Ballistic test numerical model (a) top (b) cross-sectional views.

Armor panel components and projectile were modeled with eight node solid elements. Element size is a highly critical variable for this type of problems. The mesh sensitivity of the model was performed by varying the number of elements of the penetrator and the layers. Simulations were conducted for several different mesh densities; of armor at an element size of 0.65 x 1 x 0.953 mm³, the solution seems to converge. The effect of mesh size on the penetration resistance force was also studied for different meshes while decreasing the element size from 1.30 x 2 x 1.79 to 0.325 x 0.5 x 0.477 mm³ (Figure 5.3).

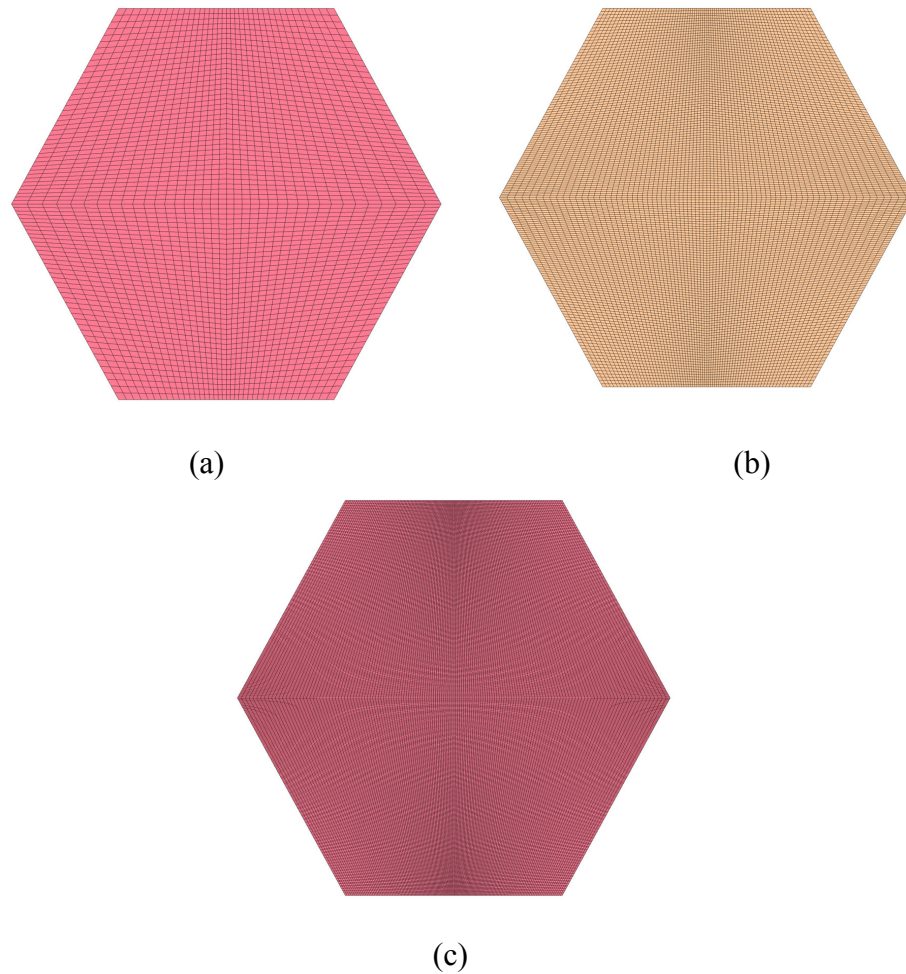


Figure 5.3. Different size meshes of ceramic layer: (a) coarse, (b) medium and (c) fine.

Even though the number of elements was increased by a factor of 2 (and the computational time by a factor of at least 1.15 and at most 3.9), the trend of variation in time domain is similar as seen in the Figure 5.4. The difference of the peak value of penetration resistance force between fine and medium mesh analysis was only 14.8% whereas 38.5% between coarse and fine mesh analysis.

Based on this, and on the restriction that the computational time should be limited, an element size typically between 0.65 and 1 mm was used in the various parts in the present study. This element size resulted in about 1725336 elements in the models and a computational time of about three hours when running on eight Intel Xeon 2.83 GHz processors. The total number of elements and maximum, minimum element size of each part are given in Table 5.1. Finite element grid of half section of model was displayed in Figure 5.2 (b).

Table 5.1. Details of the mesh used through the study.

Part	Thickness (mm)	Number of elements		Element size in plane	
		Total	Through- thickness	Maximum (mm)	Minimum (mm)
Ceramic	14.3	177840	15	2.024	0.65
Composite	12	464256	24	2.024	0.65
EPDM rubber	1.5	23712	2	2.024	0.65
Teflon	2	23712	2	2.024	0.65
Aluminum foam	18	213407	18	2.024	0.65
Polyester Mold	10	571536	4	2.024	0.65
Projectile	28.1	3672	30	0.63	0.63

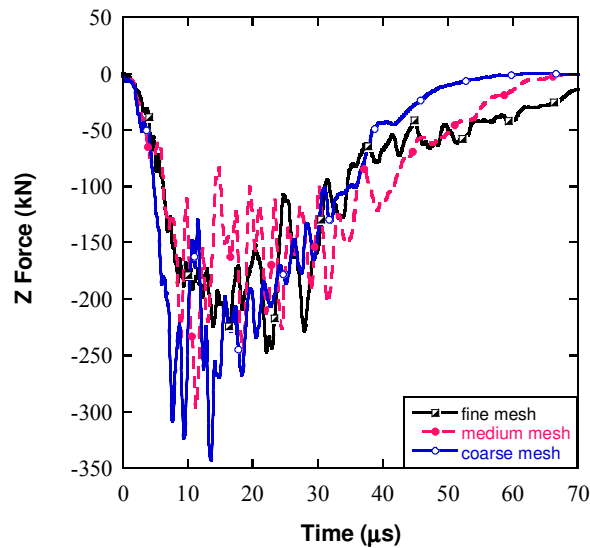


Figure 5.4. Force vs. time data of ceramic layers for different mesh sizes.

Two different contact definitions were used in the model. The composite layer was modeled with the eroding single surface contact definition, enabling to a single segment in contact. All other interfaces were modeled with eroding surface to surface

contact definition. Segment based contact algorithm, suitable for high velocity impact problems, was used in all simulations. The termination time for the simulations is 250 μ s. It is noted that the termination time is long enough to allow the projectile come to a full stop and also short enough to prevent superfluous solution times.

5.3. Experimental and Numerical Results

Excellent agreement between the numerical and experimental results was observed. Similar to tested tiles, approximately symmetric three dimensional growth of damage is displayed in both experimental and numerical results (Figure 5.5). Moreover, post-mortem study revealed that, the damage enveloped in ceramic consists surface crater, fracture conoid, radial and circumferential cracks.

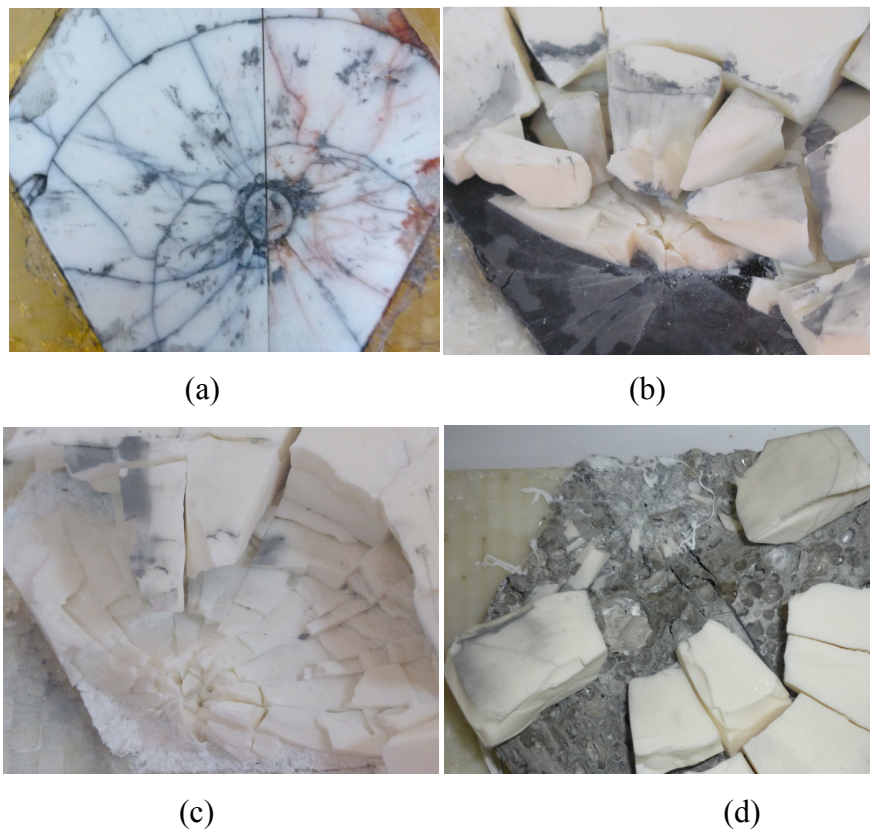


Figure 5.5. Ballistic test specimens: (a) without, (b) with EPDM rubber, (c) Teflon and (d) Aluminum foam interlayers.

Damage evolution in numerical model matches experimental results as seen in Figure 5.6 (a), (b) and (c). In these figures, damage evolution on ceramic layer of without, with EPDM rubber and Teflon interlayer configurations are displayed consecutively.

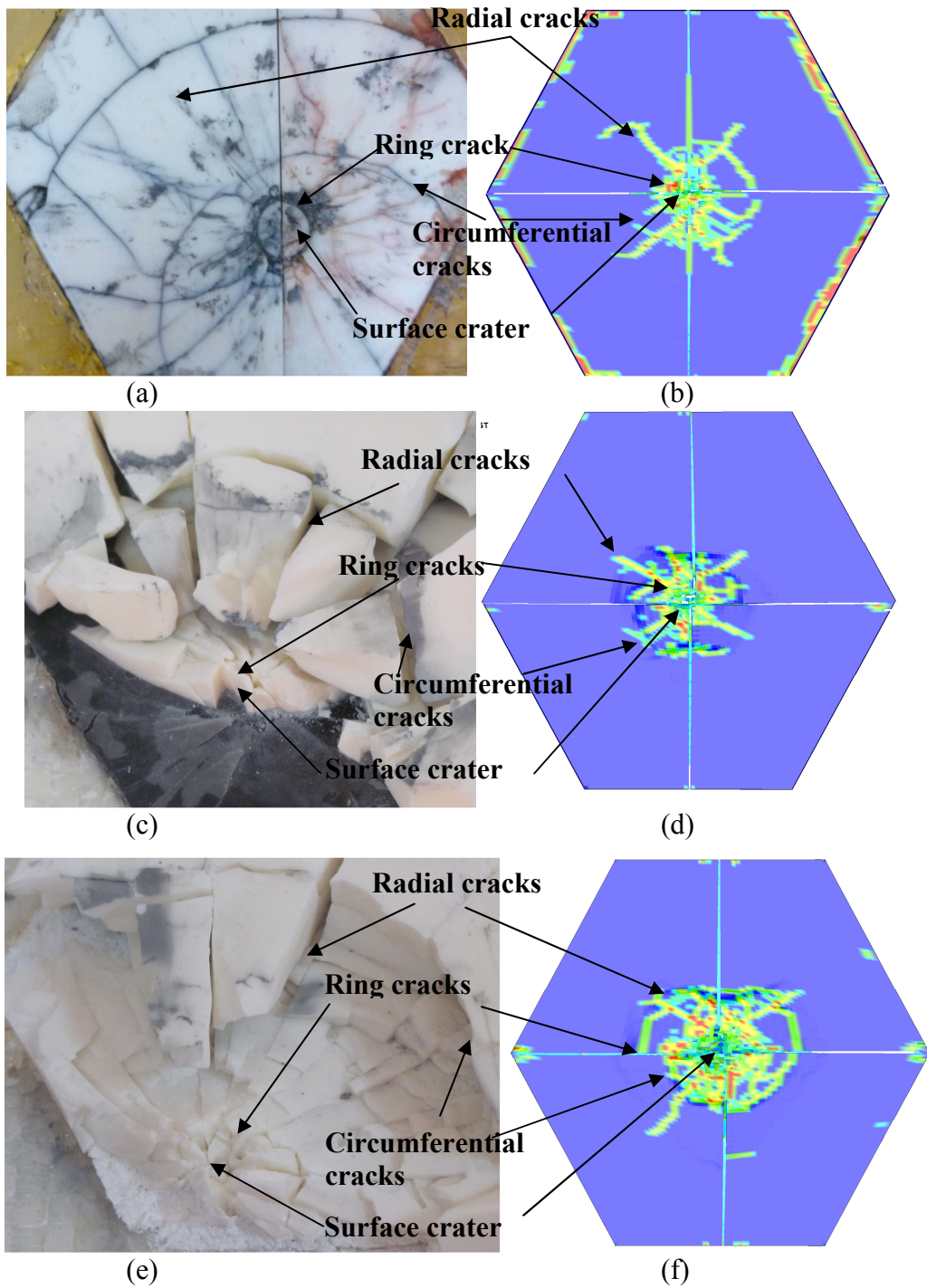


Figure 5.6. Damage occurred in ceramic layer.

Cone crack formed due to the effect of compressive loading was initiated on the top surface of ceramic layer with a ring shaped crack (resulted in shear component of transient pulse) and propagated towards the bottom surface. During this advance, circumferential cracks also occur. This phenomena separates the tile into two zones; (Sherman, 1997) primary one is surface crater, where the effective zone of high compressive stress in the tile. This localized high compressive stress is applied by conical shape hardened core projectile and increases the fragmentation of the projectile. Hence, it is a dominant mechanism operative in defeating projectile (Abrate, 2001). has demonstrated that the conoid angle of ceramic in his study is 65°, a boron ceramic tile backed by a metal plate. Then, (Zuoguang et al., 2010) formulated the relationship between the cone diameters on the top and bottom surfaces and thicknesses.

$$\tan \alpha = \frac{d_2 - d_1}{2h} \quad (5.1)$$

where α refers to the conoid angle, h is thickness, $D1$ and $D2$ are the diameters of cone on the top and bottom surfaces sequentially (Figure 5.7). As a result, α is calculated 59.0° experimentally and 58.2° numerically for no interlayer configuration. The deviation is around 1.3%. Similar results were also obtained for Teflon and EPDM rubber configurations.

Figures 5.8 ((a)-(d)) show the damage contours occurred in the ceramic layer for no interlayer and EPDM rubber, Teflon and Aluminum foam inter layer configurations. As it is seen in Figure 5.8 (a), the damage in ceramic layer is highly localized around the projectile hit zone. The rapidly stiffening EPDM rubber interlayer also causes damage to be localized around the projectile as seen in Figure 5.8 (b). Teflon and Aluminum foam interlayer on other hand spread the damage zone in radial direction, significantly altering the damage formation in the ceramic layer (Figure 5.8 (c) and (d)). These results reveal that the interface material can have a strong effect on the fragmentation behavior of the ceramic layer and the subsequent damage formation, caused mainly by the reflection of the compressive waves at the ceramic-interlayer interface due to the acoustic impedance mismatch. The spreading of the damage zone is beneficial in reducing the stress transferred to the composite backing plate. Similar results were obtained by (Zaera et al., 2000) with using different thicknesses and types of adhesives between ceramic front layer and metallic backing plate. In their study they

showed that with thicker layers of adhesive, the energy of the projectile, distributes over a wider area of the aluminum plate, gives rise to a greater deformation. The magnitude and duration of reflected stress waves depend on the interlayer material and the thickness and the material properties of the interlayer as well as the adjacent layers. EPDM rubber is a highly nonlinear material and its wave velocity is a function of stress-strain amplitude; therefore, the acoustic impedance and the transmission/reflection coefficients between adjacent layers are functions of the stress-strain amplitude. It was found experimentally, in the tested armor sample, that relatively large pieces of the ceramic around the impact axis in the EPDM rubber interlayer configuration are observed (Figure 5.5 (a)). While the ceramic layer is observed to be efficiently fragmented Teflon interlayer configuration as seen in Figure 5.5 (b). This further confirms the numerical simulation results. These observations are in agreement with the numerically determined damage counters which are represented by history variable 2 in LS-POST in the ceramic layer (Figure 5.8).

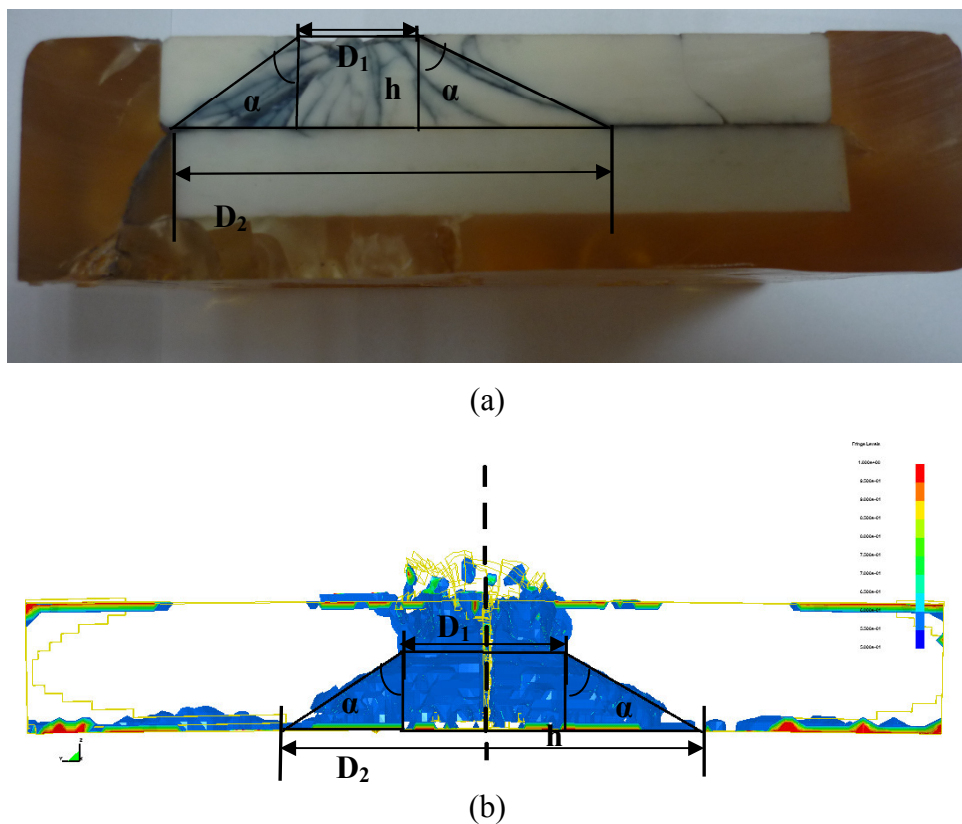


Figure 5.7. Fracture conoid: (a) experimental and (b) numerical.

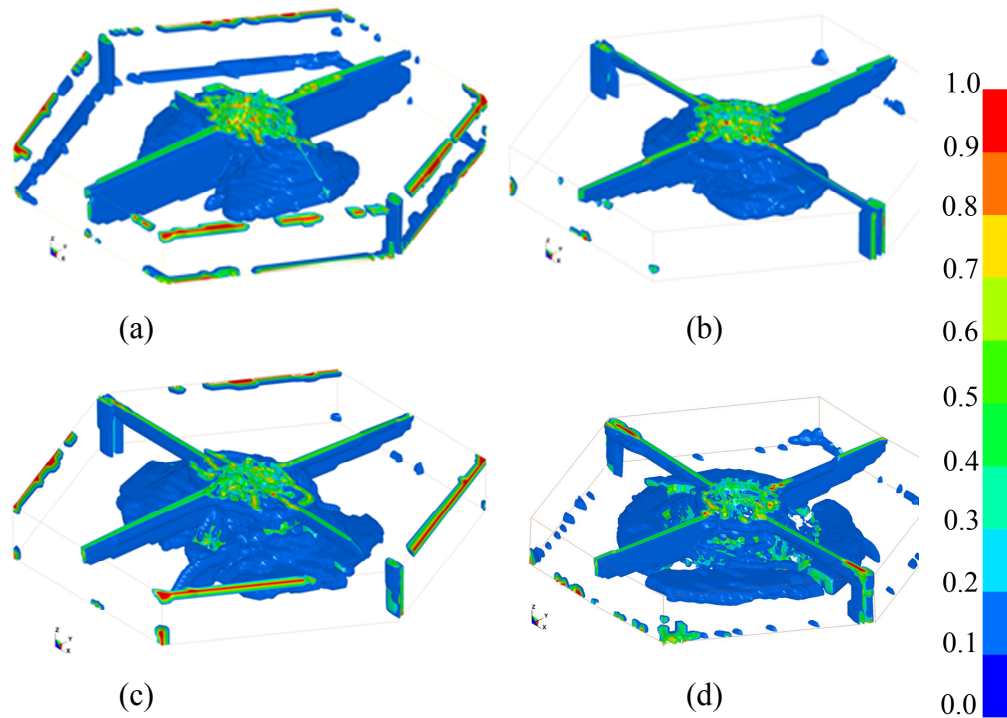


Figure 5.8. Damage occurred in ceramic layers of different configurations: (a) without interlayer, (b) EPDM rubber, (c) Teflon and (d) Aluminum foam.

Furthermore, in both ballistic tests and simulations, projectile did not perforate the multilayer armor system. Hence, ceramic was frequently shattered whereas backing plate delaminated completely with no visible damage except Aluminum foam. The reason that composite layer of Aluminum foam configuration did not experience significant damage is that, the stress Aluminum foam experienced did not exceed its plateau stress and it was not compressed till its densification strain.

Figure 5.9 ((a)-(d)) show the delamination (history variable 12 in LS-POST) occurred during the ballistic impact in the composite layer of without interlayer and EPDM rubber, Teflon and Aluminum foam interlayer configurations shown, respectively. The damaged area in the composite plate, as shown in the figures, is localized around the top outermost layers. The delamination in the composite layer is relatively narrower for Teflon and Aluminum foam interlayer configurations (Figure 5.9 (c) and (d)) than those of no and EPDM rubber interlayer configurations (Figure 5.9 (a) and (b)). In Aluminum foam interlayer configuration, the delamination area is noted to be significantly reduced (Figure 5.9 (d)). The present results clearly show that interlayer material has a significant effect on the ballistic performance of the composite armor.

Also, the extent of the delamination damage of the composite layer and fragmentation of the ceramic layer depend on the thickness of the interlayer material, the present results are only for the investigated interlayer thicknesses. The effect of interlayer is thicknesses on the ballistic performance and damage occurred is going to be given somewhere else in this thesis.

Similar to ceramic, miscellaneous damage modes were operative in composite layer during high impact tests. Figure 5.11 ((a)-(k)) exhibits fiber damage accumulation in the a and c directions of material for all configurations. Material directions inside composite are demonstrated in figure 5.10. Based on this a and b are the in-plane and c is normal directions.

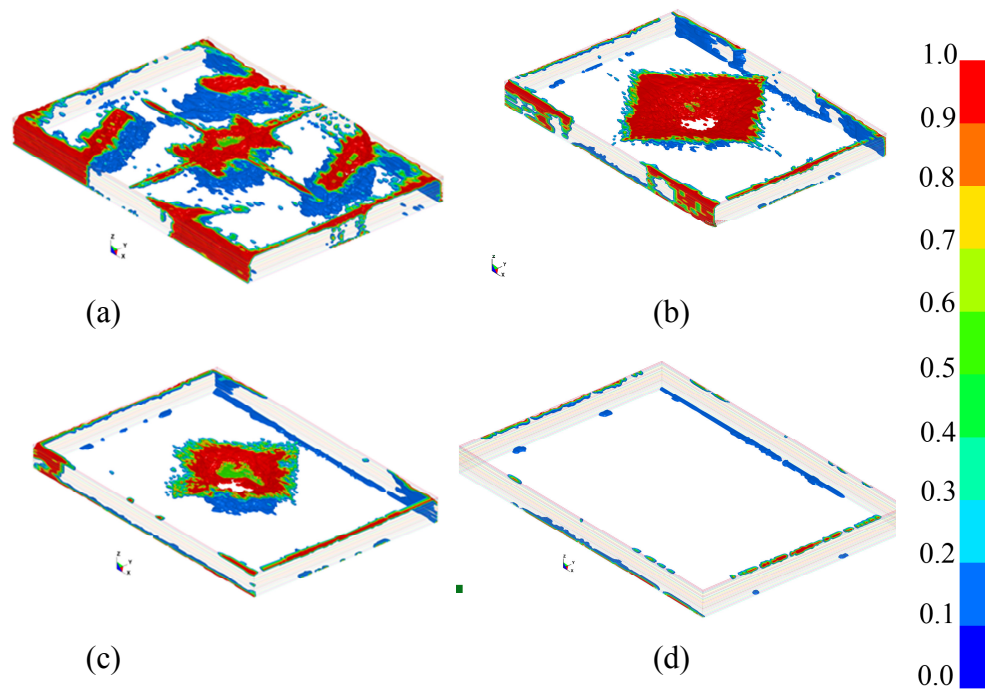


Figure 5.9. Delamination damage in the composite layers of different configurations: (a) without interlayer and (b) EPDM rubber, (c) Teflon and (d) Aluminum foam.

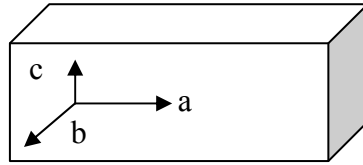


Figure 5.10. Material directions.

Figure 5.11 (a-h) demonstrate that, there was no significant damage in fibers along any direction. The damage was localized only on the top surface and became deeper without interlayer whereas no damage occurred for aluminum interlayer configuration. However, Teflon caused more localized fiber damage than EPDM rubber, as expected. Numerical model also provided detailed information about some experimentally unobtainable parameters, such as deceleration of projectile, residual mass and velocity and variation of significant energy values absorbed by the ceramic and composite layers. The tested and modeled four different armor configurations were coded as; (a) without interlayer (baseline) (WO), (b) with EPDM rubber interlayer (WR), (c) with Teflon interlayer (WT) and (d) with Aluminum foam interlayer (WF).

The variation of the projectile residual velocity and projectile mass with time for the studied four different armor configurations are shown in Figure. 5.12 (a) and (b), respectively. For the first $\sim 35 \mu\text{s}$, the projectile slows down to $\sim 250 \text{ m/s}$ and the deceleration behavior is almost the same irrespective as the type of interlayer material used; however, after that time slight deviations occur as seen in Figure 5.12 (a). The projectile velocity for without interlayer configuration decelerates at a faster rate than those of interlayer containing configurations, while the Aluminum foam interlayer is the least effective in slowing down the projectile velocity. In accordance with this, the highest amount projectile erosion occurs in without interlayer configuration, while the Aluminum foam interlayer leads to the lowest projectile erosion, as seen in Figure 5.12 (b).

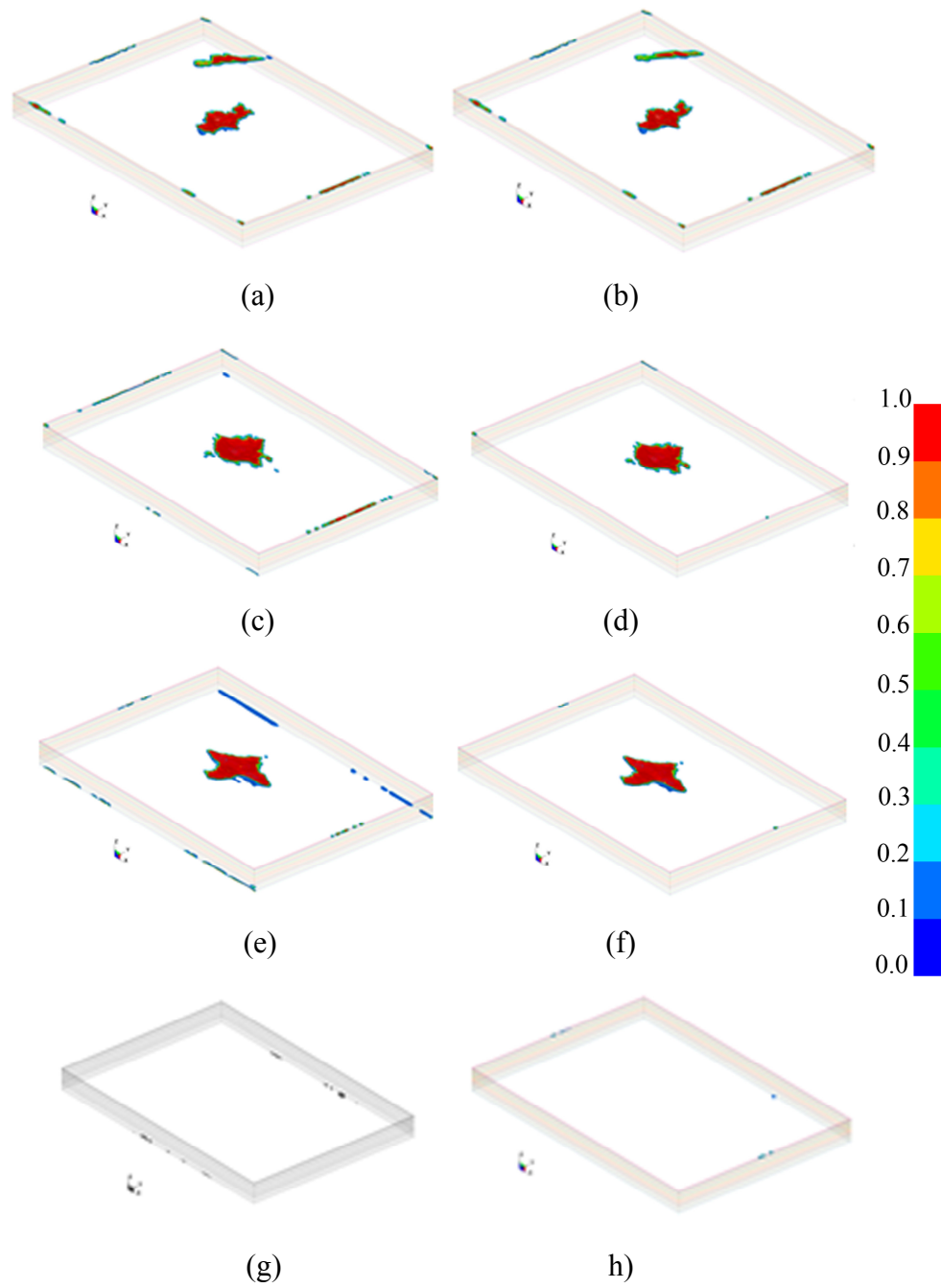


Figure 5.11. Fiber damage in the composite layers of different configurations in the in-plane and through-thickness directions consecutively: ((a)-(b)) without interlayer ((c)-(d)) EPDM rubber, ((e)-(f)) Teflon and ((g)-(h)) Aluminum foam.

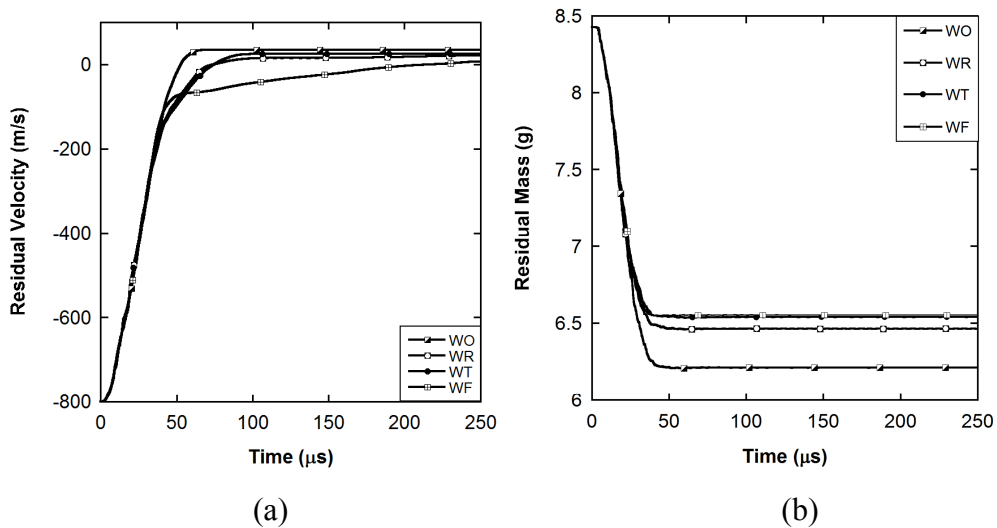


Figure 5.12. Projectile (a) residual velocity and (b) mass vs. time.

Figure 5.13 shows the variation of the eroded projectile energy with time for the investigated armor configurations. As seen in this figure, without interlayer configuration exhibits the maximum amount of eroded energy of the projectile, which in considering the highest amount of projectile erosion in this configuration. It is also noted in the same figure that the presence of an interlayer results in reduction in eroded energy of the projectile.

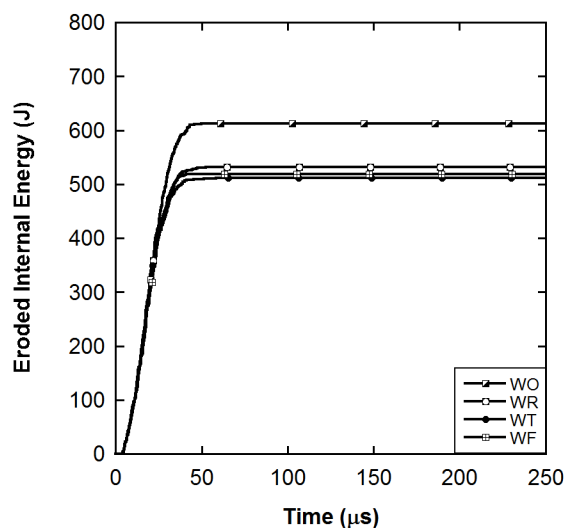


Figure 5.13. The eroded energy history of projectile.

Kinetic energy of projectile is transferred to the armor constituents and absorbed through different damage mechanisms during impact. Since the LS-DYNA calculations are based on conservation of energy, initial kinetic energy of projectile, which is equal to the total energy of system, is formulated by the equations given below.

$$KE_{\text{projectile}}^0 = \text{TOTAL E} = KE + IE + HGE_{\text{erode}} + HGE_{\text{nonerode}} + \text{SLE} \quad (5.2)$$

$$KE = KE_{\text{nonerode}} + KE_{\text{erode}} \quad (5.3)$$

$$IE = IE_{\text{nonerode}} + IE_{\text{erode}} \quad (5.4)$$

Where KE, IE are kinetic and internal energies of the system sequentially, and SLE refers to sliding energy between interfaces which determines the global energy balance (Deka et al., 2008). KE_{nonerode} and IE_{nonerode} are the kinetic and internal energies of non-eroded elements in the model whereas KE_{erode} and IE_{erode} refer to those of eroded (Figure 5.14). HGE_{nonerode} and HGE_{erode} refer to hourglass energies of remaining and eroded elements in the system consecutively. Hourglass (HG) energy modes are nonphysical, zero energy modes of deformation that produce zero strain and no stress. Mostly it is expected that HGE_{nonerode} does not exceed 10% of the peak of IE_{nonerode} of each part. In this study, hourglass of composite was formulated by type 4, a stiffness based control, minimizing the distortion of elements and accordingly reducing the hourglass modes in elements (Deka et al., 2008). Other constituents were hourglass type 3, suitable for high velocity impact problems of solid structures and provide viscosity-based control.

Energy balance of base configuration was verified (Figure 5.15). Total energy of the system, initially equal to kinetic energy of projectile, is equal to sum of sliding, hourglass, internal and kinetic energies of the system. Moreover, HGE_{remain} is less than 10 percent of IE of each part. 3%, 25% and 43% of the initial energy is absorbed by composite, ceramic and projectile (by erosion) consecutively as seen in Figure 5.16. The remaining is dissipated as HGE_{erode} and SLE. Greater amount of energy is also dissipated in erosion at ceramic-projectile interface.

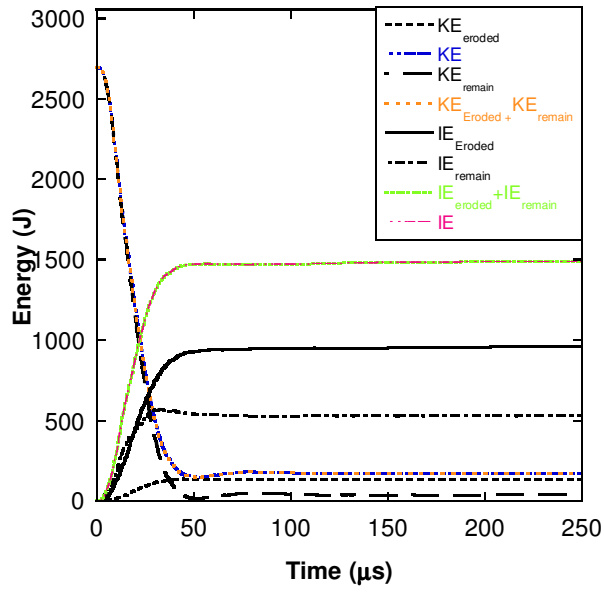


Figure 5.14. Internal and kinetic energies of eroded and non-eroded elements.

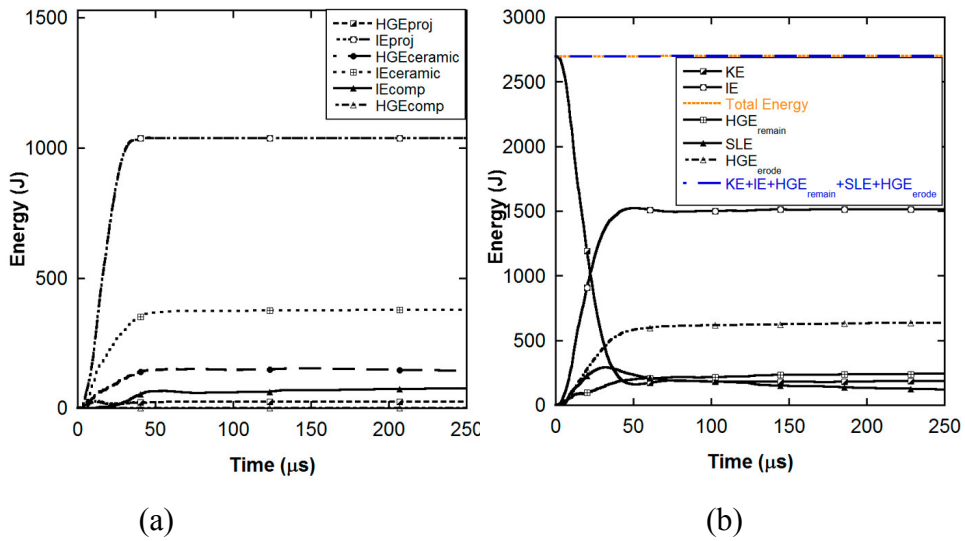


Figure 5.15. Energy balance in aspects of (a) conservation of energy and (b) hourglass energy ratio.

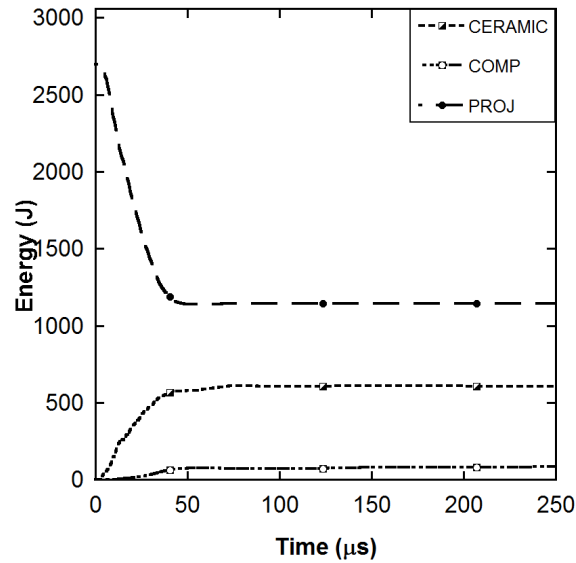


Figure 5.16. Energy dissipation in armor constituents.

The variations of the ceramic layer internal, kinetic and eroded internal energy with time are shown in Figure 5.17 (a), (b) and (c), respectively. As the projectile penetrates through the ceramic layer, the internal energy of the ceramic layer increases initially and then gradually decreases as seen in Figure 5.17 (a). Although without interlayer configuration ceramic layer shows relatively low peak energy values initially, the final value of the internal energy is the highest at 250 μs among all the configurations studied. Correspondingly, the kinetic energy increases in about 50 μs , and then decreases (Figure 5.17 (b)). The kinetic energy imparted to the ceramic layer in Teflon and Aluminum foam interlayer configurations is significantly higher than that of without interlayer and EPDM rubber interlayer configurations. This behavior is partly attributed to the relatively low axial modulus of the foam initially and during the projectile impact. The kinetic energy of the projectile is also dissipated as the projectile deforms and erodes, resulting in an increase in the eroding internal energy of the ceramic layer (Figure 5.17 (c)).

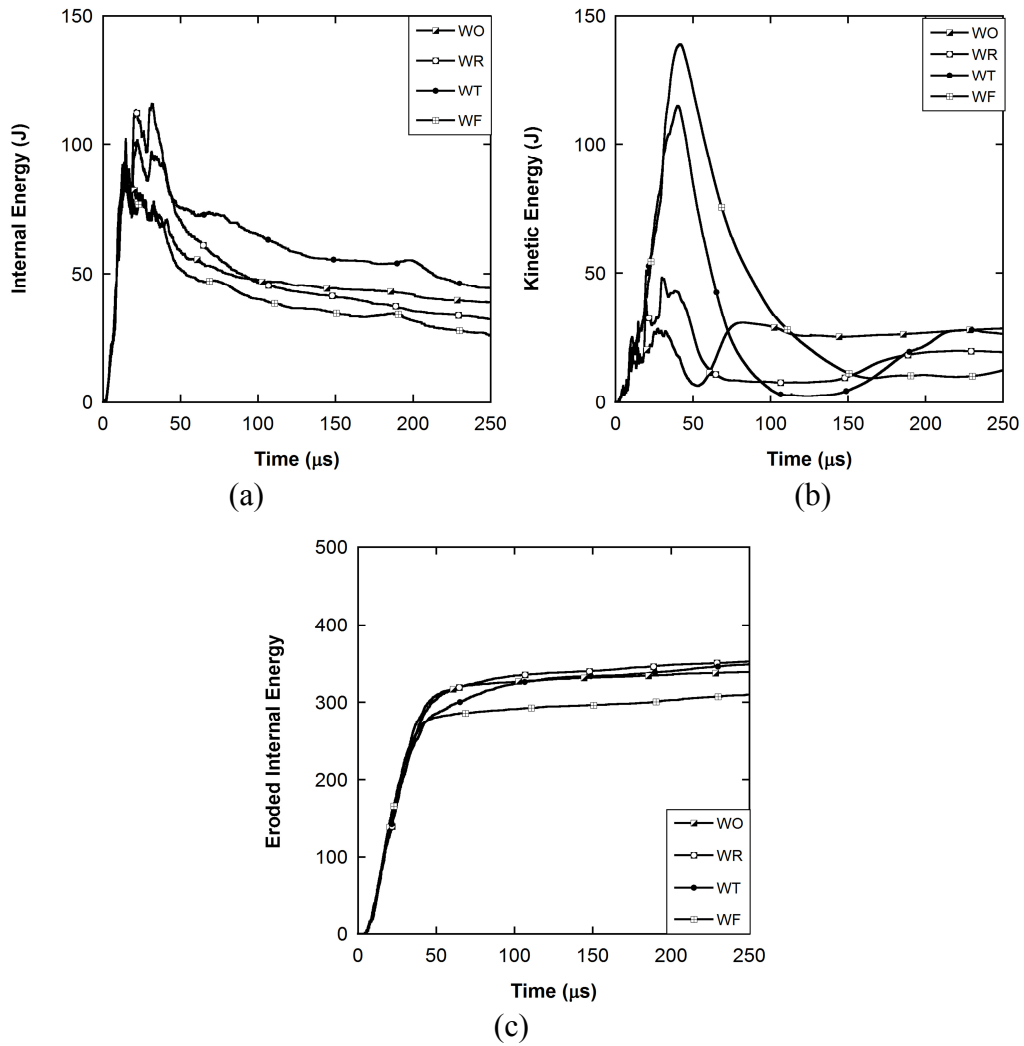


Figure 5.17. The energy histories of the ceramic layer: (a) internal, (b) kinetic and (c) eroded internal.

Figure 5.18 (a) and (b) show the kinetic and total internal energy histories of the composite layer for the studied configurations. The simulations clearly indicate that the interlayer material has a strong effect on the energy transmitted to the composite layer during the projectile penetration. The similar kinetic energy increase in without interlayer and EPDM rubber interlayer configuration (Figure 5.18 (a)) confirms the increase of the EPDM rubber stiffness rapidly during penetration. Teflon and Aluminum foam layers however cause significant delay in the energy histories (Figure 5.18 (a) and (b)). It is also noted in Figure 5.18 (a) and (b) that the Aluminum foam interlayer drastically reduces the amount of kinetic and total internal energies of the composite plate.

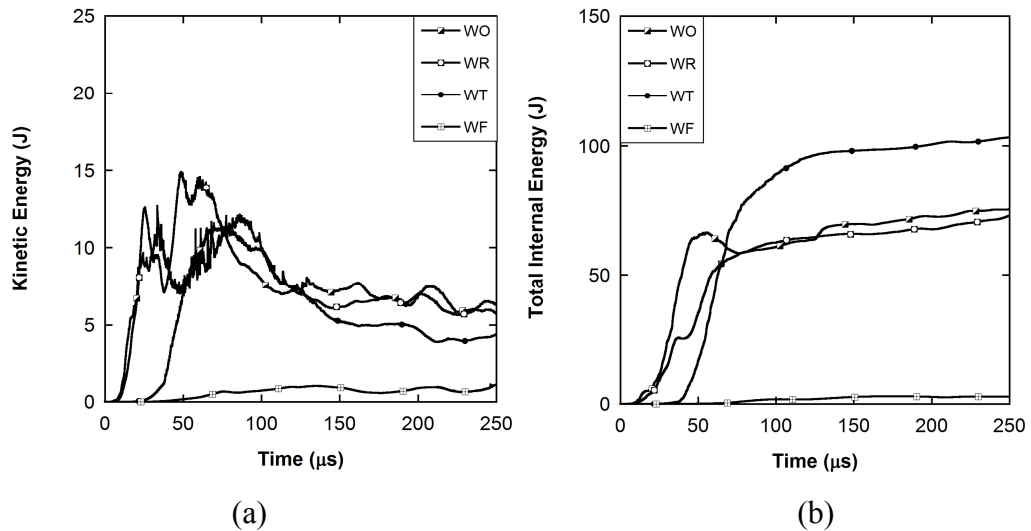


Figure 5.18. The energy histories of the composite plate: (a) kinetic and (b) total internal.

Figure 5.19 depicts the distribution of the Z-force (the force in the projectile impact direction) at the interlayer-composite interface (between interlayer and composite layer). The presence of an interlayer between ceramic and composite layer as seen in Figure 5.19 alters the stress wave transmission to the composite backing plate. It is noted in the same figure that the presence of EPDM rubber interlayer causes no delay in the initial force build-up in the composite for the first $\sim 35 \mu\text{s}$, while it decreases the force values at the later stages of the impact as compared with without interlayer configuration. Although the EPDM rubber interlayer has very low impedance initially, as the projectile penetrates into the ceramic layer its impedance rises rapidly. This is attributed to the constraining effect of surrounding material on the radial deformation of the interlayer in the vicinity of the projectile impact zone and the relatively high Poisson's ratio of the EPDM rubber. A similar behavior of EPDM rubber subjected to compressive stress wave loading was previously reported by Gama et al. (Gama, 2000; 2001). It was shown that relatively low modulus EPDM rubber interlayer delayed the passage of the elastic stress wave into the composite and reduced the stress amplitude. It was also claimed that the damage in the composite layer was reduced in the presence of EPDM rubber interlayer. For Teflon and Aluminum foam interlayer, the behavior is quite different; the force values transmitted to the composite layer decreases significantly (Figure 5.19). Teflon and Aluminum foam interlayer also result in delays in the stress wave transmission to the composite backing

plate. For Teflon and Aluminum foam interlayer configurations, the axial modulus of the interlayer remains relatively low during most of the deformation process. Gama et al. (Gama et al., 2001) previously showed that Aluminum foam interlayer in multilayered armor system behaved like a stress filter and effective stress wave transmission could only occur when the foam was completely densified.

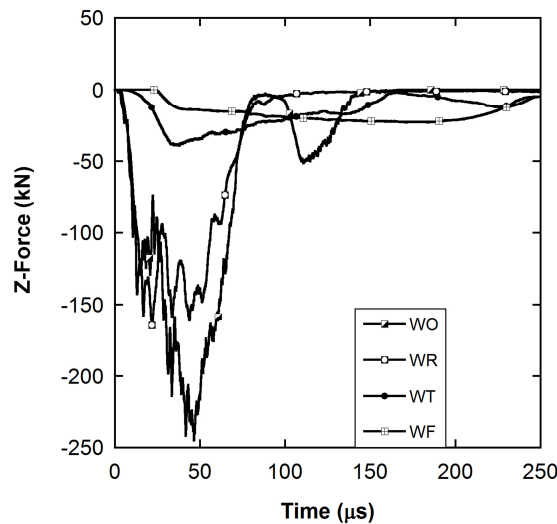


Figure 5.19. The Z-force history at the interlayer-composite interface.

Since the main stress wave propagation direction is along the through-thickness, effectiveness of interlayer in composite is demonstrated by the stress/time/distance maps along elements located in composite layers along through-thickness direction. Elements groups along through thickness direction and at $\sim 2/5$ and $3/5$ radial distances of ceramic (25.44 and 36.18 mm) were selected consecutively and illustrated by B and C in the figures. The element notation is demonstrated in Figure 5.20. Stress variation along chosen elements was saved from LS-DYNA. The resolution of this output is critical since there is a critical time step which must be adequately selected. Time step was calculated automatically by LS-DYNA and the initial time step was determined. As program looped through the elements, a new step size was determined by taking the minimum value over all elements during solution.

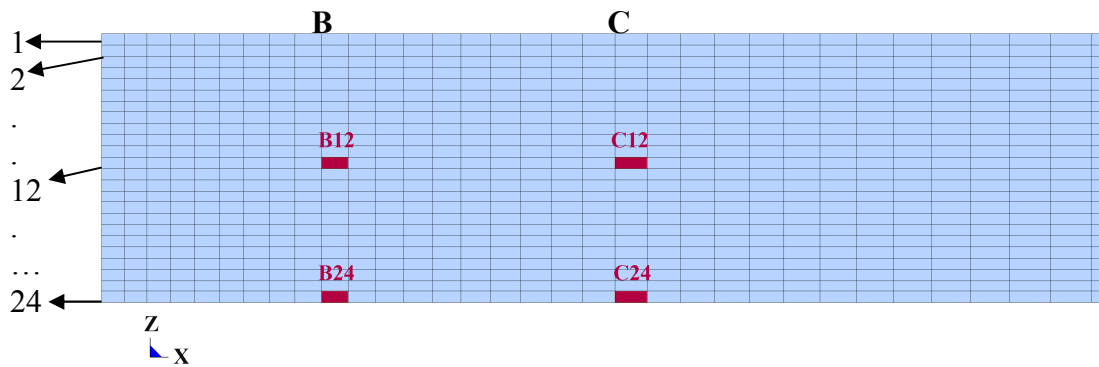
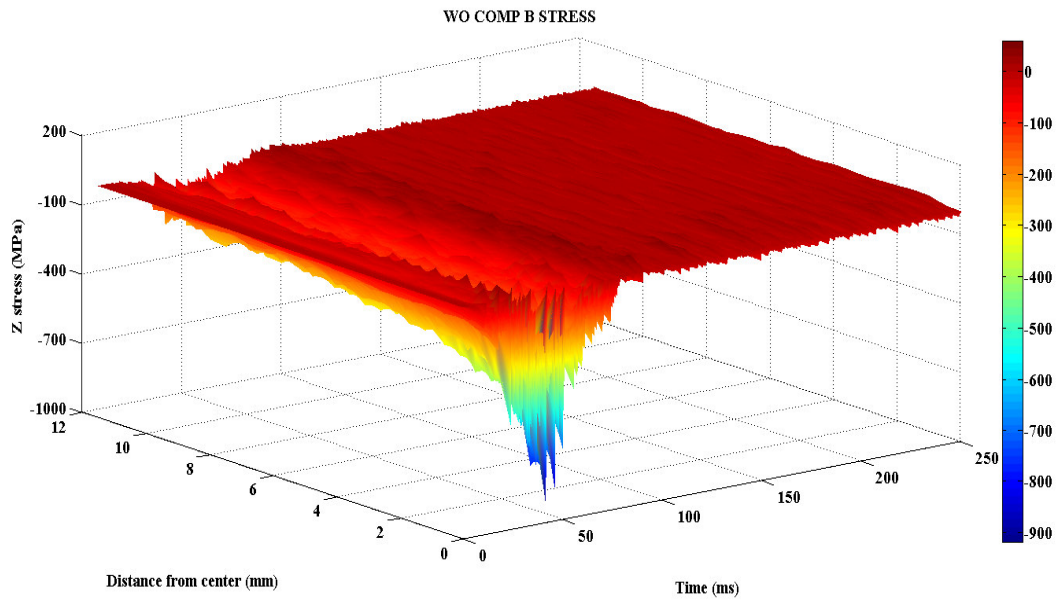


Figure 5.20. Element notation of stress/time/distance maps.

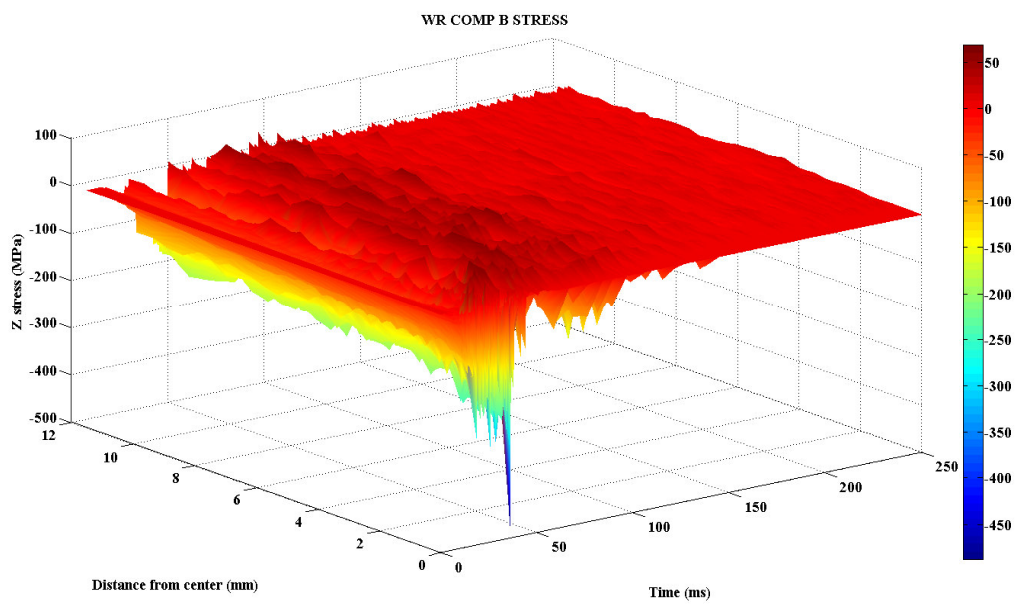
Stress/time/distance maps demonstrate that interlayer cause the mitigation of stresses level which composite experiences. The peak stress value observed in without interlayer configuration is ~ 1000 MPa, while 500 MPa was not exceeded for the interlayered configurations. Figure 5.21 (b), (c) and (d) demonstrate that, the compressive stress values observed in Teflon and EPDM rubber cases were about 400-500 MPa, while this value being almost zero for Aluminum foam configuration. Also, the level of stress mitigation Teflon interlayer was higher than that of EPDM rubber. EPDM rubber provides narrower and shallower stress pulse with higher magnitudes along the through-thickness direction as seen in Figure 5.21 (b).

The stress values on top layers observed higher and along through-thickness direction, stress drastically was decreased to Teflon. Since, the stress wave propagated along the in-plane direction in EPDM rubber interlayer configurations was higher than that of Teflon. To understand the effect of stress wave propagation in the in-plane direction, stress/time/distance maps of elements at C is drawn for all configurations.

The peak stress values along line C for without, EPDM rubber and Teflon interlayer cases are ~ 300 , ~ 250 , ~ 50 MPa sequentially. It is indicated that stress propagated along the in-plane direction for without and with EPDM rubber interlayer configuration, whereas not highly effective for Teflon.



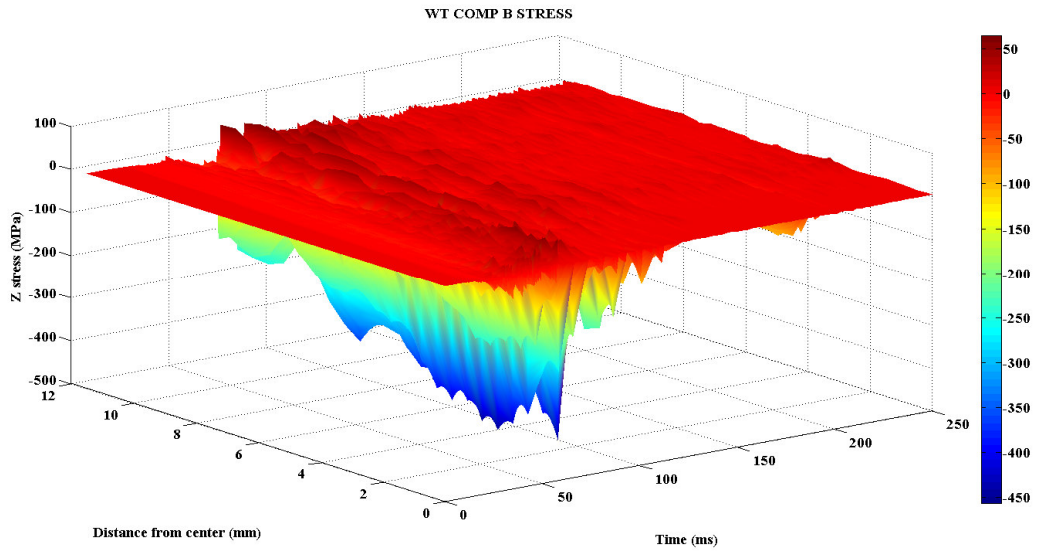
(a)



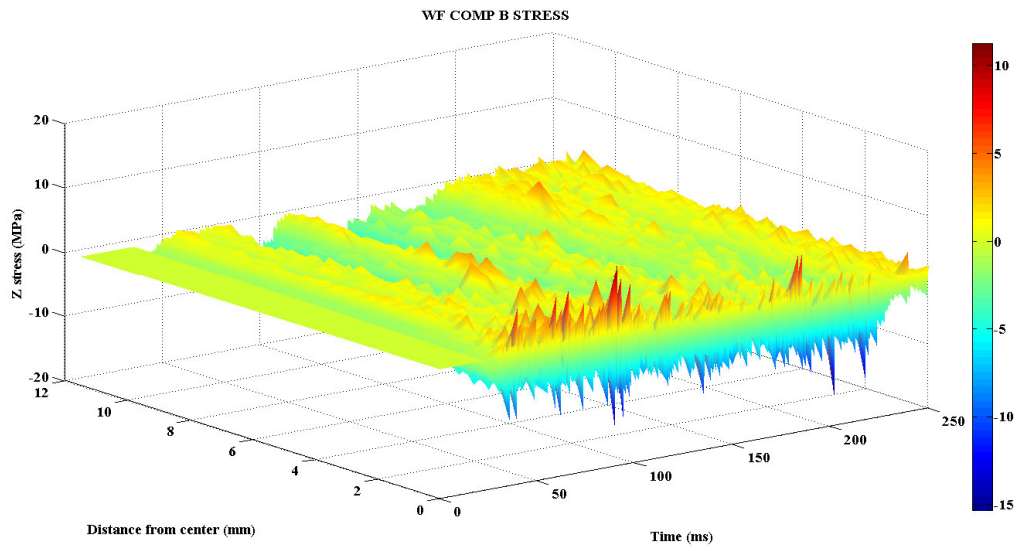
(b)

Figure 5.21. Stress/time/distance maps along line B on composite layer of different interlayer configurations: (a) without, (b) with EPDM rubber, (c) Teflon and (d) Aluminum foam.

(Cont. on next page)

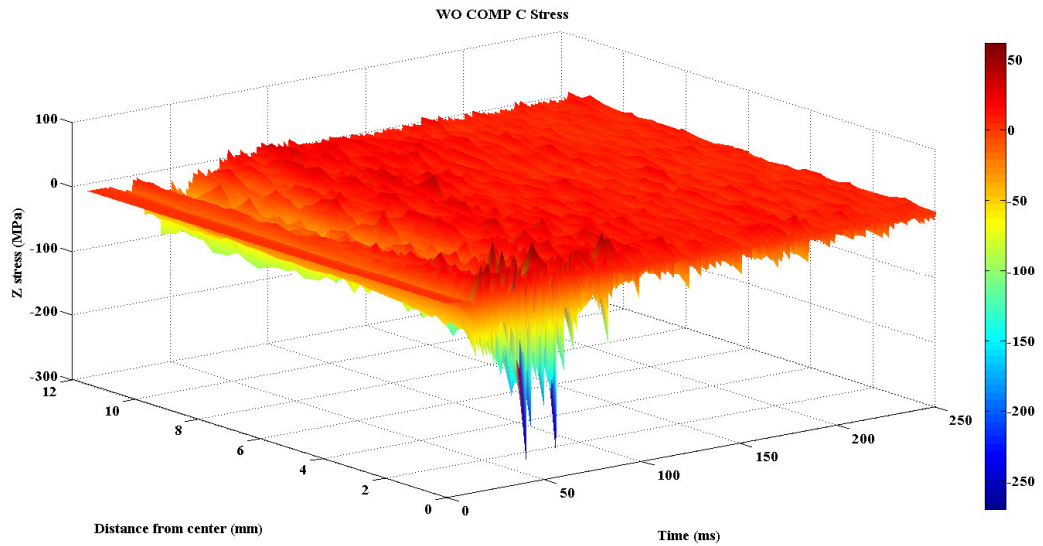


(c)

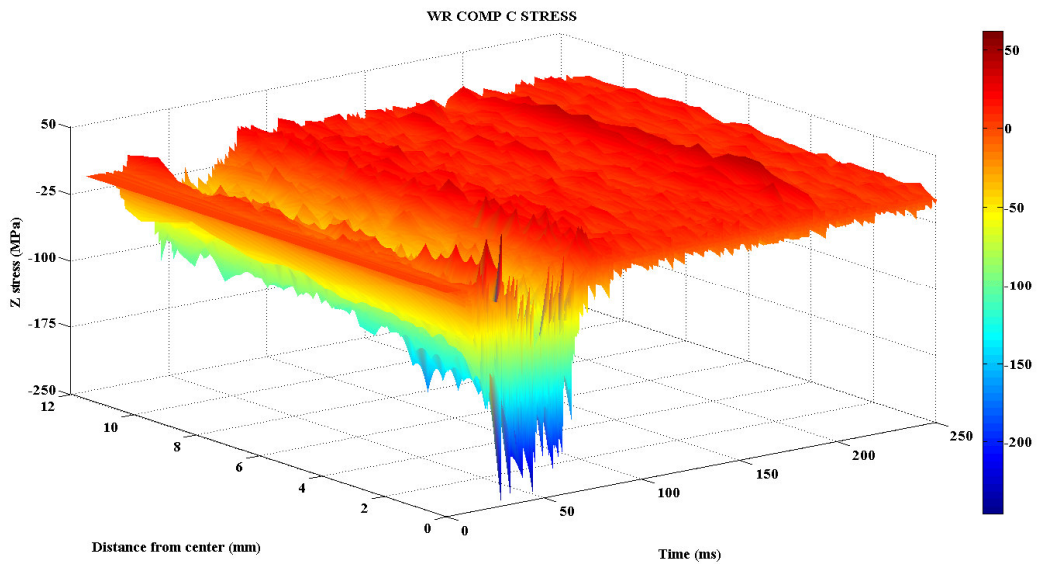


(d)

Figure 5.21. (Cont.)



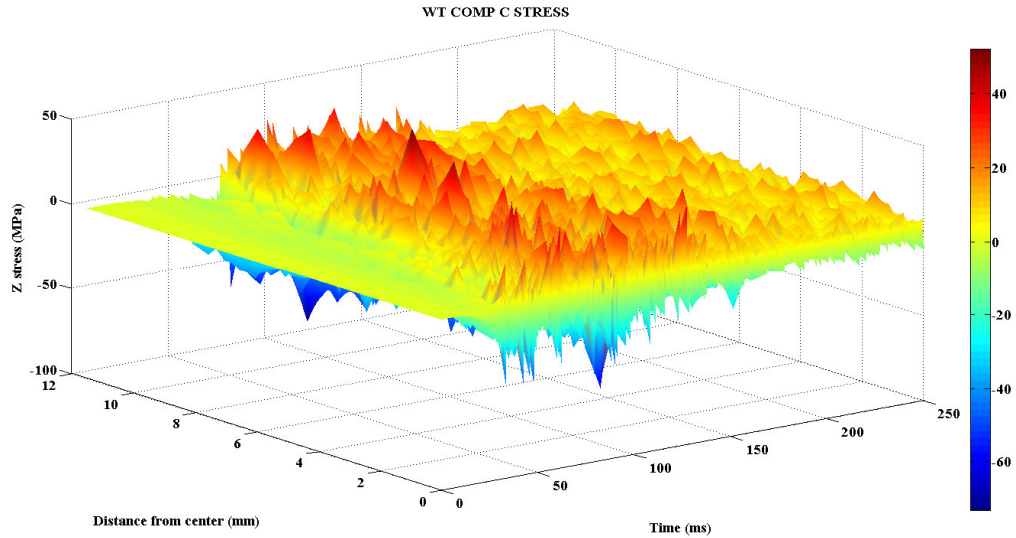
(a)



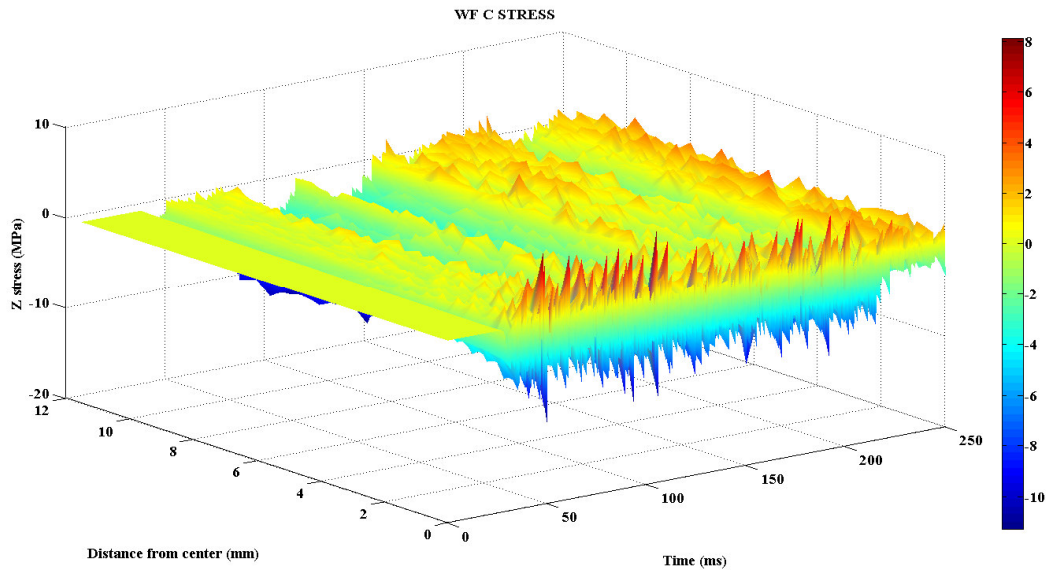
(b)

Figure 5.22. Stress/time/distance maps along line C on composite layer of different interlayer configurations: (a) without, (b) with EPDM rubber, (c) Teflon and (d) Aluminum foam.

(Cont. on next page)



(c)



(d)

Figure 5.22. (Cont.)

To understand the behavior of interlayers, stress wave distribution in each layer was investigated and the variation is given in Figures 5.21 and 5.22. To analyze the stress wave mitigation and time rise delay, stress vs. time data at B12 and C12 elements were compared in Figure 5.23.

Figures 5.21, 5.22 and 5.23 indicate that stress pulse widens and its amplitude decreases more than 75%, while moving in the in-plane direction from elements B to C. The decrease in the amplitude of stress wave in the in-plane direction is more pronounced for Teflon configuration. Owing to the low Poisson's ratio of Teflon layer,

acoustic impedance stays at lower values for longer times during the ballistic impact. Thus, less amount of stress wave was transmitted in the in-plane direction, resulted a small amount of local damage in the composite.

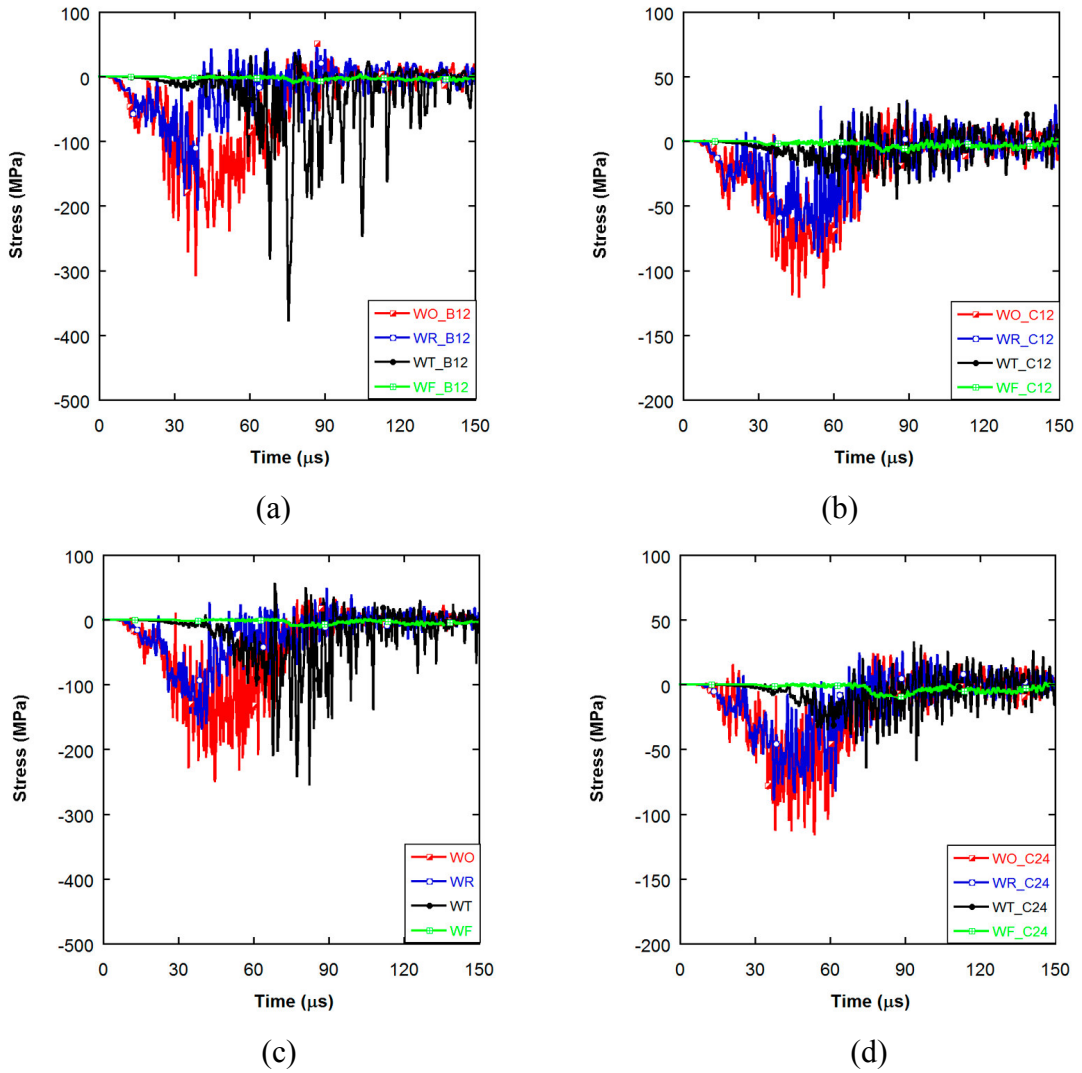


Figure 5.23. Stress vs. time data of different elements for all configurations: (a) B12, (b) C12, (c) B24 and (d) C24.

During ballistic penetration, the material around projectile hit zone is confined by the surrounding material. When the EPDM rubber interlayer is constrained, its modulus rapidly increases under the compression: the increase in modulus reduces the acoustic impedance mismatch between ceramic and composite layers (Tasdemirci, 2005). This mismatch causes relatively smooth transition in z-stress from ceramic to

composite as seen in the figures below. Presence of Teflon provides stress-rise time delay about 15 μs . Likewise Aluminum foam interlayer cause $\sim 25 \mu\text{s}$ stress-rise time delay as seen in Figure 5.24.

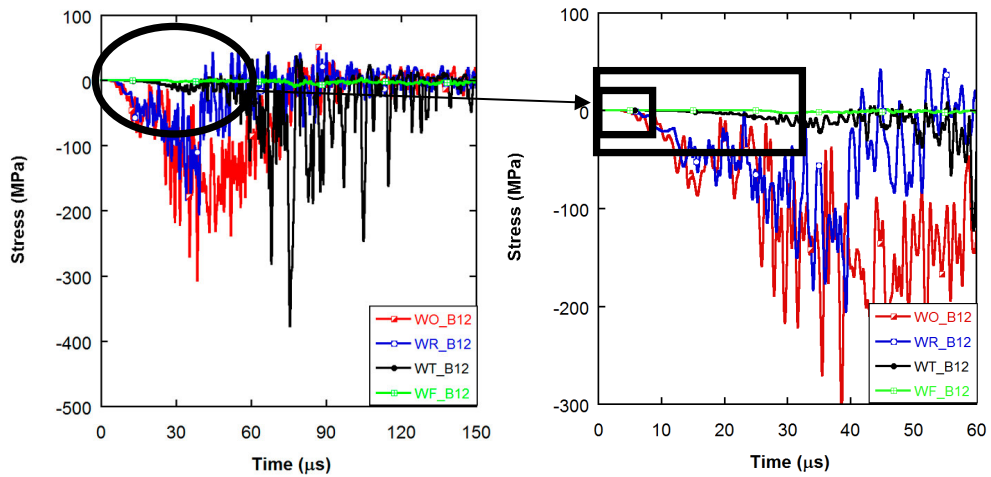


Figure 5.24. Stress rise time delay in Teflon and Aluminum foam.

As deformation proceeds, Teflon was eroded away at around $\sim 55 \mu\text{s}$ and the stress waves were transmitted to B12 element of composite after $\sim 20 \mu\text{s}$ thereby, the peak stress transmitted to B12 suddenly rises at $75 \mu\text{s}$ as demonstrated in Figure 5.25.

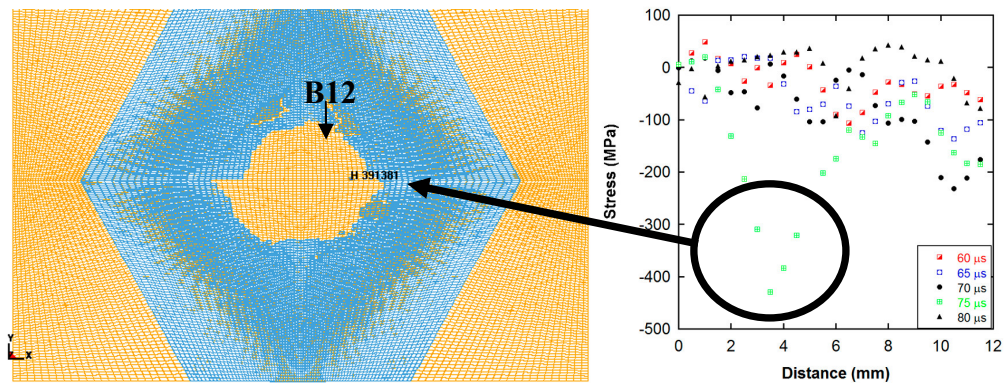


Figure 5.25. Complete erosion of Teflon.

5.4. The Effect of Interlayer Thickness on Ballistic Performance

In the previous chapter, the effect of 1.5, 2, and 18 mm EPDM rubber, Teflon and Aluminum Foam interlayers, at different areal densities, was investigated. Experimental and numerical results indicate that, Aluminum foam and Teflon interlayers cause ceramic layer to be efficiently fragmented. Hence, significant reduction in amplitude of transmitted stress wave and considerable time delay is provided. In order to investigate the effect of thickness at similar areal densities, 4 and 8 mm thick Aluminum foam and their corresponding 2.3 and 4.6 mm thick Teflon interlayer configurations were modeled and are demonstrated in Figure 5.26.

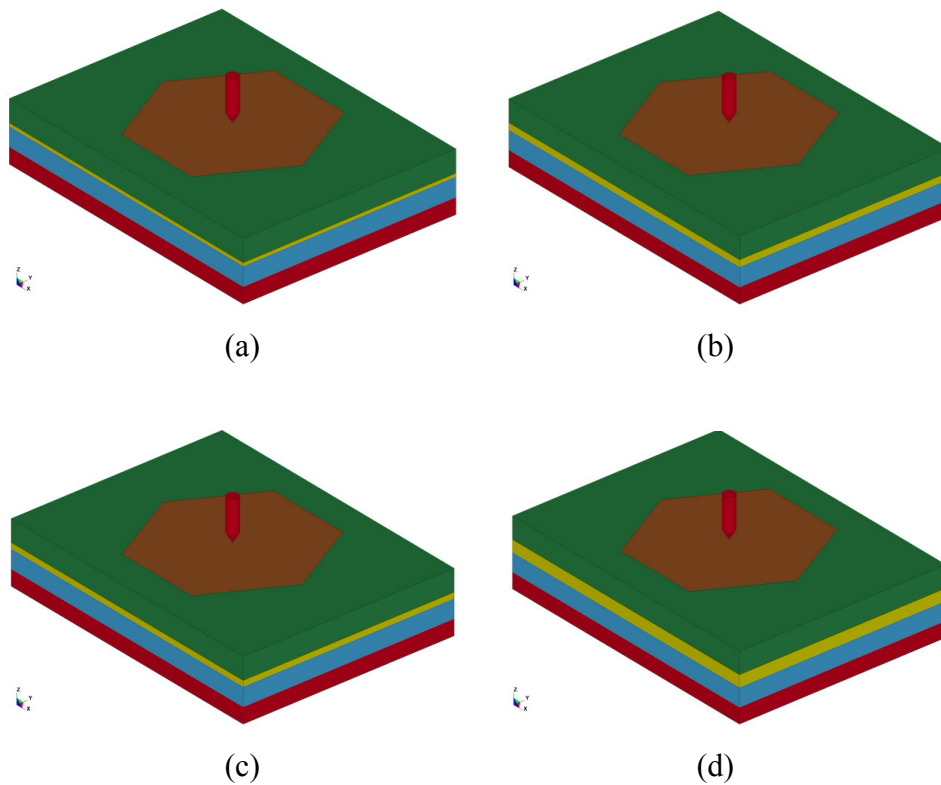


Figure 5.26. Numerical models: ((a)-(b)) 2.3 and 4.6 mm Teflon, ((c)-(d)) 4 and 8 mm Aluminum foam.

Within the first 50 μ s, the projectile penetrated into ceramic, internal and kinetic energies of the ceramic increased while projectile mass and velocity significantly decreased (Figure 5.28). It is noted that great amount of projectile kinetic energy was

absorbed in this 50 μs time period and the remaining energy was transmitted to the composite layer (Figure 5.28 (a) and (b)). After 50 μs , energy values in ceramic layer started to decrease, whereas in composite layer increase up to a certain time limit (Figure 5.27).

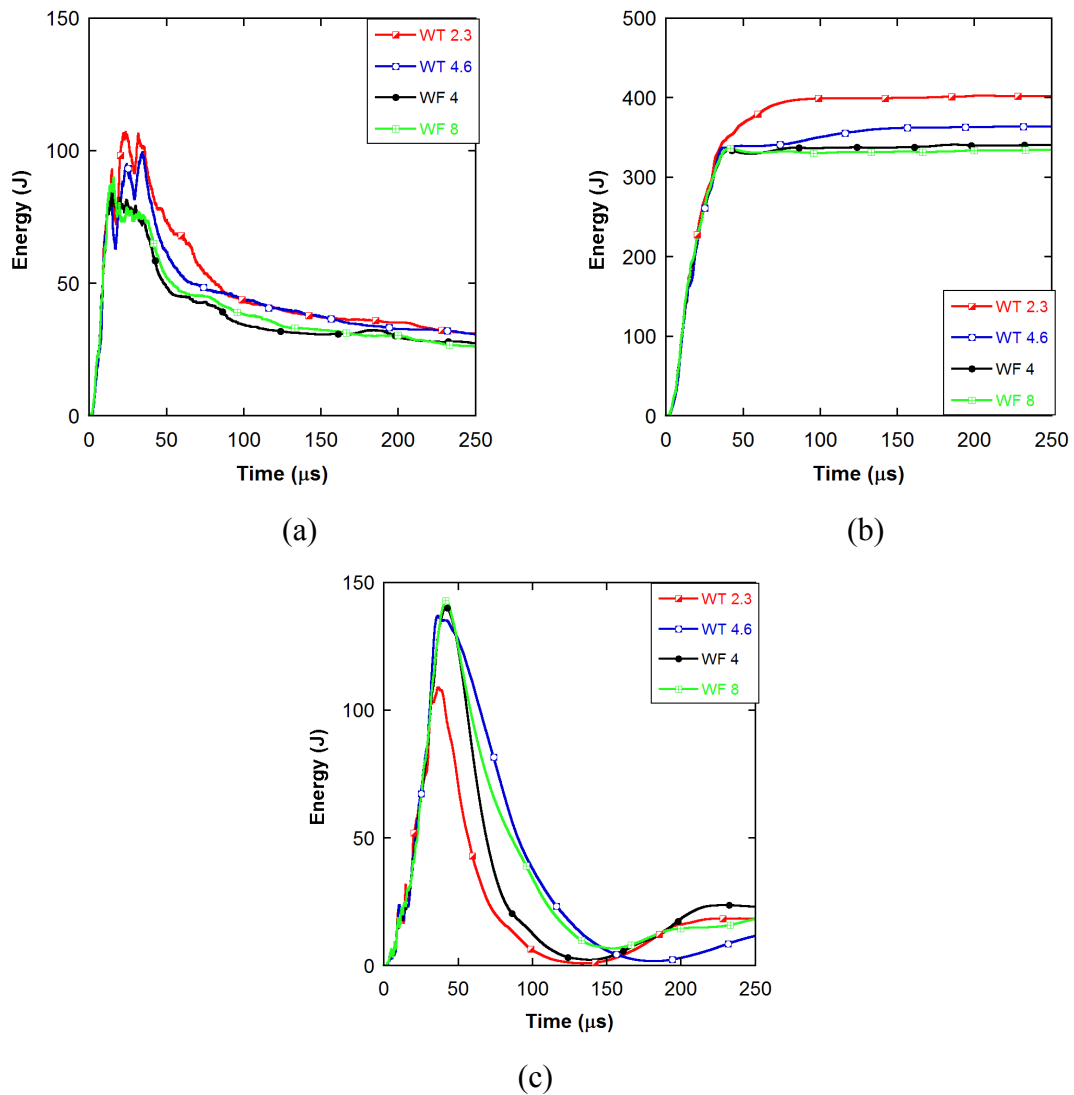


Figure 5.27. Energy histories of the ceramic layers: (a) internal, (b) total internal and (c) kinetic.

Similar to the ballistic tests and simulations, Aluminum foam was not completely compressed for 4 and 8 mm interlayer configurations (Figure 5.30). Accordingly, much of the stress wave was reflected from the ceramic-Aluminum foam

interface, thereby ceramic fragmented more efficiently. This increased amount of ceramic is in contact with the projectile so, the amount of erosion is increased, residual mass of projectile decreased and internal energy of ceramic increased for both aluminum armor configurations. Since 2.3 mm Teflon was almost completely eroded during penetration, ceramic and composite layers came into direct contact. Fractured ceramic region was backed by composite layer at longer durations and also the acoustic impedance mismatch reduced. Thus, the amplitude of transmitted compressive to the composite layer increased. Hence, projectile applied higher stress levels to ceramic since ceramic layer was directly supported by composite layer, and kinetic energy of ceramic decreased, as seen in the figures below. As the thickness of the interlayer increases, the distance that can be travelled by the ceramic layer increases, correspondingly kinetic energy increases.

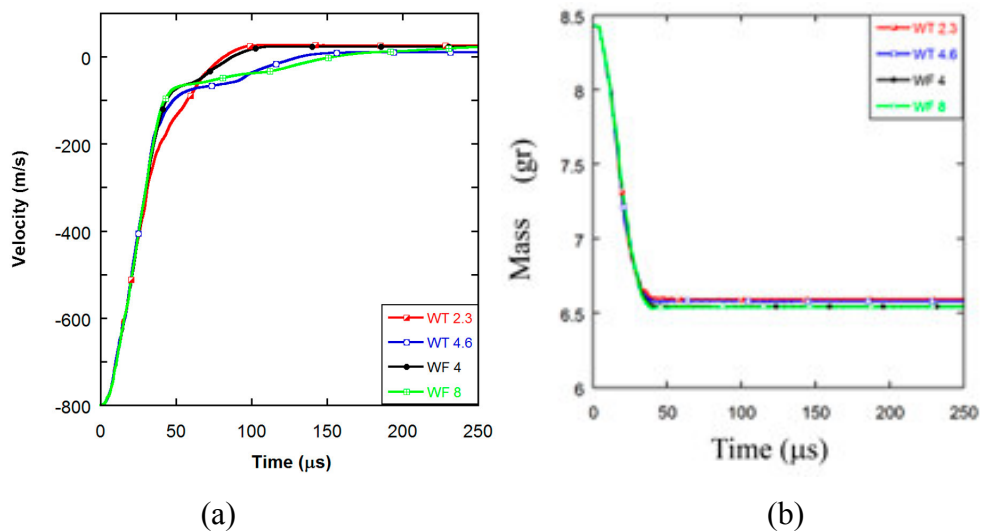


Figure 5.28. Projectile (a) residual velocity and (b) mass vs. time data of different thickness configurations.

Figure 5.29 shows that the increase of areal density caused significant delay in wave transmission. While 4.6 mm Teflon and its correspondence 8 mm Aluminum foam (having equal areal density) configurations transmitted to composite layer after 50 microseconds, 2.3 mm Teflon and 4 mm Aluminum foam had already started. Moreover, magnitude of any kind of energy in composite layer of Aluminum foam

armor was lower than Teflon. It confirms that, aluminum absorbs the larger amount of energy and less amount was transmitted to composite.

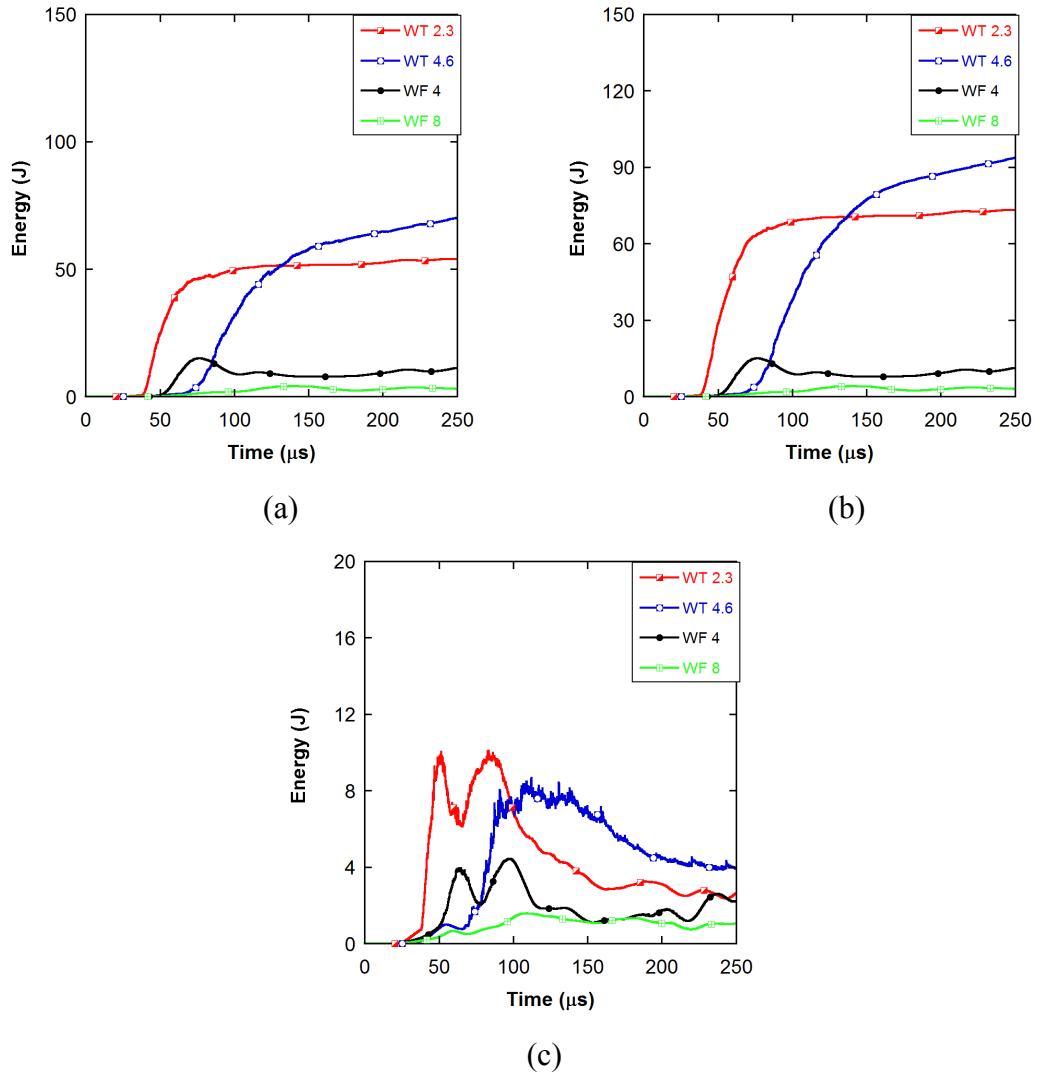


Figure 5.29. Variations of : (a) internal, (b) total internal and (c) kinetic energies of composite layer.

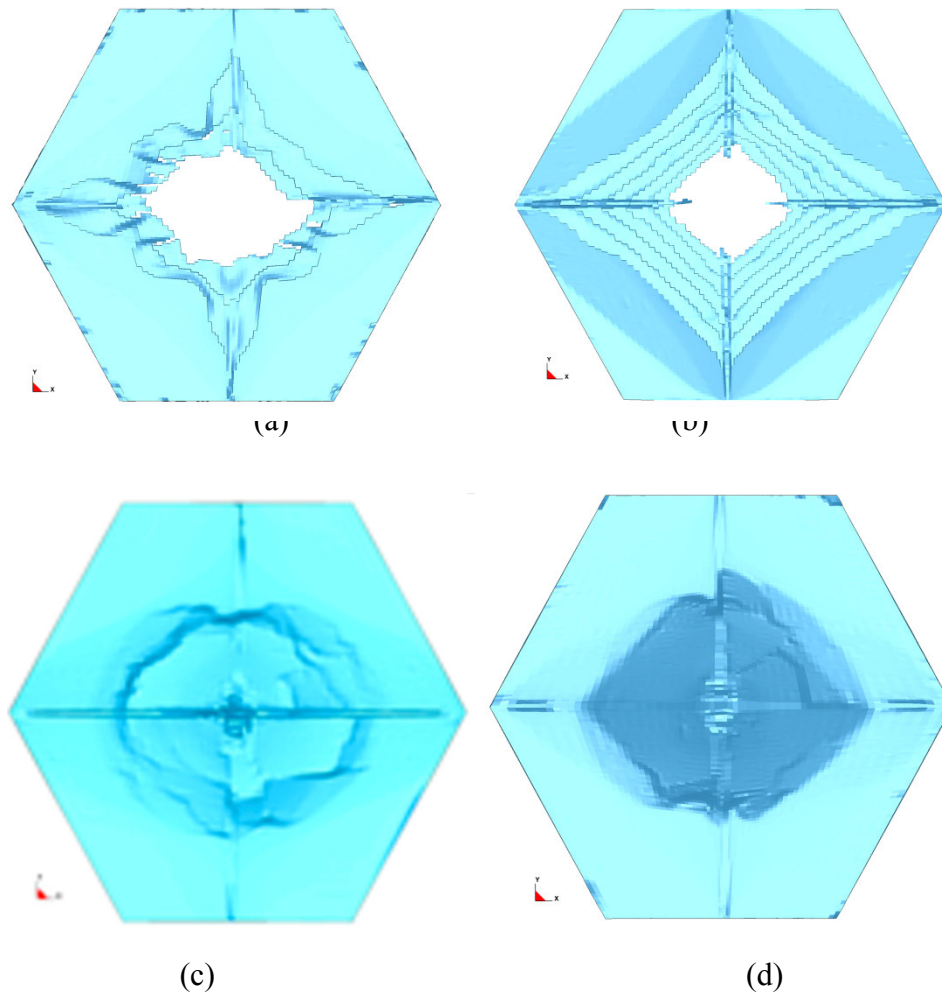


Figure 5.30. Top views of (a) 2.3 and (b) 4.6 mm Teflon (c) 4 and (d) 8 mm Aluminum foam 250 μ s after impact.

Figure 5.31 demonstrates that damage occurred in ceramic layer of Aluminum foam configuration is wider and deeper than Teflon for both areal densities. Since, Aluminum foam was not compressed to the densification region, greater amount of ceramic was fragmented and the interaction between ceramic debris and projectile was increased. Accordingly, greater portion of projectile was eroded and higher amount of energy was absorbed by ceramic layer in Aluminum foam configuration. Hence, the amount of wave and energy was transmitted to the composite layer decreased. So, almost no damage existed in composite layers of Aluminum foam configurations (Figure 5.32).

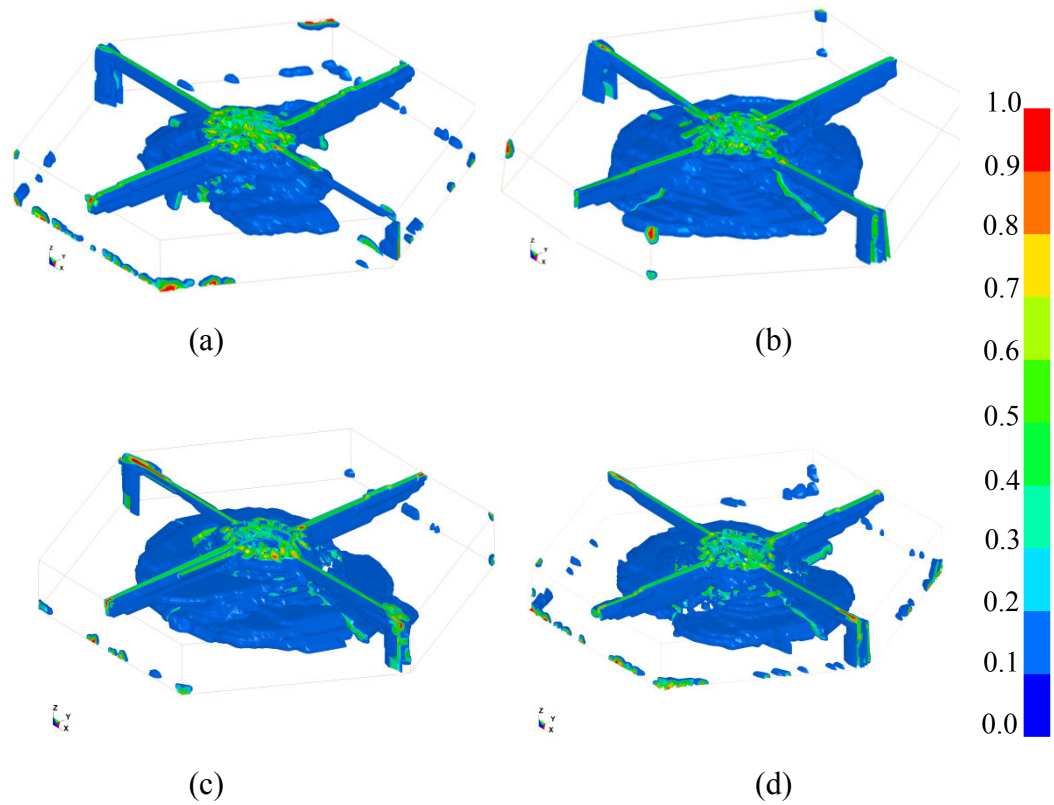


Figure 5.31. Damage contours in the ceramic layers of different interlayer configurations: ((a)-(b)) 2.3 and 4.6 mm Teflon and ((c)-(d)) 4 and 8 mm Aluminum foam.

Figure 5.32 (a) and (b) exhibit that the damage accumulation in 4.6 mm Teflon interlayer configuration was higher than that of 2.3 mm Teflon. Similarly, the amount of damage was higher for 8 mm Aluminum foam interlayer configuration than that of 4 mm Aluminum foam. It is concluded that interlayer thickness is an effective parameter in the fragmentation of ceramic. The ceramic layer was efficiently fragmented and caused more amount of projectile eroded, as thickness of interlayer was increased. The energy absorbed by ceramic increased, and the amount of energy. Compressive stress/damage transmitted to the composite layer decreased as demonstrated in Figure 5.32.

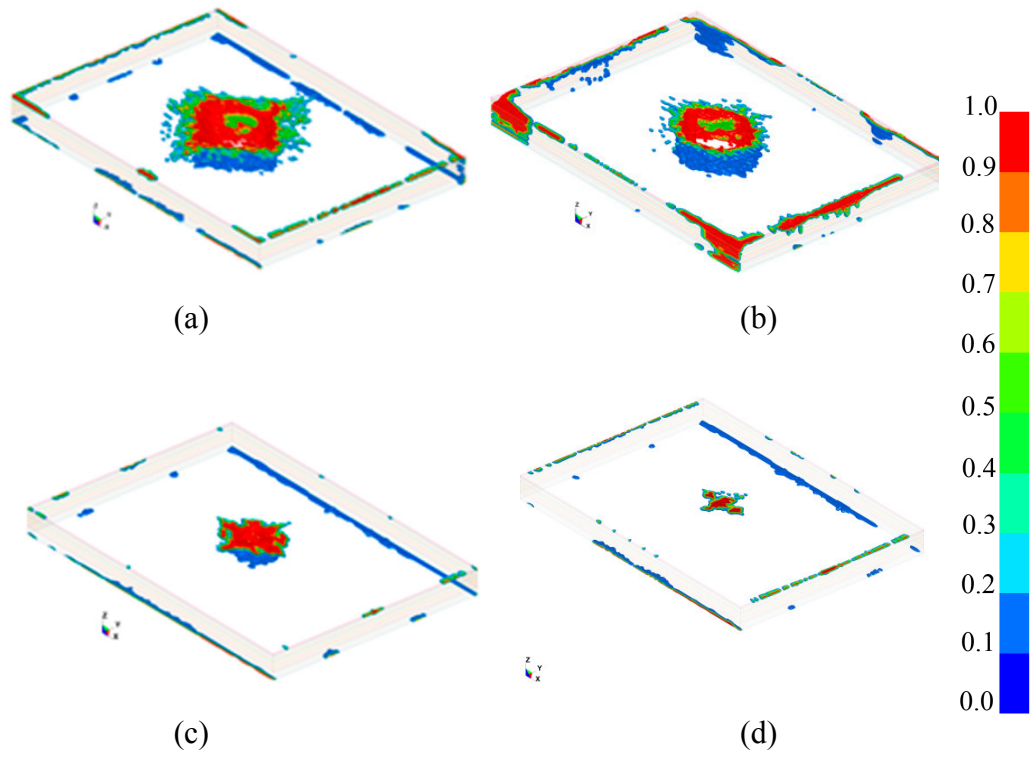


Figure 5.32. Delamination damage in composite layers of different interlayer configurations : ((a)-(b)) 2.3 and 4.6 mm Teflon and ((c)-(d)) 4 and 8 mm Aluminum foam.

CHAPTER 6

COMPRESSED AIR GUN (IMPACT CHAMBER) EXPERIMENTS

Ballistic tests were done at significantly higher impact speeds using armor piercing projectiles and results were discussed in the previous chapter. However, the effect of interlayer on impact response of composite armors at relatively low velocities has not been yet investigated in detail. Compressed air gun tests were visited to understand this behavior. 25 x 25 cm composite armor tiles were prepared by VARTM technique and hit by spherical (100Cr6) ball bearing steel at 180 ± 10 m/s. Damage accumulated in composite layer of each configuration was compared. Post-mortem analysis was carried out on alumina tiles composite plates. Additionally, projectile motion was examined by high speed camera. The results were similar to those of ballistic tests. Higher damage content was observed in composite layer of no interlayer configuration, whereas almost no damage was accumulated in Aluminum foam configuration. Interlayer reduced the damage in composite layer, particularly for Teflon and Aluminum foam. The damage of composite layer of EPDM rubber configuration was larger and deeper than Teflon.

6.1. Sample Preparation and Compressed Air Gun Tests

Multilayered armor samples consist; 5x5x1 cm 25 alumina tiles backed by 0/90 E-Glass/polyester composite plates, and Aluminum foam, Teflon and EPDM rubber interlayers bonded with polyester (CRYSTIC PAX702) as seen in Figure 6.1. Mechanical properties of constituents of armors systems used here were given in the previous chapters.

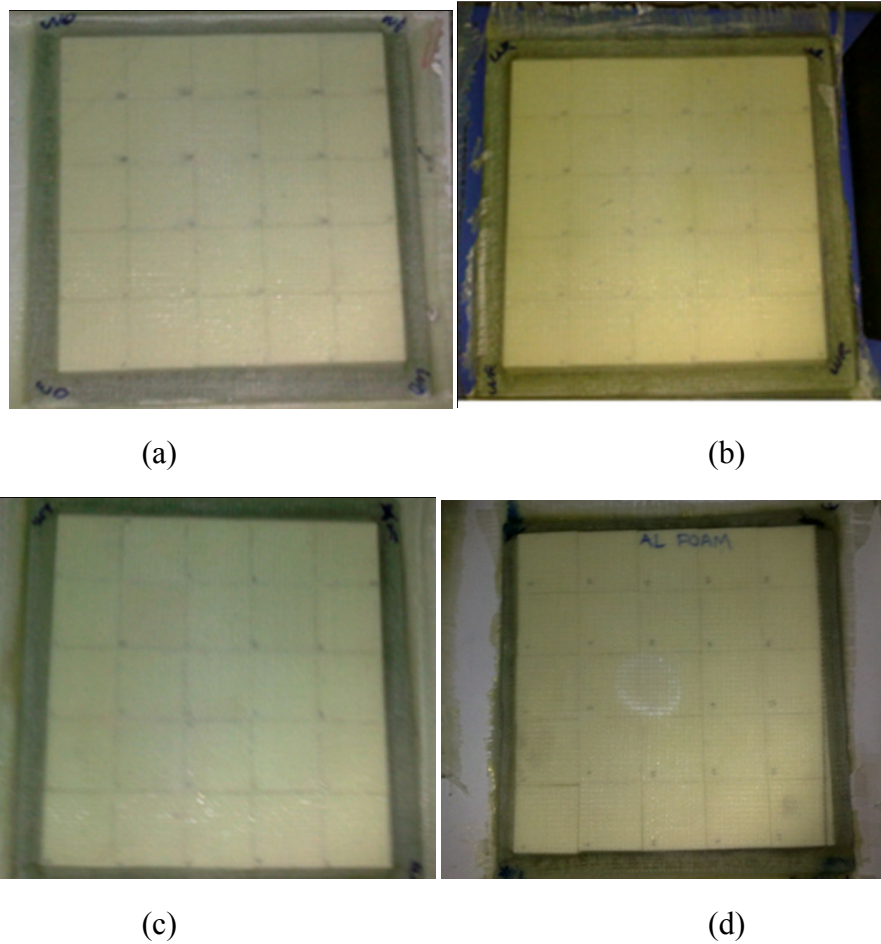


Figure 6.1. Targets of different configurations tested at compressed air gun test set-up: (a) without interlayer, (b) with EPDM rubber, (c) Teflon and (d) Aluminum foam interlayers.

Targets were impacted at 180 ± 10 m/s impact velocity by 100Cr6 spherical ball projectiles in 12.7 mm diameter. High speed camera was used to monitor projectile motion, damage evolution and ballistic response of targets. Sequential images of compressed air gun tests of various targets are given in Figure 6.2. Armors were not perforated and projectile ricocheted as expected. Target bending and projectile shattering was observed in high speed camera images.

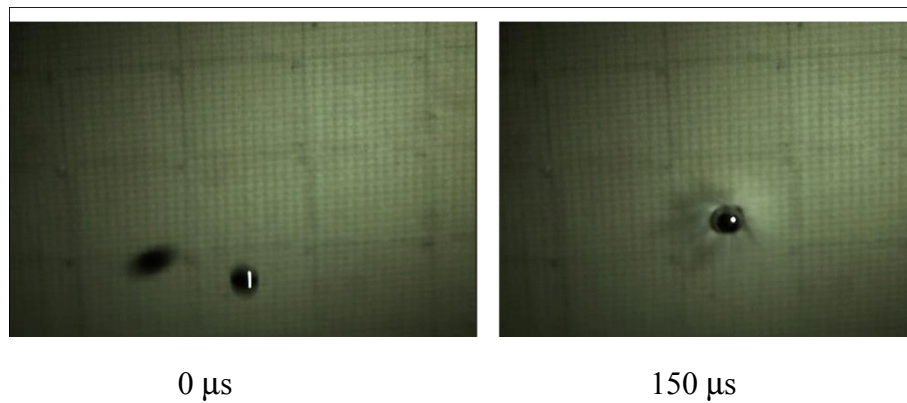
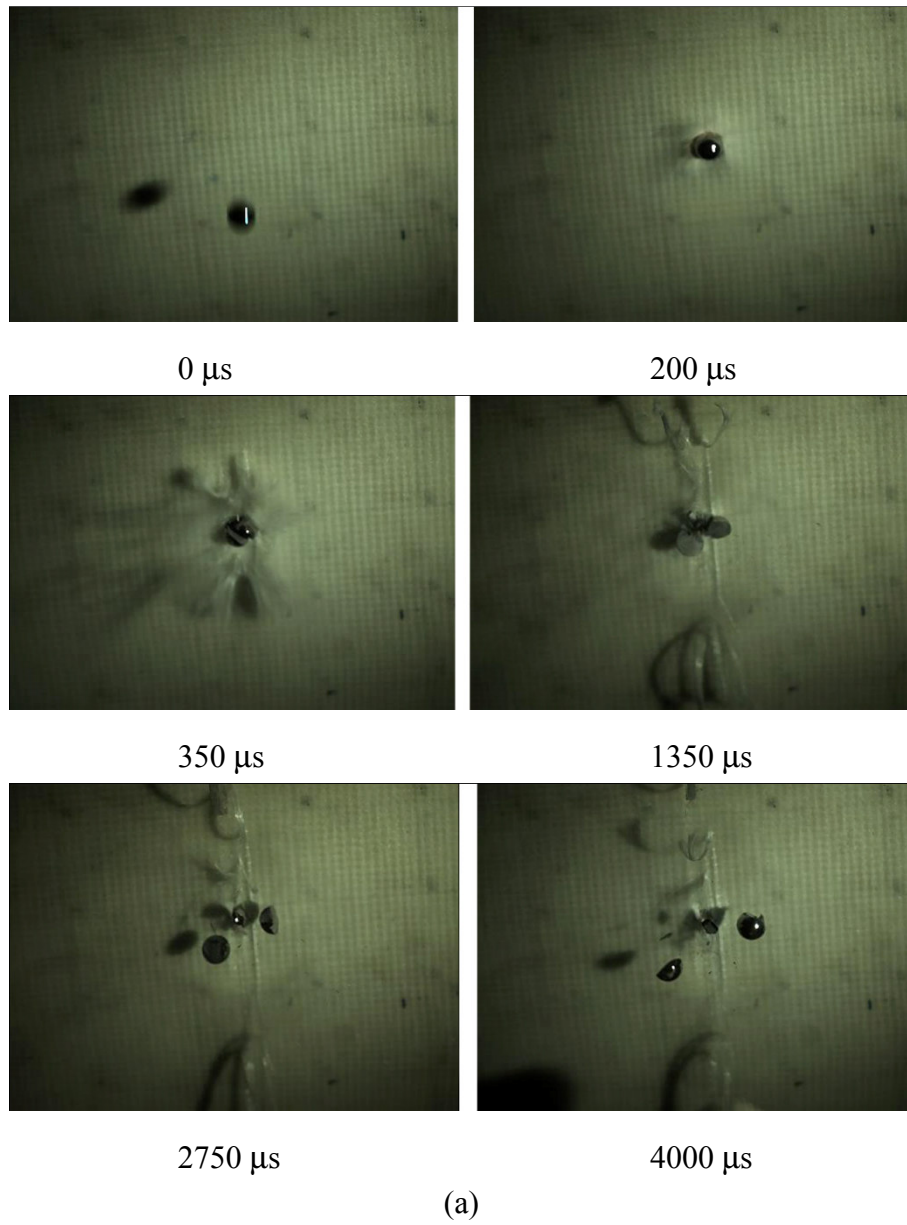
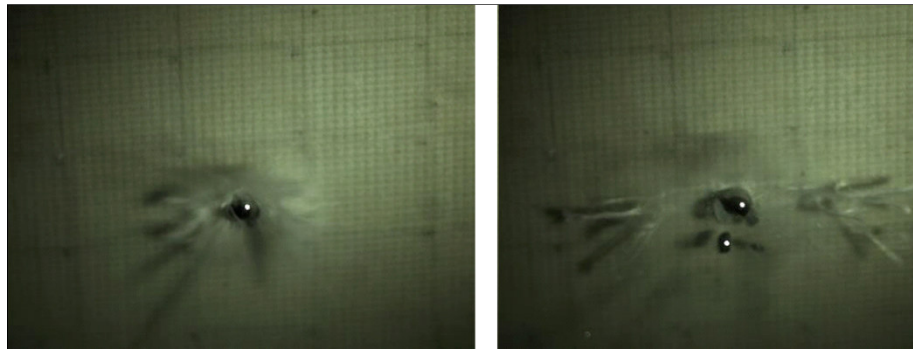


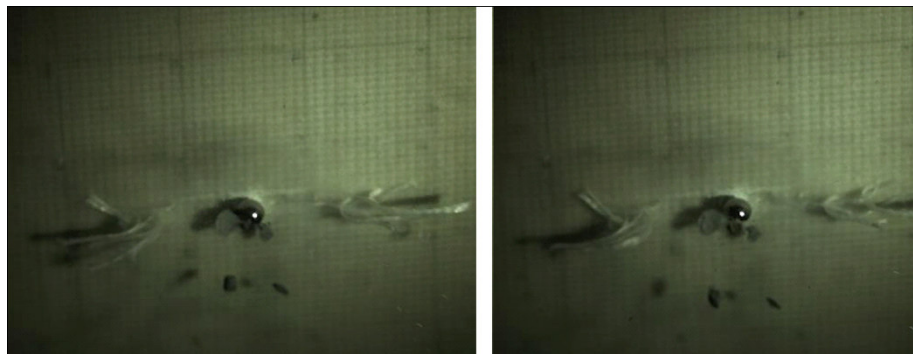
Figure 6.2. Real time images of compressed air gun tests (a)WR, (b)WT and (c) WF.

(Cont. on next page)



550 μ s

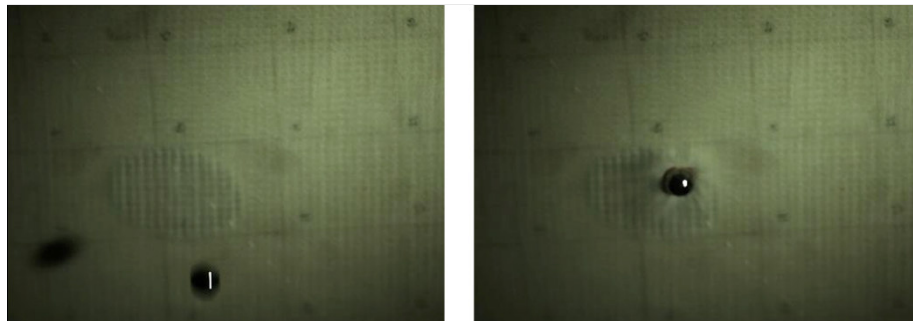
900 μ s



1500 μ s

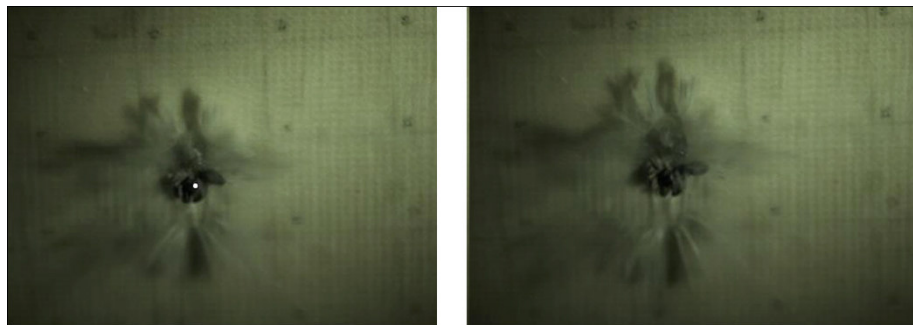
1750 μ s

(b)



0 μ s

300 μ s



500 μ s

600 μ s

Figure 6.2. (Cont.)

(Cont. on next page)

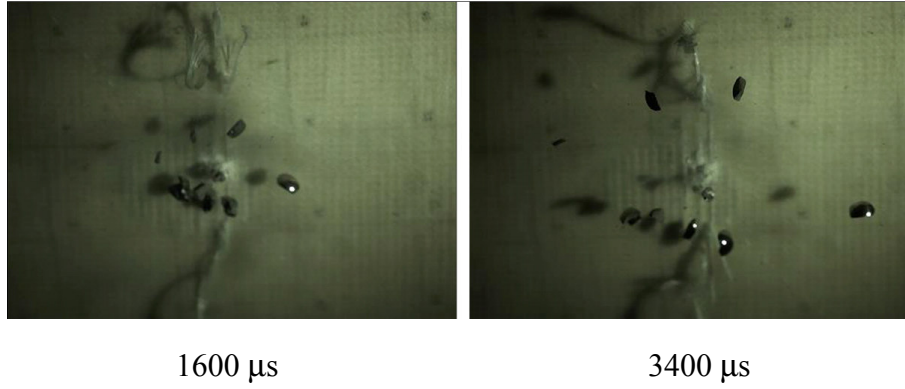


Figure 6.2. (Cont.) (c)

6.2. Damage Analysis

To demonstrate the effect of stress wave propagation and ballistic responses of targets, damage in ceramic and composite layers was investigated for each of the armor configurations. Macro cracks on alumina layer and micro cracks on composite layer were seen. Tested alumina tiles can be seen in Figure 6.3. Black ink was infused to increase the visibility of the cracks was increased. Due to the size of the each ceramic tile comprising ceramic layer extremely it was extremely hard to hit the tile in the center. However the effect of interlayer on the wave propagation was mainly traced by monitoring the damage progression in composite layer.

Table 6.1. Number of radial and circular cracks.

Configuration	# of radial cracks	# of circular cracks
WO	9	3
WR	11	1
WT	12	-
WF	14	-

As seen in Figure 6.3, the adjacent ceramic tiles to the one that was shot met no damage. Thus, radial crack propagation in the whole ceramic layer was prevented. Thus, multi hit capability of armor was increased. Moreover, adjacent layers caused confinement effect on shot tile, whole debris kept together and projectile erosion during impact was increased.

Furthermore, radial cracks was counted as well, see Figure 6.3. The number of cracks tabulated in the Table 6.1, and is in parallel with ballistic test results. Since the acoustic impedance mismatch is high in Aluminum foam and Teflon interlayer configurations, greater amount of stress wave was reflected. Thus, the number of radial cracks in Teflon and Aluminum foam interlayer containing configurations is higher. While the number of circular cracks resulting from compressive stresses are higher in ceramic layer of without and EPDM rubber interlayer configurations.

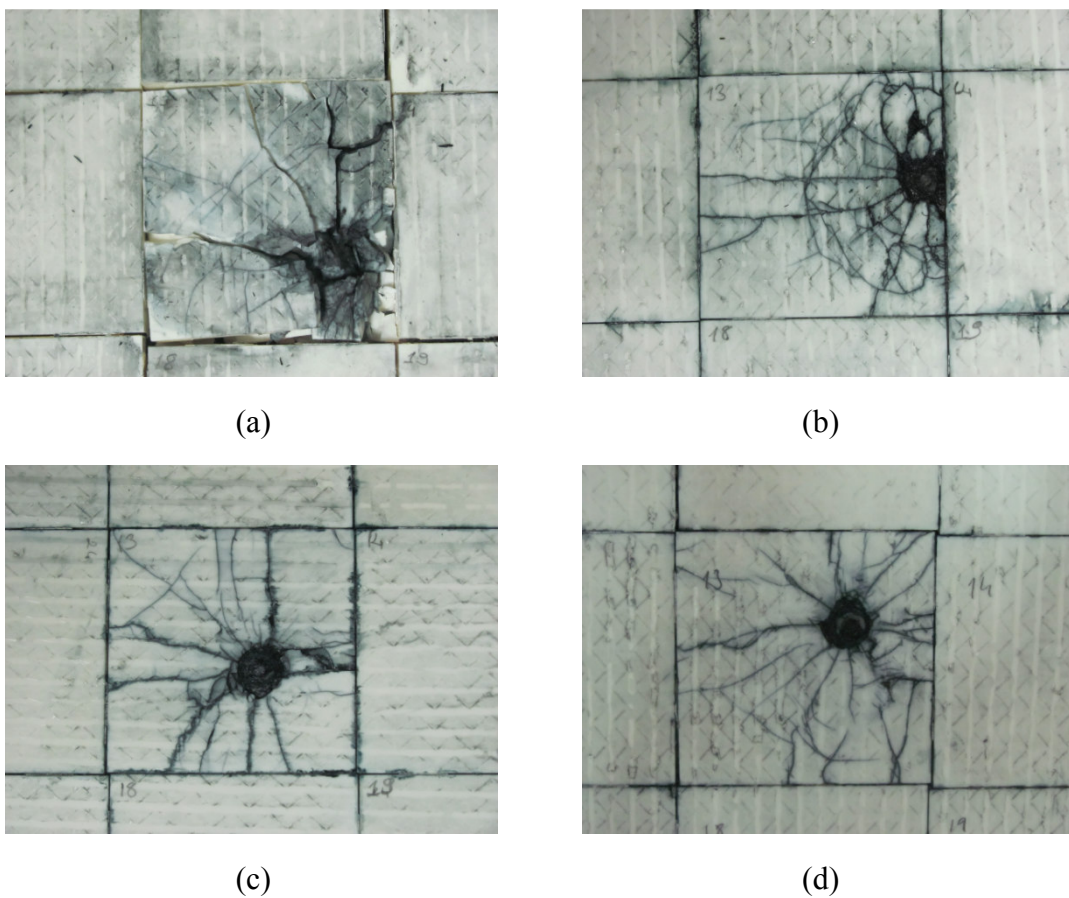


Figure 6.3. Damage contours in the ceramic layer after compressed air gun tests: (a) WO (b) WR, (c) WT and (d) WF configurations.

As seen in the figures below, backing plates delaminated with different extents. Delamination in composite layers of the configurations compared and results were in a good agreement with those of ballistic tests observed in composite layer of Aluminum metallic foam configuration, whereas, the deepest and largest amount of delamination was observed in without interlayer case.

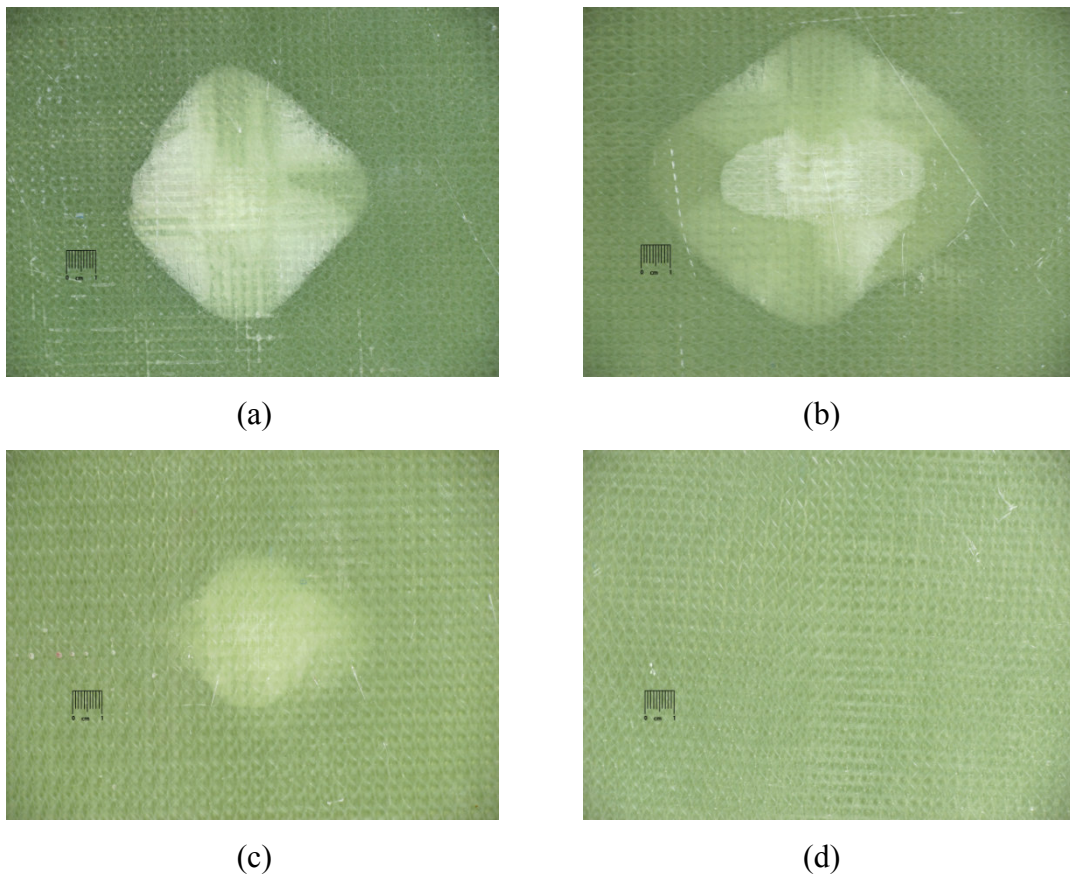


Figure 6.4. Delamination damage contours in the composite layer after compressed air gun tests: (a) WO (b) WR (c) WT and (d) WF configurations.

It is also noted that the discoloring inside the delaminated zone of composite layers were different. Light colored areas illustrate the delamination close to the bottom layers of composite. For the composite layer of without interlayer configuration, greater amount of delamination was observed and the damaged zone was deeper. However, EPDM rubber containing configurations experienced less amount of delamination than without interlayer configuration, it was not as shallow and localized as Teflon case.

To observe the different damage modes in composite plates better, composite plates were sectioned from the areas close to the hit zone and SEM images were taken. The images were taken at 100X magnification, see Figure 6.5.

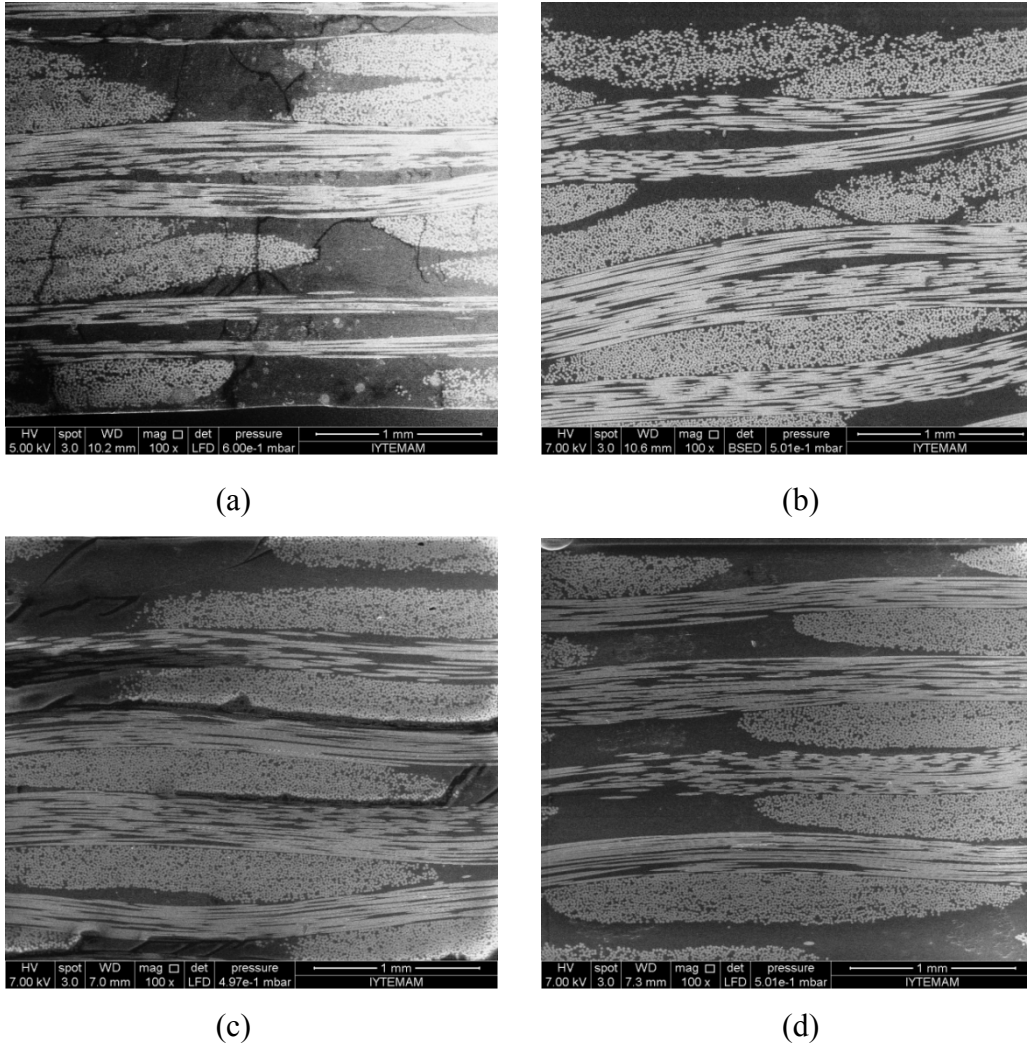


Figure 6.5. SEM images of composite layers: (a) WO (b) WR (c) WT and (d) WF configurations.

As seen can be seen from the Figures 6.5 and 6.6, almost no visible delamination was accumulated in Aluminum foam configuration while both delamination and fiber damage such as fiber crushing was observed for EPDM rubber, Teflon and no interlayer configurations. Delamination generally occurs due to the reflected tensile stress waves

and bending related tensile stresses in composite layer. In gas gun experiments, delamination occurred mainly under the action of bending related stress. On the other hand, the main reason for fiber damage is compressive stress waves crushing abruptly along the through-thickness direction. These waves compress fibers and cause them to crush each other. SEM images given in Figures 6.6 and 6.7 demonstrate fiber crushing and matrix cracks in details.

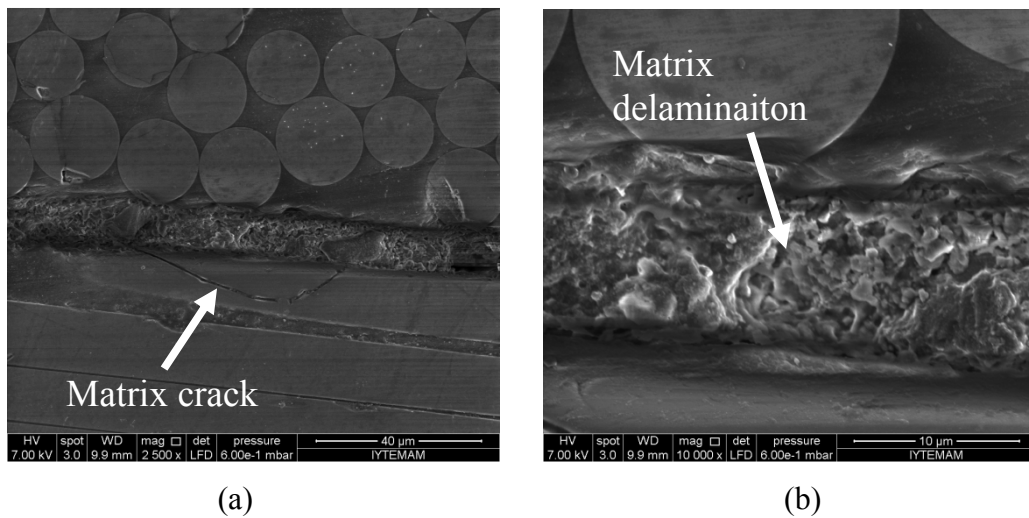
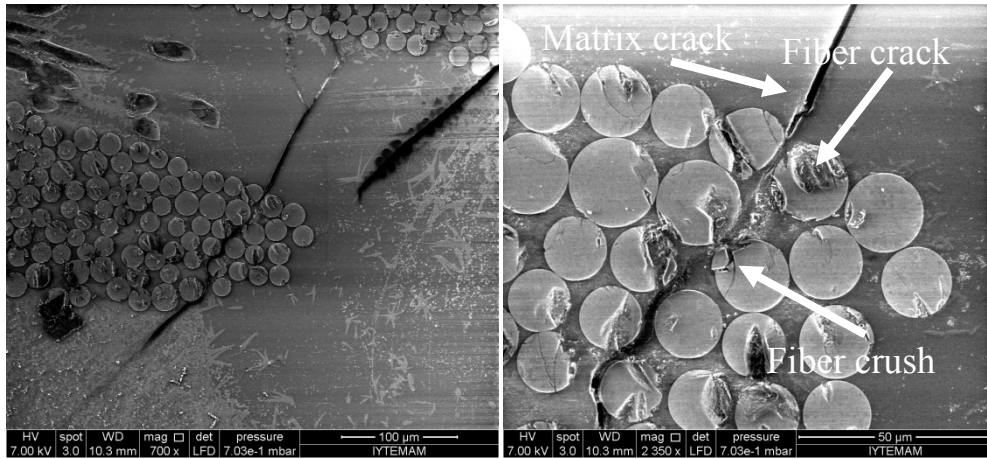


Figure 6.6. Different damage modes observed in Teflon configuration.

As a result, damage and crack analysis indicate that Aluminum foam and Teflon are the most efficient interlayers. Compressed air gun tests give parallel results to those of ballistic tests.



(a)

(b)

Figure 6.7. Fiber crush and fiber/matrix cracks observed in rubber configuration.

CHAPTER 7

CONCLUSION

In this study the effect of the interlayers on the ballistic performance of ceramic/composite armors were investigated both experimentally and numerically. The use of numerical model allowed detailed analysis of the stress wave propagation and energy partitioning between the layers. To monitor the damage initiation and propagation, ceramic and composite layers were modeled with appropriate material models and the damage parameters were incorporated. The conclusions obtained from the results are given below:

Similar to previous studies, it has been proved that, material model constants determined from SHPB and quasi-static tests can be applied successfully into armor simulations. Good agreement between the numerical models and experiments were observed.

The presence of interlayer significantly altered the stress wave transmission between the layers.

Among the tested configurations Teflon and metallic foam were presented better results. EPDM rubber interlayer did not cause any significant delay in the initial stress build-up in the composite layer, whereas Teflon and Aluminum foam interlayer caused a significant delay and reduction in the magnitude of the stress transmitted to the composite backing plate.

It was confirmed that, the ceramic layer was efficiently fragmented during the ballistic impact of Aluminum foam and Teflon interlayer configuration. Hence, greater amount of projectile kinetic energy was absorbed at ceramic-projectile interface and the remaining energy transmitted to composite backing plate was decreased.

Aluminum metallic foam presents best performance in aspects of armor design such as delay in stress-rise time, reduction in magnitude of the stress and energy transmitted to composite backing plate.

The comparison of Teflon and Aluminum foam interlayers at two different areal density values demonstrates that the increase in thickness raises the ballistic performance but this is valid up to a certain limit weight performance ratio decreases.

Behaviors of armors are similar at both low and high impact velocities.

Similar to S2-Glass epoxy, 0/90 E-Glass/polyester is a strain rate sensitive material and its strain rate sensitivity is higher in in-plane direction than through-thickness. Thus, MAT162 material model which considers strain rate dependency and represents deformation after failure is convenient mode for composite plates.

Possible studies suggested for the future are given below:

Since MAT162 material model allows user to define the orientation of each layer of composite plate directly, E-Glass/polyester or S-2 Glass epoxy composite backing plates with different orientation lay-ups can be successfully modeled. Effect of orientation lay-up on composite backing plate can be compared.

Obliquity of impact can be investigated.

Since the efficiency of Aluminum foam is demonstrated, a thickness and density optimization study can be further conducted.

Since the model is validated, the type of projectile can be changed to investigate ballistic performance of armors against various projectiles.

Compressed air gun tests simulations can be carried out to observe the stress wave propagation at low impact velocities as seen in Figure 7.1.

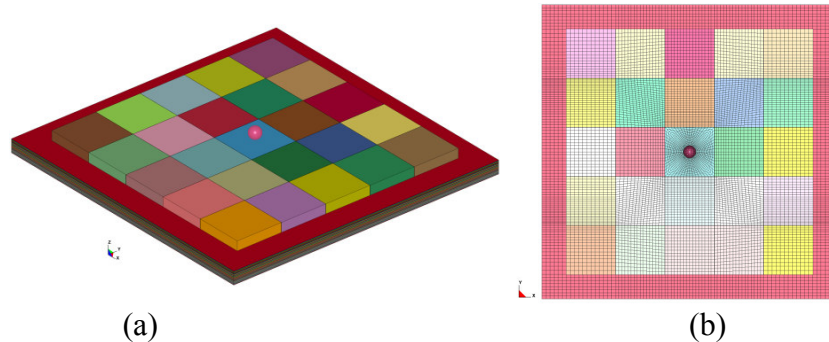


Figure 7.1. Preliminary study of a compressed air gun numerical model.

REFERENCES

- Abrate, S., 2001, Modeling of impact on composite structures. *Composite Structures*. 51 p. 129-138.
- Abrate, S., 2003, Wave propagation in lightweight composite armor. *Journal De Physique Iv*. 110 p. 657-662.
- Abrate, S., 2009. Ballistic Impacts on Composite and Sandwich Structures. *I. M. D. e. al. Carbondale, Springer Science+Business Media*.
- Anderson, C. E. and Morris, B. L., 1992, The ballistic performance of confined Al₂O₃ ceramic tiles. *International Journal of Impact Engineering*. 12(2): p. 167-187.
- Anderson, C. E., Mullin, S. A., Piekutowski, A. J., Blaylock, N. W. and Poormon, K. L., 1996, Scale model experiments with ceramic laminate targets. *International Journal of Impact Engineering*. 18(1): p. 1-22.
- Borvik, T., Langseth, M., Hopperstad, O. S. and Malo, K. A., 1999, Ballistic penetration of steel plates. *International Journal of Impact Engineering*. 22(9-10): p. 855-885.
- Bruck, H. A., 2000, A one-dimensional model for designing functionally graded materials to manage stress waves. *International Journal of Solids and Structures*. 37(44): p. 6383-6395.
- Collombet, F., Lalbin, X. and Lataillade, J. L., 1998, Impact behavior of laminated composites: Physical basis for finite element analysis. *Composites Science and Technology*. 58(3-4): p. 463-478.
- Coorstek, AD995 Alumina 99.5% Al₂O₃, <http://www.coorstek.com/materials/ceramics/alumina/ad995.asp>, 2011.
- Davies, G. A. O. and Zhang, X., 1995, Impact damage prediction in carbon composite structures. *International Journal of Impact Engineering*. 16(1): p. 149-170.
- Deka, L., Bartus, S. and Vaidya, U., 2008, Damage evolution and energy absorption of E-glass/polypropylene laminates subjected to ballistic impact. *Journal of Materials Science*. 43(13): p. 4399-4410.

- DeLuca, E., Prifti, J., Betheney, W. and Chou, S. C., 1998, Ballistic impact damage of S 2-glass-reinforced plastic structural armor. *Composites Science and Technology*. 58(9): p. 1453-1461.
- Ergonenc, C., 2008, Development and design of closed-cell aluminum foam-based lightweight sandwich structures for blast protection, *M.Sc., Izmir Institute of Technology, Izmir*.
- Fawaz, Z., Zheng, W. and Behdinan, K., 2004, Numerical simulation of normal and oblique ballistic impact on ceramic composite armours. *Composite Structures*. 63(3-4): p. 387-395.
- Gama, B. A., Bogetti T.A., Fink B.K., Mahfuz H., Gillespie Jr. J.W., 1998, Study of through-thickness wave propagation in multi-layer hybrid lightweight armor, *13th Annual Technical Conference of the American Society for Composites*, Baltimore, MD.
- Gama, B. A., Bogetti, T. A., Fink, B. K., Yu, C. J., Claar, T. D., Eifert, H. H. and Gillespie, J. W., 2001, Aluminum foam integral armor: a new dimension in armor design. *Composite Structures*. 52(3-4): p. 381-395.
- Gama, B. A., Gillespie Jr JW, Bogetti TA, Fink B., 2001. Innovative design and ballistic performance of lightweight composite integral armor. *SAE 2001 World Congress*. Detroit, USA.
- Gama, B. A., Gillespie, J. W. Jr., Mahfuz, H., Bogetti, T.A. and Fink, B., 2000, Effect of non-Linear material behavior on the through-thickness stress wave propagation in multi-layer hybrid lightweight armor, *Advances in Composite Engineering. and Science*. Technical Science Press.
- gizmag, liquid armor, <http://www.gizmag.com/liquid-armor/15771>, 2011
- global security, Military, <http://www.globalsecurity.org/military/systems/ground/body-armor2.htm>, 2011
- Gooch, W., Burkins, B., Palicka, M., Rubin, R. and Ravichandran, J., 1999. Development and ballistic testing of a functionally gradient ceramic/metal applique. *Material Science Forum*: 308-311:614-321.
- Gordon, R. J. and Tim, J. H., 1994, An Improved Model for Brittle Materials. *American Institute of Physics*. p. 981-984.
- Guden, M. and Yuksel, S., 2006, SiC-particulate aluminum composite foams produced from powder compacts: foaming and compression behavior. *Journal of Materials Science*. 41(13): p. 4075-4084.

- Gupta, N. K. and Madhu, V., 1992, Normal and oblique impact of a kinetic-energy projectile on mild-steel plates. *International Journal of Impact Engineering*. 12(3): p. 333-343.
- Gupta, Y. M. and Ding, J. L., 2002, Impact load spreading in layered materials and structures: concept and quantitative measure. *International Journal of Impact Engineering*. 27(3): p. 277-291.
- Hashin, Z., 1980, *Failure criteria for unidirectional fiber composites*. *Journal of Applied Mechanics*. 47(2): p. 329-334.
- history of armor, history of armor , <http://www.history-of-armor.com>, 2011.
- howstuffworks, liquid body armor, <http://science.howstuffworks.com/liquid-body-armor1.htm>, 2011
- inetres, 7.62 mm (7.62x51 mm) ammunition, http://www.inetres.com/gp/military/infantry/rifle/762mm_ammunition.html, 2011.
- Krashanitsa, R. and Shkarayev, S., 2005, Computational Study of Dynamic Response and Flow Behavior of Damaged Ceramics. *46th AIAA/ASME/ASCE/AHS/ASC Structural Dynamics & Material Conference*, Austin, Texas.
- Kumar, K. S. and Bhat, T. B., 1998, Response of composite laminates on impact of high velocity projectiles. *Impact Response and Dynamic Failure of Composites and Laminate Materials*, Pts 1 and 2. 141-1: p. 337-348.
- Littlefield, D. L., Anderson, C. E., Partom, Y. and Bless, S. J., 1997, The penetration of steel targets finite in radial extent. *International Journal of Impact Engineering*. 19(1): p. 49-62.
- Liu, L. S., Zhang, Q. J., Zhai, P. C. and Zhu, C. C., 2003, Impact characteristic analysis of ceramic/metal FGM. *Functionally Graded Materials Vii*. 423-4: p. 641-644.
- Lopez-Puente, J., Arias, A., Zaera, R. and Navarro, C., 2005, The effect of the thickness of the adhesive layer on the ballistic limit of ceramic/metal armours. An experimental and numerical study. *International Journal of Impact Engineering*. 32(1-4): p. 321-336.
- Livermore Software Technology Corporation, (LSTC), 2007, LS-DYNA Keyword User's Manual, *Livermore, USA*
- Matzenmiller, A., Lubliner J., a. and Taylor, R. L., 1995, A constitutive model for anisotropic damage in fiber-composites. *Mechanics of Materials*. 20(2): p. 125-152.

- Mines, R. A. W., 2004, A one-dimensional stress wave analysis of a lightweight composite armour. *Composite Structures*. 64(1): p. 55-62.
- Naik, N. K., Asmelash, A., Kavala, V. R. and Ch, V., 2007, Interlaminar shear properties of polymer matrix composites: Strain rate effect. *Mechanics of Materials*. 39(12): p. 1043-1052.
- Naik, N. K. and Kavala, V. R., 2008, High strain rate behavior of woven fabric composites under compressive loading. *Materials Science and Engineering a-Structural Materials Properties Microstructure and Processing*. 474(1-2): p. 301-311.
- National Institute of Justice , 2008. NIJ Standard. *Ballistic resistance of body armor* 46.
- Ogden, R. W., 1984, Non-linear elastic deformations, *Halsted Press*.
- Pahr, D. H., Rammerstorfer, F. G., Rosenkranz, P., Humer, K. and Weber, H. W., 2002, A study of short-beam-shear and double-lap-shear specimens of glass fabric/epoxy composites. *Composites Part B: Engineering*. 33(2): p. 125-132.
- Robbins, J. R., Ding, J. L. and Gupta, Y. M., 2004, Load spreading and penetration resistance of layered structures - a numerical study. *International Journal of Impact Engineering*. 30(6): p. 593-615.
- Roeder, B. A. and Sun, C. T., 2001, Dynamic penetration of alumina/aluminum laminates: experiments and modeling. *International Journal of Impact Engineering*. 25(2): p. 169-185.
- Sadanandan, S. and Hetherington, J. G., 1997, Characterisation of ceramic/steel and ceramic/aluminium armours subjected to oblique impact. *International Journal of Impact Engineering*. 19(9-10): p. 811-819.
- Sherman, D., 2000, Impact failure mechanisms in alumina tiles on finite thickness support and the effect of confinement. *International Journal of Impact Engineering*. 24(3): p. 313-328.
- Sherman, D. and Ben-Shushan, T., 1997, Quasi-static impact damage in confined ceramic tiles. *International Journal of Impact Engineering*. 21(4): p. 245-265.
- Shokrieh, M. M. and Javadpour, G. H., 2008, Penetration analysis of a projectile in ceramic composite armor. *Composite Structures*. 82(2): p. 269-276.
- Smith, P. D. and Hetherington, J. G., 2003, Blast and Ballistic Loading of Structures. Butterworth Heinemann.

- Sorensen, B. R., Kimsey, K. D., Silsby, G. F., Scheffler, D. R., Sherrick, T. M. and Derosset, W. S., 1991, High-velocity penetration of steel targets. *International Journal of Impact Engineering*. 11(1): p. 107-119.
- Tasdemirci, A., 2005, Experimental and modeling of stress wave propagation in multilayer composite materials, *PhD, University of Delaware, Newark, USA*.
- Tasdemirci, A. and Hall, I. W., 2005, Experimental and modeling studies of stress wave propagation in multilayer composite materials: Low modulus interlayer effects. *Journal of Composite Materials*. 39(11): p. 981-1005.
- Tasdemirci, A. and Hall, I. W., 2006, Numerical and experimental studies of damage generation in a polymer composite material at high strain rates. *Polymer Testing*. 25(6): p. 797-806.
- Tasdemirci, A. and Hall, I. W., 2007a, The effects of plastic deformation on stress wave propagation in multi-layer materials. *International Journal of Impact Engineering*. 34(11): p. 1797-1813.
- Tasdemirci, A. and Hall, I. W., 2007b, Numerical and experimental studies of damage generation in multi-layer composite materials at high strain rates. *International Journal of Impact Engineering*. 34(2): p. 189-204.
- Tasdemirci, A. and Hall, I. W., 2009, Development of novel multilayer materials for impact applications: A combined numerical and experimental approach. *Materials & Design*. 30(5): p. 1533-1541.
- Tunusoglu, G., Tasdemirci, A., Guden, M. and Hall, I. W., 2010, Numerical and experimental studies of high strain rate mechanical behavior of E-glass /polyester composite laminates, *10th Biennial Conference on Engineering Systems Design and Analysis ASME 2010 Istanbul, TURKEY*.
- wikipedi, Tankın tarihi, http://tr.wikipedia.org/wiki/History_of_the_tank, 2011, June.
- wikipedia, armour, <http://en.wikipedia.org/wiki/Armour>, 2011, June.
- Xiao, J. R., Gama, B. A. and Gillespie, J. W., 2007, Progressive damage and delamination in plain weave S-2 glass/SC-15 composite under quasi-static punch-shear loading. *Composite Structures*. 78(2): p. 182-196.
- Yadav, S. and Ravichandran, G., 2003, Penetration resistance of laminated ceramic/polymer structures. *International Journal of Impact Engineering*. 28(5): p. 557-574.

- Yuksel, S., 2010, The effects of SiC particle addition on the foaming behavior of aluminum closed-cell foams produced by powder compacts, *PhD, Izmir Institute of Technology*, Izmir, TURKEY.
- Zaera, R., Sanchez-Saez, S., Perez-Castellanos, J. L. and Navarro, C., 2000, Modelling of the adhesive layer in mixed ceramic/metal armours subjected to impact. *Composites Part a-Applied Science and Manufacturing*. 31(8): p. 823-833.
- Zaera, R. and SanchezGalvez, V., 1997, Modelling of fracture processes in the ballistic impact on ceramic armours. *Journal De Physique Iv*. 7(C3): p. 687-692.
- Zhang, Z. G., Wang, M. C., Song, S. C., Li, M. and Sun, Z. J., 2010, Influence of panel/back thickness on impact damage behavior of alumina/aluminum armors. *Journal of the European Ceramic Society*. 30(4): p. 875-887.
- Zukas, J. A., Nicholas, T., Swift, H. F., Greszczuck, L. B. and Curran, D. R., 1992, Impact Dynamics, *Krieger Publishing Company*
- Zuoguang, Z., Mingchao, W., Shuncheng, S., Min, L. and Zhijie, S., 2010, Influence of panel/back thickness on impact damage behavior of alumina/aluminum armors. *Journal of the European Ceramic Society*. 30(4): p. 875-887.